Experimental Study of Perovskite Nanocrystals as Single Photon Sources for Integrated Quantum Photonics

Stefano Pierini

Thèse
de doctorat
de l'UTT

Stefano PIERINI

Experimental Study of Perovskite Nanocrystals as Single Photon Sources for Integrated Quantum Photonics

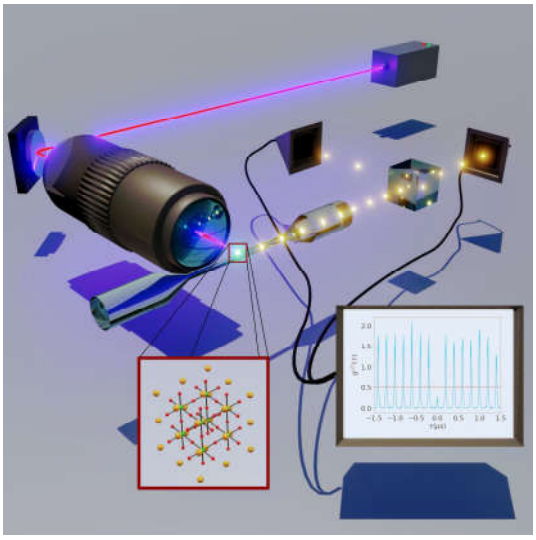

Champ disciplinaire :
Sciences pour l'Ingénieur

2021TROY0009 **Année 2021**

utt
UNIVERSITÉ DE TECHNOLOGIE
TROYES

THESE

pour l'obtention du grade de

DOCTEUR
de l'UNIVERSITE DE TECHNOLOGIE DE TROYES

en SCIENCES POUR L'INGENIEUR

Spécialité : MATERIAUX, MECANIQUE, OPTIQUE, NANOTECHNOLOGIE

présentée et soutenue par

Stefano PIERINI

le 11 février 2021

Experimental Study of Perovskite Nanocrystals as Single Photon Sources for Integrated Quantum Photonics

JURY

Mme Sara DUCCI	PROFESSEURE DES UNIVERSITES	Présidente
Mme Carole DIEDERICHS	MAITRE DE CONFERENCES - HDR	Rapporteure
M. Marco GENOVESE	PROFESSORE	Rapporteur
M. Alberto BRAMATI	PROFESSEUR DES UNIVERSITES	Directeur de thèse
M. Christophe COUTEAU	PROFESSEUR ASSOCIE UTT	Directeur de thèse

Personnalité invitée

M. Emmanuel LHUILLIER	DIRECTEUR DE RECHERCHE CNRS

Experimental study of perovskite nanocrystals as single photon sources for integrated quantum photonics

Étude expérimentale des nanocristaux de pérovskite comme sources de photons uniques pour la photonique quantique intégrée

Stefano Pierini

Contents

1 Introduction **1**

1.1 Preface . . . 2

1.1.1 Motivation for this study . . . 2

1.1.2 Structure of the manuscript . . . 3

1.2 Quantum mechanics . . . 3

1.3 Quantum Optics . . . 8

1.4 Single photon emitters . . . 9

1.4.1 Theory and definition . . . 9

1.4.2 Semiclassical approach . . . 10

1.4.3 Quantum theory of coherence . . . 12

1.4.4 Single photon emission . . . 12

1.4.5 Experimental limitations . . . 13

1.4.6 Examples of single photon emitters . . . 13

1.5 Common characteristics of solid state single photon emitters . . . 16

1.5.1 Non radiative recombination . . . 17

1.5.2 Saturation . . . 20

1.5.3 Emission Lifetime . . . 20

1.5.4 Blinking . . . 22

1.5.5 Polarization . . . 26

1.6 Guided and integrated optics . . . 30

2 Perovskite nanocrystals **35**

2.1 Introduction . . . 36

2.1.1 Interest for perovskites . . . 36

2.1.2 Perovskite nanocrystals . . . 37

2.2 Experimental setup for nanocrystal characterisation . . . 42

2.2.1 Perovskite fabrication . . . 44

2.2.2 Sample preparation . . . 46
2.2.3 Experimental Setup . . . 46
2.3 Measurements . . . 50
2.3.1 Perovskite Spectra . . . 50
2.3.2 Saturation behaviour . . . 51
2.3.3 Polarization measurements . . . 53
2.3.4 $g^{(2)}$ measurements . . . 57
2.4 Stability . . . 62
2.4.1 Role of the polystyrene . . . 62
2.4.2 Role of the Sample preparation . . . 63
2.5 Blinking properties . . . 65
2.6 $g^{(2)}$ distribution . . . 68

3 Coupling nanoemitters to nanofibers 73
3.1 Optical fiber . . . 73
3.2 Light propagation inside optical fibers . . . 75
3.2.1 Propagation in a planar guide . . . 75
3.2.2 Propagation in optical fibers . . . 78
3.2.3 Modes of a tapered optical nanofiber . . . 84
3.3 Nanofiber fabrication . . . 90
3.3.1 Choosing the profile of the fiber . . . 90
3.3.2 Pulling mechanism . . . 91
3.3.3 Experimental details . . . 94
3.4 Experimental Setup . . . 97
3.5 Nanocrystal deposition and antibunching measurement on the nanofiber 100

4 Outlook and future perspectives 105
4.1 Introduction . . . 105
4.2 Perovskite optimization . . . 106
4.3 Single defects in nanodiamonds . . . 106
4.3.1 Nitrogen-Vacancy color centers . . . 107
4.3.2 Silicon-Vacancy color centers . . . 108
4.4 Ion-exchange glass waveguides . . . 111
4.4.1 Deterministic positioning of emitters on top of a waveguide . . . 112

Conclusions 119

A Analysis software for TTTR3 files **121**
A.1 Introduction . . . 121
A.2 The software usage . . . 122
A.2.1 *Settings* panel . . . 123
A.2.2 Visualization panels . . . 124
A.2.3 Possible future improvements . . . 129
A.3 Tools used . . . 130
A.3.1 C++ programming language . . . 130
A.3.2 Qt . . . 131
A.4 Algorithm and code details . . . 132
A.4.1 Principal files of the code . . . 132
A.4.2 Algorithm main points . . . 134

R Résumé en français **137**
R.1 Introduction . . . 137
R.1.1 Émetteurs à photon unique . . . 138
R.1.2 Optique guidée et integrée . . . 143
R.2 Pérovskite . . . 145
R.2.1 Nanocristaux de Pérovskite . . . 145
R.2.2 Caractérisation expérimentale . . . 146
R.2.3 Mesures . . . 148
R.2.4 Saturation . . . 148
R.2.5 Mesures de polarisation . . . 150
R.2.6 Stabilité . . . 151
R.2.7 Distribution du $g^{(2)}(0)$ en fonction de la longueur d'onde . . . 153
R.3 Nanofibres . . . 153
R.4 Perspectives . . . 156
R.4.1 Emetteurs . . . 157
R.4.2 Guides d'onde à échange ionique . . . 157

Acknowledgments

Research is a collective process of discovery and transmitting knowledge. With no-doubts, my PhD project was not possible without the help of all the people I worked with. I would like to thank them all, no matter their role, for their contribution in this project. All of them were important. I would like to mention some of those whose contributions have been most relevant.

First of all, my PhD directors Christophe Couteau and Alberto Bramati, who found the funding to make this project possible, believed in my abilities and guided me in this path. Alberto, moreover, has followed me scientifically and humanly, in every step I have taken since I decided to continue my studies outside Italy, and I want to thank him for that. I would also like to acknowledge the other permanents of the group, Quentin and Elisabeth: they didn't hesitate to give me help and suggestions any time I needed.

In understanding the experiment, the help of the previous Ph.D. student of the group, Maxime, was essential. He spent all the needed time in training me, from the most technical skills like fiber pulling to the most simple ones, like were to find stuff in the lab.

I also want to thank my colleagues, Giuseppe, Chendjie and Marianna, working with them was a privilege and a pleasure. We shared hours in the lab and we discussed on how to solve problems.

A good working environment is the key to stay productive and motivated: from this point of view I was lucky. For this reason I would like to thank Jean-Philippe, Aurthur, Aurelie, Giovanni, Anne, Quentin, Murad, Ferdinand, Tom, Rajiv, Giacomo.

My studies were allowed by a permitted by different collaboration, among them the most fruitful was the one with Emmanuel Lhuillier, at the INSP. I thank him for all the time he spent in the developing perovskites nanocrystlas object of my research and replying to all my questions on them.

Finally I want to thank Ermelinda, with whom I not only spent all my free time, but also shared every detail of this work from the beginning and who helped me to overcome

all the difficulties encountered, scientific and human.

Chapter 1

Introduction

Contents

1.1 Preface **2**
1.1.1 Motivation for this study 2
1.1.2 Structure of the manuscript 3
1.2 Quantum mechanics **3**
1.3 Quantum Optics **8**
1.4 Single photon emitters **9**
1.4.1 Theory and definition 9
1.4.2 Semiclassical approach 10
1.4.3 Quantum theory of coherence 12
1.4.4 Single photon emission 12
1.4.5 Experimental limitations 13
1.4.6 Examples of single photon emitters 13
Single neutral atoms 14
Single ions 15
Quantum dots 15
Color centers in diamonds and nanodiamonds 15
1.5 Common characteristics of solid state single photon emitters . **16**
1.5.1 Non radiative recombination 17
Auger recombination 17
Interaction of excitons with phonons 18
Charge trapping 19
1.5.2 Saturation 20
1.5.3 Emission Lifetime 20
1.5.4 Blinking 22

Binning analysis 23
Intensity auto-correlation function 24
Fluorescence lifetime intensity distribution 26
1.5.5 Polarization 26
1.6 Guided and integrated optics 30

1.1 Preface

1.1.1 Motivation for this study

Perovskites were originally studied for solar-cell applications [1], but the interest in these material is recently increased in the quantum optics community. The versatility of perovskite nanocrystal, the fact that they have been shown to emit single photon at low [2, 3] and room [4] temperature, the possibility to tune their emission playing on their composition, makes them interesting emitters for quantum optics applications.

As other kind of colloidal quantum dots, these emitters can be fabricated without heavy facilities, using low-cost wet-chemistry techniques, and this in contrast to other emitters, such single defects in nanodiamonds and epitaxial quantum dots, that require heavy fabrication facilities.

Despite several kind of colloidal quantum dots present similar features and are nowadays well known, the appropriate choice of composition makes perovskite nanocrystals able to emit in the near infrared range, fact that is difficult to obtain with other kind of colloidal nanocrystals.

Perovskites nanocrystals currently produced have a main limitation: the optical stability. Previous attempts to improve the photostabilty of these emitters involved polymer encapsulation [5, 6], alumina encapsulation using atomic layer deposition and surface passivation [7]. In this work, in the second chapter, I describe a fabrication method to produce perovskites nanocrystals with a better optical stability than previously achieved in literature, underling at the same time the role of the dilution on the stability of the sample.

The improved stability allows to use these emitters for further studies. In particular, guided structure as tapered nanofibers allow to collect the emitted photons in a efficient way using near field coupling and opening the path to obtain a compact, integrated guided source of single photons. While the coupling with other kind of emitters, such atoms [8, 9] and solid state emitters [10, 11, 12, 13], had already been shown in literature, this is the first time this coupling has been achieved using perovskite nanocrystals.

1.1.2 Structure of the manuscript

The manuscript is divided in four parts.

In the first chapter I will introduce basic concepts useful to understand the experimental work presented in the following. This involves a short introduction on quantum mechanics and quantum optics, useful to define single photon emitters and their interest. In particular, I explain why experimentally we consider to be dealing with a single photon emitter any time that the photon statistic shows that the second order autocorrelation function respects the following relationship $g^{(2)}(0) < 0.5$. I also briefly introduce various single photon emitters, specifically solid state single photon emitters, detailing different analysis that can be performed on these emitters in order to characterize them. I conclude the chapter with an introduction to guided and integrated optics, presenting its advantages respect to the free-space optics.

In the second chapter I describe the experimental details of my project. In particular. I introduce perovskite nanocrystals as single photon emitters, and present the setup I used to study their properties. I detail two different fabrication methods for these nanocrystals, and present a systematic study of their emission properties and stability.

In the third chapter I present the nanofiber platform, which will be coupled with a single nanocrystal. After an introduction on fibers and nanofibers theory, I describe the technique and the setup used to fabricate the nanofibers. Finally I explain the technique used to depose a single perovskite nanocrystal on a tapered nanofiber and show a measurement proving that the nanocrystal emits single photons directly inside the nanofiber.

In the fourth chapter I show some outlooks of these system. Firstly I discuss the possible improvements of the emitters that can be done by better controlling the perovskite nanocrystals fabrication. Also the use of different emitters, such single defects inside nanodiamonds, is envisioned.

Finally the manuscript is concluded with a french resume and an appendix describing the main code used for the data analysis.

In this chapter I introduce the theory that underlies our research: I will review the fundamental concepts on which our experiments are based on and their interpretation.

1.2 Quantum mechanics

The theory of Quantum Mechanics was developed at the beginning of the XXth century in order to explain different phenomena impossible to explain with a classical approach.

This brief introduction in which some basic concepts of quantum mechanics are recalled was inspired by two classical textbooks: the book written by Griffiths and Schroeter [14] and the one written by Sakurai and Napolitano [15].

In order to understand the differences between the classical and the quantum theories, it can be interesting to consider them from an axiomatic point of view. This is not the usual way to proceed, as most authors prefers to present the physics from a historical point of view, but it gives a rapid insight on the differences of the two theories. It is possible to define the classical theory as a theory in which the following axioms are valid:

1. at any time, the state of a particle can be specified by two variables $x(t)$ and $p(t)$ that forms a point in the phase-space

2. Any variable can be expressed as a function of x and p

3. The ideal measurement of a variable ω will result in $\omega(x,p)$ if the particle is in the state (x,p), and the measurement does not perturb the state.

4. State variables follow the Hamilton equations:

$$\dot{x} = \frac{\partial H}{\partial p}, \qquad \dot{p} = -\frac{\partial H}{\partial x} \tag{1.1}$$

In quantum mechanics partially different assumptions are made:

1. at any time, the state of a particle can be specified as a vector $|\psi(t)\rangle$

2. The classical variables of quantum mechanics are replaced by the hermitian operators X and P, with the following matrix elements:

$$\langle x|X|x'\rangle = x\delta(x-x') \tag{1.2a}$$

$$\langle x|P|x'\rangle = -i\hbar\frac{\partial}{\partial x}\delta(x-x') \tag{1.2b}$$

   To obtain the operator Ω corresponding to a generic variable ω, we use the classical definition with the substitution

$$\Omega(X,P) = \omega(x \to X, p \to P)$$

3. The ideal measurement of a variable corresponding to ω will results in one of the

eigenvalue ω of $\Omega(x,p)$ with a probability $P(\omega) \propto |\langle\omega|\psi\rangle|^2$. After the measurement, the system is projected on the state $|\omega\rangle$.

4. The state variables follow the Schrödinger equation:

$$i\hbar\frac{\partial}{\partial t}|\psi(t)\rangle = H|\psi(t)\rangle \tag{1.3}$$

where H is the quantum hamiltonian, obtained from the classical one with the substitution $H(X,P) = H(x \to X, p \to P)$

From these axioms, two specific points can be underlined. The first point is that the state is not anymore defined by two variables (x and p), but rather by a state-vector $|\psi\rangle$. Usually $|\psi\rangle$ lives in a Hilbert space with infinite dimensions.

The state vector contains a huge amount of information that is the starting point for the evolution of the system. The downside is that the measure process has the effect to destroy the biggest part of the information.

The other point to underline is that the measurement process is completely different from the classical one. If we measure ω in classical mechanics we obtain, for a particle in the state (x_0, p_0), $\omega(x_0, p_0)$: and this is quite straightforward. In the quantum mechanics case, we need first of all to obtain the operator Ω corresponding to ω with the substitution given by postulate 2: $\Omega = \omega(x \to X, p \to P)$. After that we need to determine the eigenvalues ω_i and eigenvectors $|\omega_i\rangle$ of Ω and to expand the vector $|\psi\rangle$ on the basis of eigenvectors of Ω. The measure will return as a result ω_i for a certain i; the probability to obtain it is given by:

$$P(\omega_i) = |\langle\omega_i|\psi\rangle|^2 \tag{1.4}$$

. What is counter-intuitive in the quantum mechanical approach is that in the general case, the result of a single measurement is not completely defined by the initial state of the system and by the measurement itself but, with the same initial conditions it will return different results with different probabilities. For no-specific reason we obtain from the measurement ω_i and not ω_j. In addition the measurement perturbs the system: if we repeat the measurement of Ω we will obtain again the same ω_i obtained before. The system now is in the state $|\psi'\rangle = |\omega_i\rangle\langle\omega_i|\psi\rangle$.

The fact that the measure perturbs the system can appear as an evidence: when a measure is performed in the laboratory, there is always something that perturbs the system in some ways. However, in the specific case of quantum mechanics, we are speaking about an ideal measure: no matter how careful the measure will be, there is no

way to measure Ω without projecting the system in an eigenstate of Ω. This behavior, known as the the collapse of the wave function is probably the most surprising behavior in quantum mechanics.

It is also useful to note that, due to the collapse of the wave function, position and momentum of a particle cannot be measured simultaneously. This consequence of the postulate is known as Heisenberg's uncertainty principle, and can be formalized with the following inequality

$$\sigma_x \sigma_p \geq \frac{\hbar}{2} \tag{1.5}$$

In equation (1.5) σ_x and σ_p are the incertainties on the position and on the momentum, while $\hbar$ is the reduced Planck constant. In consequence of the Heisenberg's uncertainty principle is impossible to follow the trajectory of a given particle at any time, even in principle. If multiple identical particles are present, as their trajectory cannot be followed, it is not possible to distinguish a particle from another one. Particles that, even in principle, cannot be distinguished are called indistinguishable.

This revolution of physics, born at the beginning of the XXth century, is at the basis of the explanation for several particular phenomena; the most known is maybe the photoelectric effect.

Nowadays, many applications are based on knowledge coming from the quantum theory, but do not use the quantum mechanical properties in elaborating the information. For example, modern electronics devices uses transistors, whose behaviour can be explained only with the use of quantum mechanics. However the information is stored and processed in a classical way. Recently, many applications that directly create and manipulate quantum states to process information have been developed. Between them we can name the following ones.

Quantum Key Distribution: It is based on the *no-cloning theorem* [16] witch states that it is impossible to make a copy of an unknown quantum state leaving the first one unaltered. From this, it is possible to establish a protocol to exchange secure keys and makes it possible to know whether a key has been intercepted by someone else. As opposed to classical cryptography systems that are based on the fact that to decrypt a certain information is too expensive, in terms of money and time, quantum cryptography based on quantum key distribution relies on a fundamental physical law and is for this reason way more secure. Moreover, we know now that possessing a faster computer could allow to decrypt classical cryptography, while this is not valid for quantum cryptography.

Quantum simulation: The idea here is to use a quantum system to simulate another one. This is particularly useful, due to the complexity of quantum mechanics, to obtain information on systems that are too complex to be simulated with a classical computer.

Quantum computation: A quantum computer uses quantum superposition and quantum interference to solve computational problems that are hard to solve with a classical computer. This does not mean that problems are impossible to solve with classical computers, but that the required time for solving a given problem will be too long: the ability to solve them in a reasonable amount of time with a quantum computer is called quantum supremacy or quantum advantage. In 2019 Arute *et al.* [17] working at Google claimed to have been able to solve with a quantum computer a problem that was impossible to solve with a classical one. However, there are still practical problems for the physical implementations of quantum computers, mainly connected to quantum decoherence and error correction, that still need to be solved.

The potential of the applications cited above has raised a growing interest from various public and private founders and all these fields are very active.

However, in order to implement these quantum technologies, there is a need to produce so-called quantum objects, systems with quantum properties that can store a quantum state and can be manipulated in different ways. This implies to have a system (for example a single photon, or a single atom) with an observable A that has two different eigenvectors, called $|0\rangle$ and $|1\rangle$ corresponding to two different eigenvalues a_0 and a_1. If we measure A on a generic $|\psi\rangle$ state we obtain either a_0 or a_1. In analogy this can be regarded as the equivalent of a bit of information in classical computers, where the information is normally encoded in two different values of tension, for example 5 V and 0 V: one is indicated conventionally with 1 and the other with 0. The huge difference in quantum information is that while the result of a measurement is either a_0 or a_1, the state $|\psi\rangle$ is generically given by

$$|\psi\rangle = \frac{1}{\sqrt{|\alpha|^2 + |\beta|^2}} \left(\alpha |0\rangle + \beta |1\rangle\right), \tag{1.6}$$

with $\alpha, \beta \in \mathbb{C}$, where $\mathbb{C}$ is the set of complex numbers. We note here that we have ignored any observable that is orthogonal to A, that will not be affected in any way by the measurement process. As the global phase is irrelevant, it is possible to rewrite

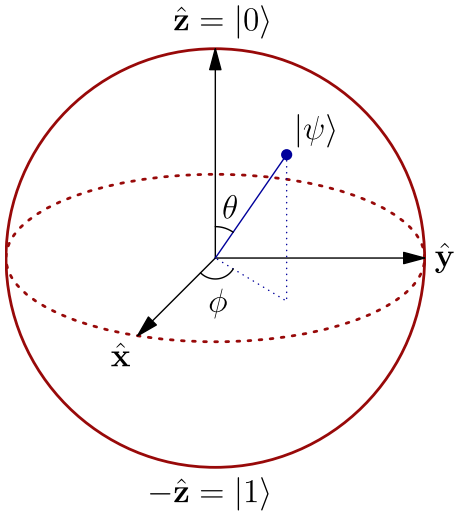

Figure 1.1 – Block representation of a qubit $|\psi\rangle$. All the points on the sphere correspond to a possible state vector $|\psi\rangle$ of the qubit. $\vartheta = 0$ corresponds to the state $|0\rangle$ while $\vartheta = \pi$ corresponds to the state $|1\rangle$.

equation (1.6) as

$$|\psi\rangle = \cos\vartheta\,|0\rangle + e^{i\varphi}\sin\vartheta\,|1\rangle \tag{1.7}$$

with $\vartheta, \varphi \in \mathbb{R}$ and $0 \leq \vartheta \leq \pi/2$ and $0 \leq \varphi \leq 2\pi$. The state $|\psi\rangle$ is usually called *qubit*, from *quantum bit* in analogy with classical computation and it is usually visualized as a vector in the Bloch sphere, represented in figure 1.1. All the points of the sphere corresponds to a possible state vector $|\psi\rangle$, in particular the top and the bottom point, respectively when $\vartheta = 0$ and $\vartheta = \pi$ are the corresponding states $|0\rangle$ and $|1\rangle$.

The described formalism as the advantage to be independent of the physical realization: this makes it possible to advance in theoretical and mathematical research without paying too much attention of the specific platform used in practice.

Nowadays, many platforms are being investigated such as trapped ions, trapped neutral atoms, superconducting qubits or electron spins in semiconductors. However, single photons and quantum photonics present a particular interest as they are ideal carriers for quantum information and as such holds a special place amongst the various platforms studied across the globe for quantum technologies.

1.3 Quantum Optics

Quantum optics is the study of light and light-matter interaction from the point of view of quantum mechanics.

It normally uses the formalism of second quantization, in which not only the physical quantities but also the fields are considered as operators. In the first quantization, each particle is associated with a wavefunction $|\psi\rangle$ with the result of having often more than one way to write the same global wavefunction. For example if we have two indistinguishable particles, the following notations are equivalent:

$$\psi_1 \otimes \psi_2 \qquad\qquad \psi_2 \otimes \psi_1 \tag{1.8}$$

To remove this ambiguity, they need to be symmetrized or anti-symmetrized, depending if the particles have a fermionic or a bosonic behaviour. In the second quantization approach we do not consider which particle is in which state but how many particles are in each state: this provides a more efficient way to deal with the problem. We can denote the state as:

$$|n_1, n_2, \cdots, n_\alpha, \cdots\rangle\,. \tag{1.9}$$

This notation holds also for the case in which no particle is present, i.e. the vacuum, indicated as $|0\rangle = |0, 0, 0, \cdots, 0, \cdots\rangle$. In addition, we can consider the case in which only one state contains particles ($|0, 0, 0, \cdots, n_\alpha, \cdots\rangle$) and this is called a single-mode Fock state.

Without entering into the details, it is now possible to define a photon as an excitation of the electromagnetic field from the quantification of Maxwell's equations. When we count single photons, in practice, we consider a Fock state.

1.4 Single photon emitters

1.4.1 Theory and definition

By *single photon emitters* we indicate any object that emits not more than one photon at each given time. Theoretically the simplest single photon emitter we can think to is a two level system: when it is excited from the ground state to the excited state it needs a certain amount of time to relax again in the ground state while emitting a photon. Until this photon is emitted, it is not possible to excite it anymore. In practice this object has a more complex structure, with more energy bands and levels and ideally one energy gap between them. We can then optically excite the emitter with a more energetic light that can be absorbed by the emitter. The recombination of the excited carriers is divided into two parts: a radiative recombination, when the photon is emitted, and a non-radiative recombination where some energy is lost somehow. This leads to the fact that the emitted

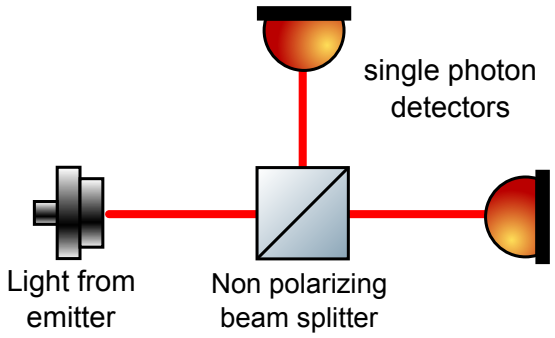

Figure 1.2 – Schematic setup to measure the $g^{(2)}(\tau)$. The non-polarizing beam splitter divides the beam in two equal parts. The light is then detected by avalanche photodiode (APD) detectors.

photon is usually at a different wavelength than the excitation beam, allowing an easy way to separate them by filtering the light using spectral selective optical elements.

To characterize the single photon emission of an object, we perform a measurement using the setup represented in figure 1.2. Before defining rigorously what is happening, let us try to explain it in easy words. Let us imagine photons coming from the emitter acting like a particle for this example and passing through a 50/50 non-polarizing beam splitter: if we have only one photon, it can not be divided and it will go in the first detector or in the second one but never in both. On the other hand, if we have many photons coming at the same time, there will be approximately half of them going to the first side and half going to the other one. Then, if we look to the function that describes the number of coincidences, i.e. the number of photons detected by the two detectors as a function of the delay τ from one detected photon on one detector and one on the other one, it has to go to zero at zero delay when we are in presence of a true single photon emitter. This simple argument provides a qualitative insight in the single photon emission but is not enough for a full understanding of this behavior. To explain it better we need to introduce a mathematical description, starting from a classical point of view.

1.4.2 Semiclassical approach

The semi-classical theory uses the quantum theory to describe the interaction of light with the detector and with the atoms and the classical theory for the treatment of the field [18]. It gives us a better understanding of the single photon emission.

Let $\vec{x}$ be a point in space-time, $\vec{x} = (\vec{r}, t)$. In the framework of the semiclassical theory, we can represent the light field as a complex signal $V(\vec{x})$ as well as the light intensity as

$I(\vec{x}) = |V(x)|^2$.

To characterize the fluctuations in two points in space-time, we can use the amplitude correlation function and the intensity correlation function:

$$G^{(1)}(\vec{x}_1, \vec{x}_2) = \langle V^*(\vec{x}_1) V(\vec{x}_2) \rangle \tag{1.10a}$$

$$G^{(2)}(\vec{x}_1, \vec{x}_2) = \langle I(\vec{x}_1) I(\vec{x}_2) \rangle \tag{1.10b}$$

and their normalized versions

$$g^{(1)}(\vec{x}_1, \vec{x}_2) = \frac{G^{(1)}(\vec{x}_1, \vec{x}_2)}{\sqrt{\langle I(\vec{x}_1) \rangle \langle I(\vec{x}_2) \rangle}} \tag{1.11a}$$

$$g^{(2)}(\vec{x}_1, \vec{x}_2) = \frac{G^{(2)}(\vec{x}_1, \vec{x}_2)}{\langle I(\vec{x}_1) \rangle \langle I(\vec{x}_2) \rangle}. \tag{1.11b}$$

At this point it is useful to recall the Cauchy-Schwarz inequality:

Cauchy-Schwarz inequality. *Given two vectors $\vec{u}$ and $\vec{v}$ of a inner product space, the following inequality is true*

$$|\vec{u} \cdot \vec{v}| \leq |\vec{u}| \, |\vec{v}| \tag{1.12}$$

Making use of this relation, and considering that the expression contains functions of real numbers and the inner product between these functions, it is possible to show that

$$g^{(2)}(\vec{x}_1, \vec{x}_2) \leq \sqrt{g^{(2)}(\vec{x}_1, \vec{x}_1) \, g^{(2)}(\vec{x}_2, \vec{x}_2)} \tag{1.13}$$

Experimentally, we measure the function $g^{(2)}(\tau)$ defined as

$$g^{(2)}(\tau) = g^{(2)}(\vec{r}, t, \vec{r}, t + \tau). \tag{1.14}$$

From equation 1.13 and equation 1.14 we can conclude that for classical light

$$g^{(2)}(0) \geq g^{(2)}(\tau) \tag{1.15}$$

In case of $g^{(2)}(0)$ is bigger than $g^{(2)}(\tau)$ for any $\tau > 0$ we say that the light is bunched, if $g^{(2)}(\tau)$ is constant the light is called unbunched, while if $g^{(2)}(0)$ is smaller than $g^{(2)}(\tau)$ for $\tau > 0$ the light is called antibunched [18]. Due to the normalization, $\lim_{\tau \to \infty} g^{(2)}(\tau) = 1$, then the light is bunched if $g^{(2)}(0) > 1$. In other words, in the semiclassical approach the $g^{(2)}$ function can only be bunched or unbunched. An ideal coherent light is unbunched, and $g^{(2)}(\tau) = 1$ for any τ, while the thermal light from a light bulb is bunched.

1.4.3 Quantum theory of coherence

In the quantum theory of coherence [19] correlation functions are expressed in terms of the electric field operators $\hat{E}^{+}(\vec{x})$ and $\hat{E}^{-}(\vec{x})$, that represent the positive and negative frequency parts, respectively. Indicating by $\hat{\varrho}$ the density matrix operator, we can redefine functions 1.10 in the following way:

$$G^{(1)}(\vec{x}_1, \vec{x}_2) = \mathrm{Tr}\left\{\hat{\varrho}\hat{E}^{-}(\vec{x}_1)\hat{E}^{+}(\vec{x}_2)\right\} \tag{1.16a}$$

$$G^{(2)}(\vec{x}_1, \vec{x}_2) = \mathrm{Tr}\left\{\hat{\varrho}\hat{E}^{-}(\vec{x}_1)\hat{E}^{-}(\vec{x}_2)\hat{E}^{+}(\vec{x}_1)\hat{E}^{+}(\vec{x}_2)\right\} \tag{1.16b}$$

and their normalized versions $g^{(1)}(\vec{x}_1, \vec{x}_2)$ and $g^{(2)}(\vec{x}_1, \vec{x}_2)$ can be defined by analogy with the semi-classical case. The main difference in this case is that we cannot interpret anymore $g^{(2)}(\vec{x}_1, \vec{x}_2)$ as a normalized statistical correlation function of the optical intensity; for this reason we cannot apply anymore the Cauchy-Schwarz inequality (1.12). As a conclusion, in the quantum case the $g^{(2)}(\tau)$ function defined by analogy by the function (1.14) is not anymore bounded to be at least one when $\tau = 0$. Finding $g^{(2)}(0) < 1$ is indeed a behavior that can be explained only in quantum theory of coherence and for that reason we usually address to it as "quantum light".

1.4.4 Single photon emission

As we defined in the previous section, any antibunched light has to be regarded as "quantum light", as there is no classical explanation for it. In the presence of quantum emission we can look at the $g^{(2)}(\tau)$ function in more depth, to understand how many photons are emitted. In particular it is possible to show [20] that:

$$g^{(2)}(\tau) \geq 1 - \frac{1}{\langle n \rangle} \tag{1.17}$$

where $\langle n \rangle$ is the mean photon-number. This is valid for any $\langle n \rangle \geq 1$. From the previous equation we deduce that only $g^{(2)}(0) = 0$ can ensure that $\langle n \rangle \leq 1$ and describe a "pure" single photon emission. Experimentally, in practice, we measure the value of $g^{(2)}(0)$ to conclude on the quality of a single photons emitter. The smaller $g^{(2)}(0)$ is, the less probable is to have more than one photon emitted at each time. Anyway if

$$g^{(2)}(0) < 0.5 \tag{1.18}$$

the mean number of photons emitted is smaller than 2 and we can consider to deal with a single photon emitter. In the following, any emitter that satisfies the inequality 1.18 will be considered as a single photon emitter.

1.4.5 Experimental limitations

In the theoretical analysis, we never had the need to introduce the setup represented in figure 1.2. For the theory, indeed, it is only needed to measure the photon statistics emitted, and a unique single photon detector with no beam-splitter should be enough. In order to perform a correct measurement of $g^{(2)}(0)$ this detector should be able to detect two photons arriving at the same time: this could be possible with photon-resolved single photon detectors, but it is not possible with common avalanche-photodiode single photon detectors we use (Excelitas SPCM-AQRH-14-FC). In our case, after a photon arrives onto one detector, there is a reset time in which the detector is off until it is capable of receiving and detecting the next photon: this dead-time is about 25 ns.

To avoid such problem the most common solution is to split the signal into two parts using two different APDs, one for the so-called start signal and another one for the so-called stop signal. This method has the disadvantage to reduce the rate of collection of the data but allows to measure correctly the $g^{(2)}(0)$. It is important, for the future understanding, to keep in mind that in any experimental measurement of the function (1.14), τ will be considered as the delay between a start event detected by one APD and a stop event detected by the other APD.

1.4.6 Examples of single photon emitters

An ideal single photon source should be able to produce deterministically on-demand indistinguishable single photons (as defined in section 1.2). In practice, multiple approaches have been studied to realize such a source, each of them presenting advantages and disadvantages.

We can subdivide them in two groups [21]:

Stochastic single photon generation : in this approach, one of the most interesting techniques is to use a laser and a non linear crystal in order to obtain pairs of photons using the so-called spontaneous parametric down-conversion effect (SPDC).The laser intensity has to be weak in order to generate in average not more than one pair of photons. The advantage of this technique is the possibility to use one photon of the pair to know when they are generated, and for this reason they

are called heralded single photons. Upon this technique rely various devices used for quantum key distribution applications. Unfortunately, such device produces single photons only when we require from them a low photon rate. In addition, they are not deterministic as the time at which the photon pairs will be emitted is not known. Different solutions have been proposed to tackle this problems, such as using multiplexed photons to increase the single-pair emission rate without increasing the probability of multiple pair emission [22, 23, 24, 25] or storing the emitted photons to use them on-demand at later times.

Deterministic single photon sources: in this approach, already mentioned, the aim is to find a single photon source that can work as a deterministic single photon emitter. Multiple alternatives have been explored such as single neutral atoms, single trapped ions, single molecules, different kind of quantum dots, single color centers in diamonds and nanodiamonds.

During my work I studied different emitters from the second group, and I will concentrate on such systems in the following. Indeed, differently from an attenuated laser that has a poissonian statistics, these sources can provide true single photons. I proceed to describe some different kinds of *deterministic single photon sources*.

Single neutral atoms

They have the advantage of repeatability as each atom is identical to the others (they are slightly 'different' in practice due to different environments), but they are challenging to operate with. The most used atoms for this application are alkali atoms [26, 27, 28, 29, 30, 31, 32]

They are usually used in a regime of strong coupling with a cavity that allows to efficiently collect emitted photons. The atoms are first trapped in a magneto-optical trap; then the trap is switched off and the atoms falls inside a cavity with the help of gravity. Once they fell into the cavity, another optical trap is turned on to keep them in place. This operation is, of course, experimentally challenging and space consuming, which poses limitation to future scalability of this source for quantum technologies.

Such atoms usually are three level systems, with two ground states $|g_1\rangle$ and $|g_2\rangle$ and an excited state $|e\rangle$. The optical cavity is resonant to the transition $|g_1\rangle \rightarrow |e\rangle$, so that the excited state, thanks to the Purcell effect[33], tends to decay in the $|g_1\rangle$ state. The pumping laser is set to the transition $|g_2\rangle \rightarrow |e\rangle$, while the population is moved from the state $|g_1\rangle$ to the state $|g_2\rangle$ via stimulated Raman adiabatic passage [34].

Single ions

The single photon emission mechanism is similar to the one for single atoms, with the difference that single ions can be trapped using a radio-frequency ion trap. The trapping is simpler in respect to the optical trapping needed for single atoms, and the position of the ion can be set with a precision of few nanometers.

As in the case for atoms, ions are identical and the reproducibility of emitted photons is ensured. Multiple ions can also be controlled in a singular trap[35, 36, 37], but it is difficult to efficiently collect the emitted photons.

Quantum dots

Quantum dots semiconductors can be split into two different groups:

- quantum dots grown by epitaxial methods on a bulk material;
- colloidal quantum dots, obtained in solution using a chemical synthesis.

The mechanism is different in respect to single atoms/ions. In this case, the small size results in a discrete level structure. When excited by a pumping laser, one or more excitons are produced. The excitation can be performed optically, usually non-resonantly with the emission, or electrically. Usually some internal mechanisms allow for the non-radiative recombination of most of the excitons produced, except one, resulting thus in a single photon emission. In the next sections, I will describe in more details the strong and weak points of colloidal quantum dots.

Color centers in diamonds and nanodiamonds

Newer than the others in the single photon emitters use, they are based on a defect in the crystal structure of diamond [38]. The emission mechanism is similar to the quantum dots, the defect creates a multiple level energy system that can be excited out (or in-) of resonance in order to produce single photons. The main advantage, compared to colloidal quantum dots, is that they are optically stable. In addition, differently from epitaxial quantum dots, they can emit at room temperature. They are naturally present in diamond, but they can also be artificially created at a certain place using laser writing techniques[39]. Diamond has a high refraction index and photon extraction can be difficult. In order to overcome this issue and use this kind of sources with glass-based platforms, single defects in nanodiamonds are being developed. One of the main

problems with this approach is that they are not easy to fabricate. Controlling the composition and the nanometric size of nanodiamonds is challenging. The easier defect to create in nanodiamonds is the Nitrogen-Vacancy (NV)-center and multiple studies have shown their capabilities as single photon emitters. At room temperature, the emission spectrum of a NV center is very broad. In addition, crystal strain can affect the emission wavelength and that pose some issues when we want to couple them together.

Other kinds of defects, such as the Silicon-Vacancy (SiV) center, have also shown single photon emission [40], but are even more difficult to produce in nanodiamond shape [41] and, as in the NV case, they can suffer from crystal strain present in the lattice [42].

As I have shown, different kinds of single photon emitters exist. Existing works at the LKB and L2n focus on the study of CdSe/CdS rod-shaped quantum dots. During my thesis, I worked with CdSe/CdS rod-shaped quantum dots even though I concentrated my studies on perovskites quantum dots, a new kind of quantum dots from perovskite nanocrystals. I describe them in more details in chapter 2. I also had the opportunity to perform some preliminary studies using NV^- and SiV^- color centers in nanodiamonds. These emitters and their characteristics are described in more details in chapter 4.

1.5 Common characteristics of solid state single photon emitters

A solid state single photon emitter is an object of nanometric size made by a semiconductor material or that presents a semiconductor-like level structure. When it is excited with the correct wavelength, an electron can jump from the valence band to the conduction band. In the relaxation process, there is emission of light and the color emission depends on the energy gap. When one electron is in the conduction band, it leaves a corresponding hole in the valence band. We can now define the notion of exciton: an exciton is a neutral quasi-particle, formed by the bounding of an electron and a hole. It can be seen as an elementary excitation of condensed matter.

Different mechanisms can be present in a solid state single photon emitter that allows only a single photon to be emitted at a given time: the most important of them for colloidal quantum dots is probably the Auger Effect.

In this section I will explain the mechanisms common to most of the solid states single photon emitters, making reference, when useful, to some studies performed at

the LKB in the past.

1.5.1 Non radiative recombination

As opposed to radiative recombination processes, a non radiative recombination allows the annihilation of an exciton without the emission of photons. These processes are present in quantum dots, as well as in semiconductors in general, and are important to understand the dynamics of the system. The most important ones are:

- Auger recombination,
- exciton-phonon interaction,
- charge trapping.

I briefly describe these effects below, starting form the most important in our case of colloidal quantum dots, the Auger recombination.

Auger recombination

Auger recombination is a mechanism present in semiconductors analogous to the Auger effect [43] in atoms. The Auger effect[43] is the second ionization of an atom due to the energy transferred by an electron of the atom itself: the process is shown in figure 1.3. It happens in two steps:

- The atom is first ionized, i.e. by an ionizing radiation and as a consequence of this ionization, a hole is present in one of its inner shells
- One electron relaxes from an outer level to the hole while another "collects" its energy and is emitted

In Auger recombination there is a similar effect: an exciton in a semiconductor recombines giving to a carrier in the valence band its energy. As opposed to the Auger ionization, this time the carrier that collects the charge stays in the conduction band at a higher level state and no-ionization happens. The carrier can then relax non radiatively to the ground state of the conduction band.

This mechanism is important in quantum dots as it often guarantees single photon emission. Indeed, if more than one exciton is created, the excitons in addition to the first one, can recombine non radiatively giving their energy to the first one. The Auger recombination is usually a very efficient mechanism: until the Auger recombination

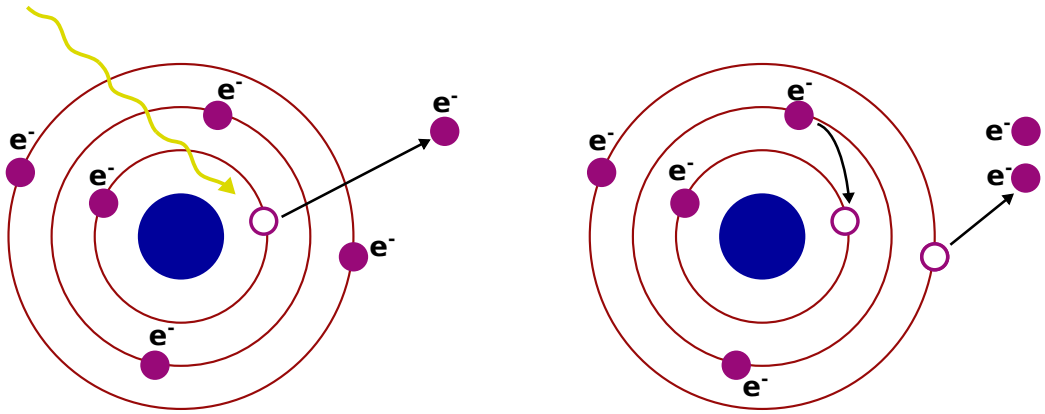

(a) (b)

Figure 1.3 – Mechanism of Auger ionization: (a) The atom is ionized by a radiation (i.e. a γ ray) and looses one of its electrons of the inner shell; (b) One outer electron relax to the hole left by the missing electron giving its energy to an outer electron and the atom is ionized for the second time.

is possible, it is predominant on the radiative recombination. When only one exciton is present, there are no more carriers in the conduction band to which the energy of the exciton can be passed on, and the Auger effect is not possible anymore; this time, the exciton relaxes radiatively with the emission of one photon. The scheme of this mechanism is shown in figure 1.4.

It has been shown for different kinds of quantum dots that this mechanism scales linearly with the volume of the quantum dot [44, 45]. This property, known as 'V-scaling', is the main reason of why Auger recombination is so effective in colloidal quantum dots.

Interaction of excitons with phonons

A phonon is a quasi-particle that represents the elementary vibrational excitation of a lattice. We can distinguish two different cases: one is the case of intraband relaxation and the other one is the case of interband relaxation.

Intraband relaxation: the fact that electrons and holes can relax giving energy in a semiconductor seems normal, although with a deeper thinking, it is quite surprising. Indeed, as well as for electrons and holes, phonon energy levels are also discrete due to the quantum confinement. As a consequence, except in the unlikely case of energy overlap, the transfer of energy from an exciton to a phonon should be prohibited. On the contrary, it was observed that the thermal relaxation is even accelerated by the quantum confinement, with a relaxation time that can

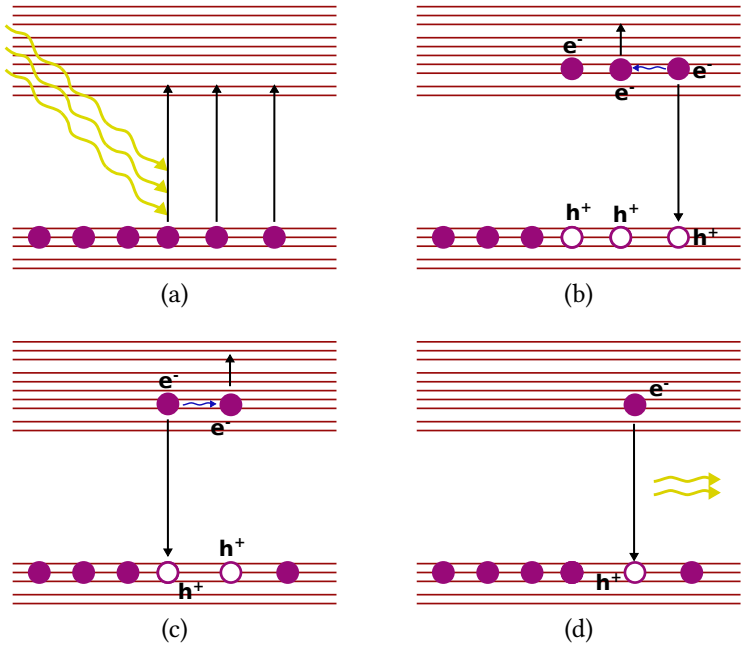

Figure 1.4 – Mechanism for Auger recombination: (a) The semiconductor is excited by light and multiple excitons are created; (b) and (c) until mutiple excitons are present, one exciton can relax non-radiatively passing the energy to another one; finally (c) the last exciton relaxes radiatively by emitting a single photon with the energy of the gap.

be ten times faster in a nanocrystal than in the bulk material [46] in CdS/CdSe. This is due to the fact that this process is mediated by the Auger energy transfer from electrons to holes. The process is usually very fast, on the order of hundreds of femtoseconds (compared to some nanoseconds for the radiative decay) and this is the reason why all the emission happens at the lowest energy and we see only one emission peak.

Interband relaxation: phonons have an effect also in interband relaxation, in two distinct ways. First, they affect the spectrum by broadening the emission peak and secondly they create a non-radiative relaxation channel that is in competition with the radiative one.

Charge trapping

A carrier can be trapped onto a defect of the lattice or at the surface of the nanocrystal. When this happens, it creates additional energy levels within the gap of the semiconductor providing a non radiative decay path and, as a consequence, no photon is emitted by the nanocrystal.

A trapped state can last from tens of picoseconds up to several seconds and its desexcitation is usually non radiative.

This is however a reversible process, as opposed to chemical reactions that provoke a permanent bleaching of the emission, i.e. the emitters do not emit light any more and they become completely dark.

1.5.2 Saturation

A typical effect present in deterministic single photon emitters is the saturation of the emitted intensity. In case of nanocrystals this is an effect of Auger recombination. If we imagine to start at zero excitation intensity, no excitons are created in the nanocrystal. When the excitation power increases, one or more excitons are created in the nanocrystal. At first, the probability to create one or more excitons with a single pulse increases but at a certain point it is almost certain to create one exciton and the excitation light pulse can create two or more of them. Increasing the excitation power will create more excitons at the same time. As already mentioned, ideally only one of them can emit light while the others recombine non radiatively. For this reason, the emitted intensity saturates and, up to a certain point, exciting with a higher intensity does not imply a higher number of photons emitted. If we report on a graph the emitted intensity as a function of the excitation intensity, we obtain a curve described by the equation:

$$P_{PL}(I) = P_{sat} \cdot \left(1 - e^{-\frac{I}{I_{sat}}}\right) \tag{1.19}$$

This equation is valid if the Auger recombination is efficient enough. The saturation intensity I_{sat} corresponds to the intensity at which, on average, an exciton is created for each excitation light pulse. In case of a not-so-efficient Auger effect, the equation (1.19) needs to be modified adding a linear term and becomes

$$P_{PL}(I) = P_{sat} \cdot \left(1 - e^{-\frac{I}{I_{sat}}}\right) + B \cdot I \tag{1.20}$$

The shape of the two curves is shown for comparison in figure 1.5.

1.5.3 Emission Lifetime

We have seen, talking about Auger Effect, that the decay rate γ plays an important role for single photon emission. It is thus possible to measure the decay rate associated to the emission via a lifetime measurement corresponding to the spontaneous emission of

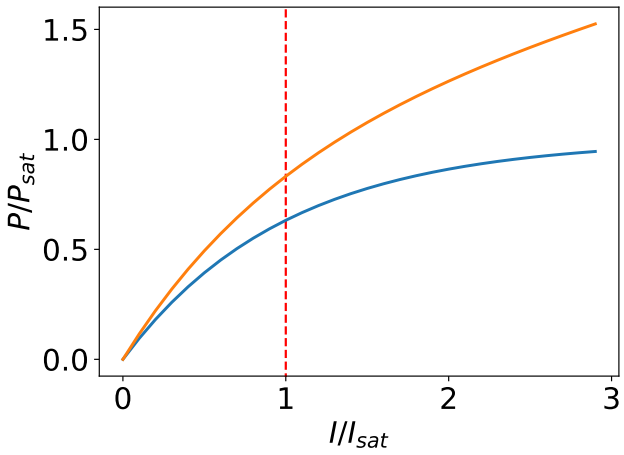

Figure 1.5 – In blue, plot of the saturation curve described by equation (1.19). In orange, plot of the saturation curve described by equation (1.20), where $B = 0.2P_{sat}/I$.

the emitter. If we call γ_r the radiative decay rate, the lifetime of the emission τ_r is defined as:

$$\tau_r = \frac{1}{\gamma_r} \tag{1.21}$$

This can be measured using a time correlated single photon counting (TCSPC) measurement. In practice, exciting the emitter with a pulsed laser, we detect at which time later from the excitation pulse the photon is emitted and we use it to create an histogram in time (an example is represented in figure 1.6). We can then fit it using an exponential decay function:

$$I = A \cdot e^{-t/\tau_r} \tag{1.22}$$

finding the lifetime of the emission τ_r. If multiple emission states are present, as often the case, multiple lifetimes are measured and equation (1.22) becomes:

$$I = \sum_i A_i \cdot e^{-t/\tau_i} \tag{1.23}$$

where i runs over all the radiative states. When the τ_i in (1.23) are of the same order of magnitude, experimentally distinguishing between the different times can be challenging.

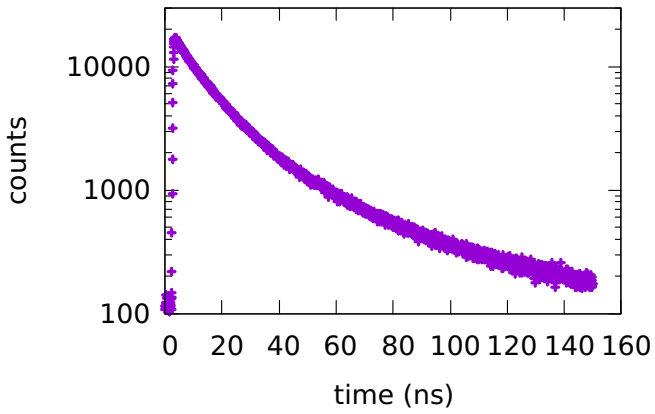

Figure 1.6 – Lifetime histogram obtained from a single CdS/CdSe dot-in-rod nanocrystal. Each point represents the number of photons that is impinging onto the detector at a certain delay. The histogram can be fitted by an exponential decay function (equation (1.23)).

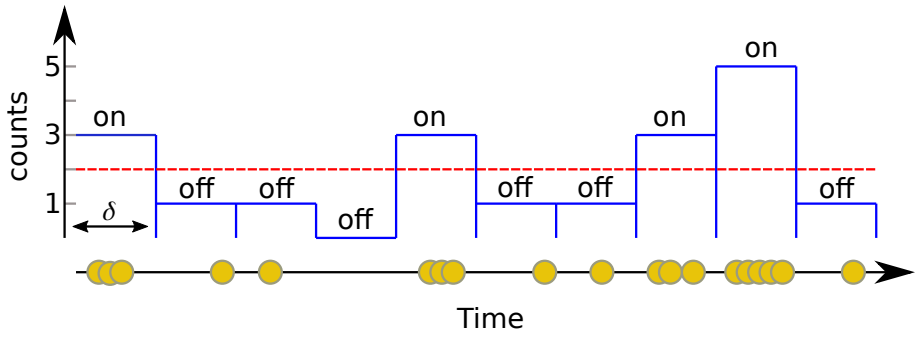

Figure 1.7 – Exemplification of the creation of the blinking trace. Each bin of the histogram reports the number of photons (in yellow) arrived at the time delay δ. A threshold is then chosen, I consider that the bin over the threshold are considered "on" while the bin under it are considered "off".

1.5.4 Blinking

Due to the charge trapping described in section 1.5.1, the emitter can become dark (or gray) for a certain time and recover its emission at a later stage. This phenomenon is known as blinking and has been largely studied.

There are different analysis that can be performed on blinking nanocrystals. I will detail some of them, knowing that they are not necessarily all applicable for our particular case.

Binning analysis

One of the most traditional way to study the blinking is to perform a time correlated single photon measurement or in other words to measure, with the help of a single photon detector, if a photon arrives and when it arrives. It is then possible to select a size for a temporal bin and to find out how many photons arrived within a specific bin. The result at the end is an histogram reporting for each time interval how many photons arrived. There are two different kinds of measurements that can be performed depending on the instrument: one directly provides the histogram, while the other one provides a list of photon arrival times with which it is possible to create the histogram.

Once we have the histogram, we can inspect the distribution of the intensities in each time bin. We can then analyse if the distribution of the on-states and the distribution of the "off"-states can easily be separated thus we can set a threshold in between. The probability for a state to stay "off" or "on" for a certain time is measured and noted $\mathcal{P}_{\text{off}}(t_{\text{off}} > \tau)$ and $\mathcal{P}_{\text{on}}(t_{\text{on}} > \tau)$.

In the case of the "off"-states, the probability $\mathcal{P}_{\text{off}}$ usually follows an inverse power-law distribution:

$$\mathcal{P}_{\text{off}} \propto \tau^{-\mu} \tag{1.24}$$

The "on" duration is also a power-law distribution but in this case an exponential truncation is usually observed:

$$\mathcal{P}_{\text{off}} \propto \tau^{-\mu} e^{-t/\tau_c} \tag{1.25}$$

The estimation of the parameter μ gives important information on the blinking. It is possible to distinguish three different cases depending on the value of μ:

$\mu < 1$
in this case the average value and the variance of the distribution $1/\tau_\mu$ are not defined, as all the momenta of the distribution diverge;

$1 < \mu < 2$
in this case, the mean value converges but not the variance;

$\mu > 2$
in this case, the mean value and the variance both converge.

Clearly the last case is the best one, while in the first case we cannot define a typical blinking time.

This kind of analysis is useful but it has some limitations. First of all, the bin size cannot be too small due to the need of having a good signal to noise ratio and/or a

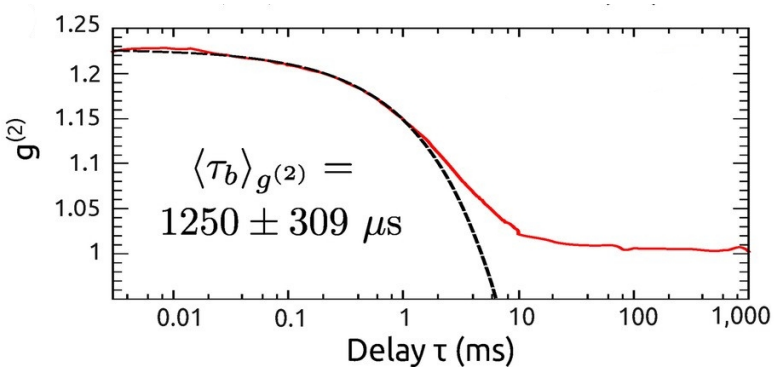

Figure 1.8 – Example of $g^{(2)}$ behavior as a function of the delay due to the blinking. The black dashed line is a fitting model using function (1.26), while the continuous line is the experimental curve. *(credits: Manceau* et al. *[47]).*

finite temporal resolution of the detector. This fact imposes limits in the minimum time measured in the distribution and possible switching between the "on" and "off" states occurring in this time is averaged out. Another problem is that the result is influenced by the choice of the bin size and by the threshold. It makes sense that the values of μ and τ_c are affected by these choice. This dependence is more evident when the "on" and "off" states are not well separated, while it is minimal if they are separated.

When two different states are present in the blinking trace, setting a threshold is also useful to separately study the lifetime of each of the states. This can be done when the acquisition card is able to record the arrival time of each photon. In this case it is possible to make a post-selection on the lifetime histogram events. We proceed as follows:

- first of all, we set a threshold dividing "on" and "off" states;
- we select only the events coming from one of the two states (i.e. the "on" state);
- we create the histogram only taking in consideration the photons arrived when the emitter was in the selected state.

With the described procedure it is possible to separately obtain the decay rates of the two states.

Intensity auto-correlation function

Another way to characterize the blinking properties is to use the intensity autocorrelation function $g^{(2)}(\tau)$ already described in section 1.4.1. Due to the fluctuation of the intensity induced by the blinking, the emission is typically super-poissonian and shows

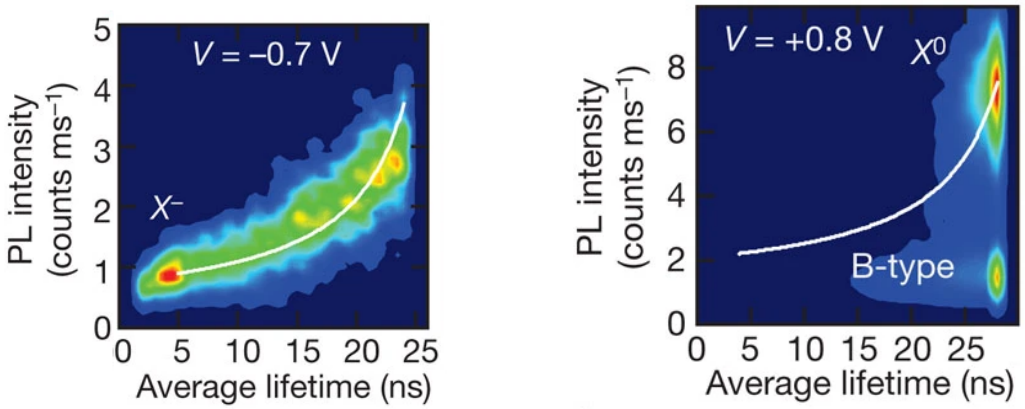

(a) (b)

Figure 1.9 – FLID: (a) in the presence of a type A blinking, the average lifetime depends on the emitted intensity; (b) in the presence of type B blinking the average lifetime does not depend on the emitted intensity. *(credits: Galland* et al. *[51]).*

photon bunching, except for low values of $g^{(2)}(0)$. For timescales smaller than the exponential cutoff, it is possible to express the $g^{(2)}(\tau)$ function as [48, 49, 47]:

$$g^{(2)}(\tau) = B\left(1 - A\tau^{1-\mu}\right). \tag{1.26}$$

where μ is the highest exponent amongst μ_{off} and μ_{on}.

In equation (1.26), B is the bunching value, i.e. the maximal value reached by the $g^{(2)}(\tau)$ (value that it takes at short timescales with respect to the characteristic blinking time). This model does not take account the presence of photon antibunching (single photon emission) that happens on much shorter times, i.e. on a nanosecond scale. The A coefficient is given by [49]:

$$A = \frac{1}{\langle\tau_b\rangle}\frac{\tau_{\text{min}}^{\mu}}{\Gamma(2-\mu)} \tag{1.27}$$

where $\langle\tau_b\rangle$ is the average duration of the bright "on"-states, τ_{min} is the minimal duration of an event and Γ is the Euler gamma function [50]. By fitting the correlation function, we can obtain information on the parameters B, A and μ. Unfortunately, the choice of the cutoff influences the result of the fit for the last parameter. There are possibilities to overcome this problem, one of them, as proposed by Manceau *et al.* [47] is to use the information from the residual of the fit.

Fluorescence lifetime intensity distribution

Often the signal is too low and the blinking too fast to allow the selection of a single state: this was the case for the perovskite nanocrystals that I studied and describe in the next chapter.

When it is impossible to select a single state in the blinking trace, it is more appropriate to talk about flickering [4, 51]. Usually, the study of this phenomenon is performed using the Fluorescence Lifetime Intensity Distribution (FLID) introduced for the first time in 2011 by Galland *et al.* [51]. This kind of study allows to distinguish between two different blinking types called A and B. As shown in figure 1.9, it is experimentally possible to distinguish between them as the A type blinking presents a clear dependence with the emission intensity and the fluorescence lifetime, while in B type blinking the fluorescence lifetime is independent of the emission intensity.

Galland *et al.* [51] used this technique to study the blinking dependence of the charged state, controlled with the use of a three electrode electrochemical cell. This technique is useful also in neutral conditions in order to identify the mechanisms involved in the blinking.

Physically, different kinds of blinking correspond to different relaxation mechanisms. In the case of type A blinking, the "on"-to-"off" switch happens when a carrier is moved to a trap state: this trapping usually happens via thermal ionization or Auger-assisted photo-ionization. The opposite process, "off"-to-"on" switch, happens when the carrier is released, typically via a relaxation process. This is shown in figure 1.10. It goes differently for the case of type B blinking as the intensity fluctuation is due to a fast trapping of high energy electrons followed by a non-radiative recombination of the electron and the hole. The luminescence is decreased due to this process, but it does not affect the lifetime of the emission as the trapping process is not in direct competition with the radiative recombination from the band edge. This mechanism is reported in figure 1.11.

1.5.5 Polarization

The polarization of a light beam is defined as the direction of oscillation of the electrical field and lays always on the plane orthogonal to the propagation direction. When the polarization changes are random we have non-polarized light. In this case, even if in each point of the space and in each moment of time, the polarization state is clearly defined, there is no relation with the polarization state that the light will have in the same point in a subsequent moment. This is the case for sunlight or in the case of incandescent

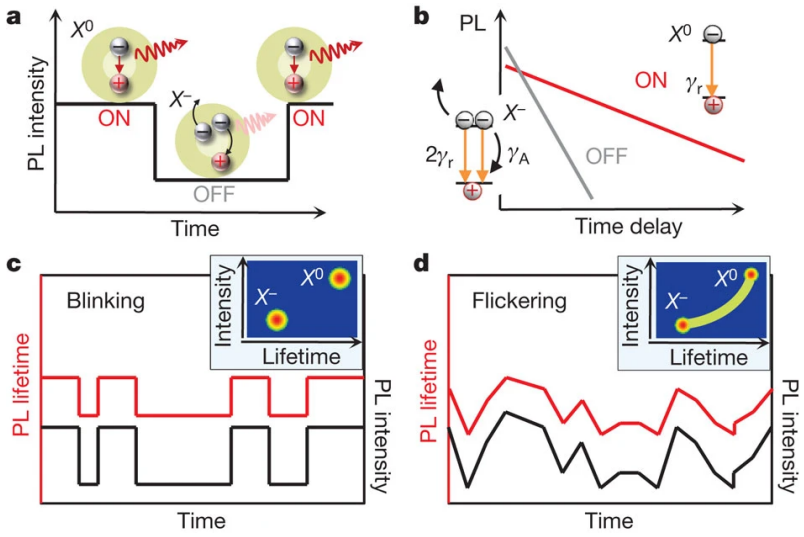

Figure 1.10 – Mechanism of type A blinking: a) the "on" periods corresponds to the neutral state, while the "off" period corresponds to the negatively charged excitation states. b) Different mechanisms correspond to different measured lifetimes c) in case of blinking between two well-separated states this behavior corresponds to two different spots in the FLID image, while (d) in presence of flickering a curve is visible on the FLID *(credits: Galland* et al. *[51]).*

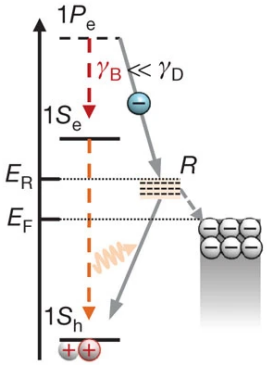

Figure 1.11 – Mechanism of type B blinking: The "off" periods are due to the presence of a relaxation center R that captures the electrons with a rate γ_D higher than the intraband radiative rate γ_r. *(credits: Galland* et al. *[51]).*

lamps.

For various applications, it is more useful to work with polarized light, that is light in which the polarization state follows a well defined temporal evolution, i.e. it is always on the same direction as in case of linearly polarized light. In order to describe such polarized light, we can use three different parameters: the two transverse components of the electromagnetic field and their relative phase. In the case where the light is not completely polarized, it is necessary to add the degree of polarization. This way we obtain four parameters, called the Stokes parameters.

There are several equivalent ways to represent the polarization of a light beam. The most commonly used are the following three: the polarization ellipse, the Poincare sphere and the Stokes parameters.

Stokes parameters: they allow to give a quantitative way of describing the state of polarization. Usually they are indicated by S_0, S_1, S_2, S_3. They represent respectively:

S_0 is the intensity,

S_0 is the degree of horizontal/vertical polarization,

S_2 is the degree of polarization at $\pm 45^{\circ}$,

S_3 is the degree of circular polarization.

It is convenient to consider a monochromatic light propagating along the z axis with the two components of the electric field given by:

$$E_x(z,t) = E_{0x}\cos\left(\omega t - \kappa z + \delta_x\right), \tag{1.28a}$$

$$E_y(z,t) = E_{0y}\cos\left(\omega t - \kappa z + \delta_y\right). \tag{1.28b}$$

In this case, the Stokes parameters, in terms of components of the electric field, are given by:

$$lS_0 = E_{0x}^2 + E_{0y}^2, \tag{1.29a}$$

$$S_1 = E_{0x}^2 - E_{0y}^2, \tag{1.29b}$$

$$S_2 = 2E_{0x}E_{0y}\cos(\delta), \tag{1.29c}$$

$$S_3 = 2E_{0x}E_{0y}\sin(\delta). \tag{1.29d}$$

For the case of fully polarized light the following relation is valid:

$$S_0^2 = S_1^2 + S_2^2 + S_3^2 \tag{1.30}$$

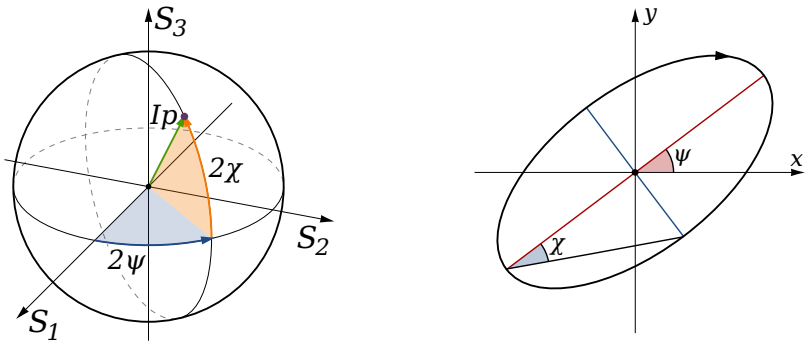

(a) (b)

Figure 1.12 – Different graphical representations of the polarization state of light. (a) Poincare sphere: the polarization is represented as a point on a sphere, the coordinates of the point are in relation with the Bloch vector following the equations (1.31). (b) Polarization ellipse: two dimensional visualization of the polarization, easier to report of a flat support than the Poincare sphere it contains the same amount of information. *credits: Wikimedia Common.*

Poincare Sphere: the polarization state of the light can be expressed in spherical coordinates and is given in this case by a point on the so-called Poincare sphere. To obtain the coordinates of a point given the Stokes parameters we can use the following relations:

$$\begin{aligned} I &= S_0 \\ p &= \frac{\sqrt{S_1^2 + S_2^2 + S_3^2}}{S_0} \\ 2\psi &= \arctan \frac{S_2}{S_1} \\ 2\chi &= \arctan \frac{S_3}{\sqrt{S_1^2 + S_2^2}} \end{aligned} \tag{1.31}$$

Polarization ellipse: this representation is useful as it gives an easy way to represent graphically the polarization. As opposed to the Poincare Sphere, it is a two-dimensional representation, easier to report on a screen or on paper. The polarization is represented as an ellipse. When the two semi-axis have the same length (then the ellipse coincides with a circle) the polarization is circular, when one semi-axis is equal to zero the polarization is linear (thus the ellipse is simply a segment).

The relation between the different graphical representations is shown in figure 1.12.

Working with single photons, the polarization is an important property, especially

when considering whether two photons are indistinguishable which means that they need to have the same polarization state. For this reason, for some quantum applications, it is important to obtain polarized single photons. Working with quantum dots as single photons emitters, their polarization properties are influenced by the asymmetries in their structure or in their shape. For example, CdS/CdSe dot in rods have a linearly polarized emission due to the elliptical shape of the shell and, subsequently, of the core [52, 53]. Nitrogen-Vacancy defects in nanodiamonds on the other hand have an asymmetrical molecular structure due to the defect itself, that results in partially linear polarized emission[54].

1.6 Guided and integrated optics

The advantages of guiding electrical fields and the enormous development and amount of innovation that the ability to guide and control the electrical field has brought is quite clear. Firstly, the use of conductors in controlling it has given the possibility to use its energy for many different applications. This affected our life at the point that nowadays it is almost impossible to imagine a world without this technology. What followed was the ability to transport and manipulate information using an electrical field and it has given rise to electronics and yet again changed the world with a revolution that is not yet finished. In the last two centuries, the life of people in the world has changed as never before.

It would seem that photonic applications are following the same path. They also contribute to changing our life as the electric and electronic revolutions did. The ability to transport light was initially used in medical applications (as explained in chapter 3), but it has recently shown its potential to control and manipulate information alongside electronics. The world has been connected by optical fibers and it has turned out to be an efficient way to transport information: this has increased the necessity to create integrated optical circuits and connections.

It is evident that for industry and practical applications, the integrated approach has some clear advantages over free-space optics:

- it is stable and not affected by misalignment. It does not need to be realigned after temperature changes
- it is compact

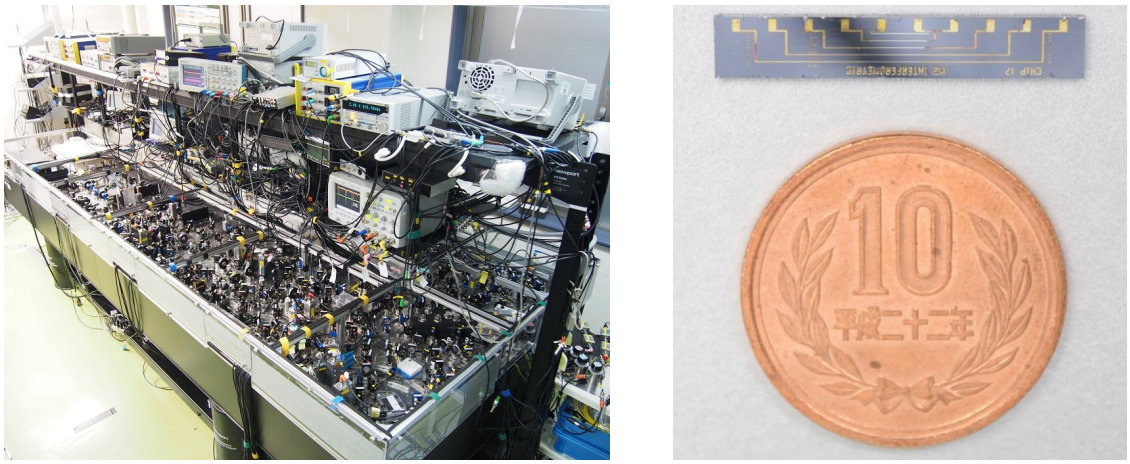

(a) (b)

Figure 1.13 – Difference between freespace (a) and integrated (b) optics. The free-space optics is flexible and historically well known, but requires fine alignment and wide space. On the contrary, integrated optics cannot be modified one fabricated, but it is small, stable and does not risk misalignment.

- it can be industrially replicated, once the project made, in multitude of identical parts

These advantages are evident as shown by figure 1.13.

In the domain of quantum information technologies, photons are one the most promising carriers of information. As an example, for quantum key distribution, the information is usually encoded in the quantum state of a photon. There is a clear interest in coupling single photons to guided and integrated optics. Multiple approaches are available to reach this goal, the most classical one is to use a microscope objective to couple photons directly into an optical fiber.

During my Ph.D. I had the occasion to work on a different approach, potentially more scalable: the near field coupling.

Multiple guided structures have been proposed in the last few years to be used for quantum technologies. We can classify them in three different groups [55]:

Dielectric waveguides: in this category, we count all the structures that guide the light using total internal reflection. The light is guided in a medium with a higher refractive index with respect to the surrounding medium. The most important and known members of this group is the optical fiber, but other members, such as Ion-exchange glass waveguides (described in the last chapter) are part of this group.

Photonic crystal waveguides: in this kind of guides the light is confined thanks to

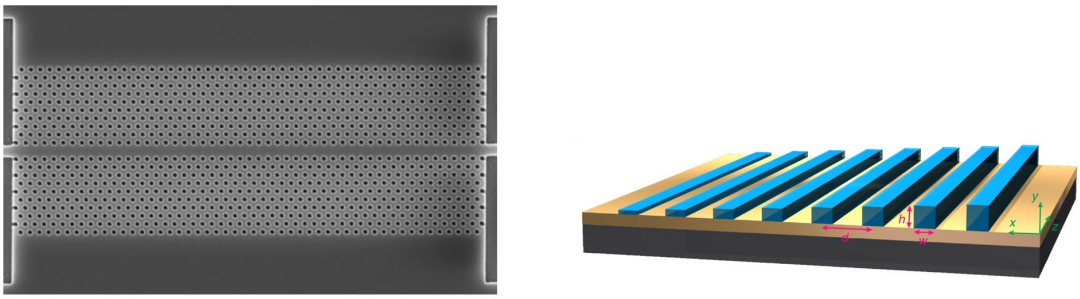

(a) (b)

Figure 1.14 – Sanning electron microscopy image of a photonic crystal waveguide array 1.14a *(credits: García-Rupérez* et al. *[59])* and scheme of an array of surface plasmon polariton waveguides (PMMA on gold surface) 1.14b *(credits: Block* et al. *[60]).*

the periodicity of the structure. Interestingly, this enables a sharp bending of the guide [56, 57] resulting in a slow group velocity for certain frequencies that can give origin to strong light-matter interactions. In addition, they have a narrow bandgap that allows the propagation of some selected frequencies only.

Surface plasmon polariton waveguides: these guides use the coupling of the electromagnetic field with the electron plasma of the conductor. The field is thus confined at a dielectric-conductor interface. They are interesting as they enable high confinement of the electromagnetic field [58].

We concentrated this PhD work on the study on two different kinds of dielectric waveguides. The main part of my work was dedicated to the optical tapered nanofibers, described in detail in chapter 3. I also studied the Ion-exchange glass waveguide that could overcome some nanofiber limitations: they are described in chapter 4.

Conclusions

In this chapter I presented the main concepts useful for understanding my PhD work:

- I introduced the basic concepts of quantum mechanics and explained why it is interesting to study the possibility of encode information in quantum states.
- I introduced photons and the interest to use them in such applications.
- I defined a single photon emitter, explaining how it is possible to recognize its emission and to measure it.
- I defined the polarization of light and explained the notation to identify it.
- Single photon emitters can be of several kinds, each with specific properties.
- In the characterization of nanoscale single photon emitters properties, it is important to take into account multiple properties:
  - their saturation intensity can give information on the mechanisms that generate the single photon emission;
  - their fluorescence lifetime gives information on their emission rate, on the transition involved in the emission and on the state of the emitter;
  - their blinking statistics gives information on the process that generates the emission.
- The previous mechanisms are also important as they greatly influence the possible applications that a single photon emitter can have in the future
- I have briefly introduced the interest of an integrated optics approach and some of the structures that have been proposed for this approach.

Chapter 2

Perovskite nanocrystals

Contents

2.1 Introduction . . . 36
2.1.1 Interest for perovskites . . . 36
2.1.2 Perovskite nanocrystals . . . 37
Level structure in perovskite nanocrystals . . . 37
Perovskite nanocrystals as single photon emitters . . . 38
Blinking properties . . . 39
Stability of the nanocrystals . . . 40
2.2 Experimental setup for nanocrystal characterisation . . . 42
2.2.1 Perovskite fabrication . . . 44
Sample A . . . 44
Sample B . . . 45
2.2.2 Sample preparation . . . 46
2.2.3 Experimental Setup . . . 46
2.3 Measurements . . . 50
2.3.1 Perovskite Spectra . . . 50
2.3.2 Saturation behaviour . . . 51
2.3.3 Polarization measurements . . . 53
2.3.4 $g^{(2)}$ measurements . . . 57
Acquisition . . . 58
Signal cleaning . . . 60
2.4 Stability . . . 62
2.4.1 Role of the polystyrene . . . 62
2.4.2 Role of the Sample preparation . . . 63
2.5 Blinking properties . . . 65

2.6 $g^{(2)}$ distribution 68

2.1 Introduction

Historically "Perovskite" was the name given to the mineral Calcium Titanium Oxide ($CaTiO_3$), discovered in the Ural mountains in 1893. It was named after Lev Perovski, a Russian mineralogist[61]. This mineral (represented in Figure 2.1a) had the peculiarity to present a particular cubic structure.

(a)

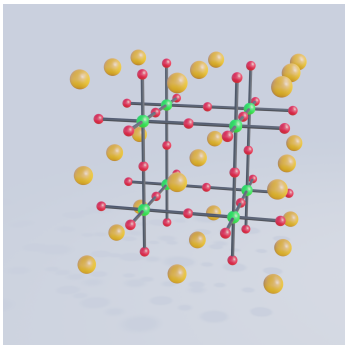

(b)

Figure 2.1 – (a) Crystals of perovskites in mineral matrix from Magnet Cove, Arkansas, USA. The cubic structure, particularly unusual for a natural compound, is clearly visible. *(credits Wikimedia Commons)* (b) 3D Structure of a perovskite (ABX_3): in red the X atoms, cations, in green the B atoms and in yellow the A atoms. Both A and B are metal cations, with B atoms smaller than the A ones.

In the following the name Perovskite is given to a class of materials with a structure similar to Calcium Titanium Oxide, most of which nowadays are synthetic. This structure, generally represented as ABX_3, is indeed peculiar to many oxides and usually takes the form ABO_3. They all present a structure shown in Figure 2.1b. The X atom is an anion, while both A and B are metal cations with A bigger than B.

In most of the perovskite natural compounds the anion X is oxygen: particularly $(Mg,Fe)SiO_3$ and $CaSiO_3$, known as Silicate Perovskite are largely present in the lower part of the Earth mantle.

2.1.1 Interest for perovskites

The particular structure of Perovskites give them peculiar characteristics that have been studied in different physical aspects.

It was first discovered that perovskites shows colossal magnetoresistance, that is the capability of a material to dramatically change their resistance in presence of a magnetic field[62]. Perovskites-like ceramics are used in superconductive applications, enabling to reach relative high superconductive temperature. What is particularly remarkable was the discovery in 1986 of the possibility that some of these materials have a critical temperature above 90 K.

From an optical point of view, perovskites have been studied for solar-cell applications. The first report of a perovskite-based solar cell was published in 2012[63] using $CsSnI_3$ and since then they have reached remarkable efficiencies, up to 24%[64]. Despite the high efficiency, the main problem of the stability is still open, as the perovskites undergo degradation if exposed to moisture or light. Meanwhile, other possible uses of perovskite semiconductors have emerged: particularly the possibility to produce perovskite nanocrystals has opened the possibility to use them as quantum dots in quantum optics applications.

2.1.2 Perovskite nanocrystals

Quantum dot nanocrystals are interesting to study for quantum optics. They allow to fabricate single photon sources, working at room temperature and they can be used deposited on a glass plate or integrated into different photonic structures such as nanowires[65] or nanofibers[66].

Perovskites nanocrystals maintain the advantage to be easy to fabricate and add the possibility to tune their emission playing on their shape and on their composition: this is a main advantage in comparison with other kinds of colloidal quantum dots such as Cd/CdSe quantum dots, that can also be tuned but can hardly reach ranges outside the visible one. Their main limitation is the optical stability but with different approaches we can obtain good improvements on this field, as I will explain later.

Level structure in perovskite nanocrystals

The energy level structure in perovskite nanocrystals is currently under experimental and theoretical investigations. The level structure of the Brillouin zone of a $CsPbBr_3$ nanocrystal is shown in figure

From the most recent results obtained on this topic, the perovskite level structure seems to differ from other kinds of emitters such as CdS/CdSe quantum dots. Even if the fact is still debated, some studies claim that perovskites have a bright ground state [68, 67] which seems to be due to the Rashba Effect. Moreover, they have a momentum

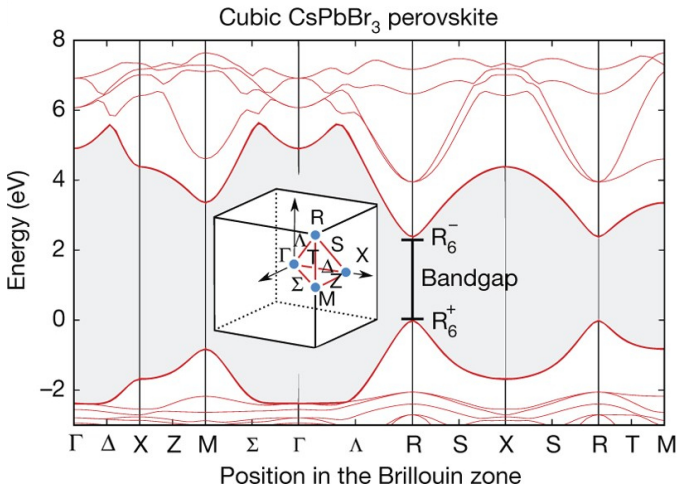

Figure 2.2 – Band structure of $CsPbBr_3$ perovskite, calculated by Becker *et al.* [67]. In the inset, the first Brillouin zone of a cubic crystal lattice is visible. *(credits: Becker* et al. *[67]).*

dependent splitting of the spin that can be derived using the perturbation theory and results in an additional term in the Hamiltonian of the form:

$$H_R = \alpha(\boldsymbol{\sigma} \times \mathbf{p}) \cdot \hat{z} \tag{2.1}$$

where $\boldsymbol{\sigma}$ is the Pauli matrix vector and α is the Rashba coupling. The Rashba effect influences only the Hamiltonian in the case of a weak confinement, while in the case of a strong confinement, it does not [68]. Finally, the hyperfine structure is influenced by the size of the nanocrystal and by the medium in which the nanocrystal is immersed [68].

Perovskite nanocrystals as single photon emitters

Single photon emission from perovskite nanocrystals has been reported firstly by Park *et al.* [4] in 2015 with an experiment at room temperature. They describe single photon emission from perovskite nanocubes made of $CsPbBr_3$, $CsPbI_3$ and $CsPbBr_xI_{(3-x)}$. In particular, the last compound, where x can be any positive rational number smaller than 3, showed the flexibility of these materials. The emission spectra are reported in Figure 2.3a: it is clearly visible that changing the composition of the perovskites will modify the emission wavelength. In Figure 2.3b, we can see that the autocorrelation function $g^{(2)}(0)$ of the emitted light is very low and thus these nanocrystals are very good single photon emitters.

Given these facts it is not difficult to understand that the community has a big interest

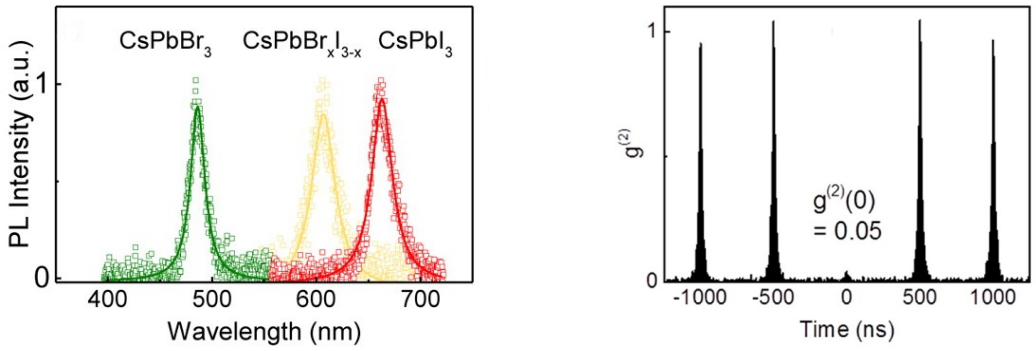

Figure 2.3 – (a) Different emission spectra with different composition of perovskite nanocrystals. (b) $g^{(2)}(\tau)$ measurement of light emitted from a single perovskite nanocrystal, excited with a pulsed laser. *(credits: Park* et al. *[4]).*

in this kind of materials for single photon applications and that multiple studies have analyzed their emission from a quantum optics point of view in the last few years.

Blinking properties

Like other kinds of quantum dots, these emitters do blink. From what is reported in Park *et al.* [4], the blinking is the intermittency of the intensity luminescence between a dark and a gray state: this is evident from the luminescence of a single $CsPbBr_3$ nanocrystal trace reported in Figure 2.4 [4]. In this case the signal is binned every 1 ms and it is

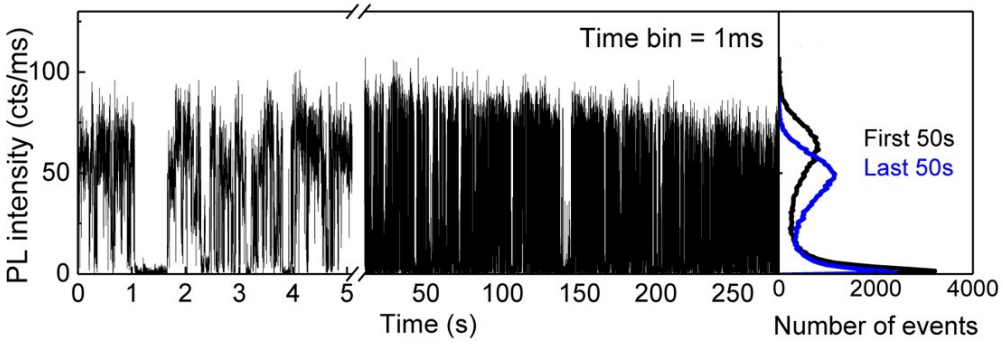

Figure 2.4 – On the left, the luminescence trace of a single perovskite $CsPbI_3$ nanocrystal: it is clearly possible to distinguish two different states, a bright one and a dark one. The binning is 1 ms. On the right the histogram of the first and the last 50 s, showing a degradation of the signal. *(credits: Park* et al. *[4]).*

possible to distinguish in this case between two different emission levels normally called bright and dark states.

As already shown, the blinking is normally due to two or more different states and can be categorised in type A and B blinking. To have a deeper understanding of this blinking behavior, it is possible to look at the FLID images: here the relation between the blinking and the intensity emission is evidenced, as explained in section 1.5.4 at page 26.

In figure 2.5 we can see a measurement of this type performed by the authors of [4]. In the first panel (figure 2.5a) it is possible to see the correlation between the blinking trace (upper part), obtained in this case with a bin size of 50 ms and with a pulsed laser, and the evolution of the mean lifetime (lower panel). We know the lifetime indicates the delay from the moment when the emitter is excited and the moment when a photon is emitted by spontaneous emission. The mean lifetime in this case is the arithmetical mean of the lifetimes of all the excitation-collection events registered in a certain time interval, corresponding to the bins of the histogram. In this case, as the binning is larger than the blinking characteristic time, we talk about flickering. The authors supposed two different states to be present. By only taking the photons arrived in the lower part of the intensity trace (between the green and the blue lines respectively), they created an histogram to deduce the lifetimes of the two different states: the neutral one, with a lifetime of $\tau_x = 13.6\,\text{ns}$, and the charged one, with a lifetime of $\tau_{x^*} = 13.6\,\text{ns}$. This histogram is represented in figure 2.5b. They then reported the FLID images for different excitation powers, using τ_x and τ_{x^*} to deduct the state that is mostly probable as a function of the mean number of excitons created in each pump pulse, indicated by $\langle N \rangle$. In Figure 2.5c-f we can see that the probability for the emitter to be in the "on" state decreases as they increase the excitation power, having with $\langle N \rangle = 0.01$ 98% of probability to find the emitter in the off state.

In addition to this analysis, looking at Figure 2.5, we can deduce that the emission lifetime depends on the emission intensity. This is evident from the FLID images and tell us that we are in the presence of a type A blinking.

Stability of the nanocrystals

Unfortunately there are some limitations that make difficult to use such emitters for practical applications. The main one is the stability as underlined for solar-cell applications. Perovskites are degraded by moisture and light and this is true even more for nanocrystals, which have by definition a big surface/volume ratio.

It has been observed that by exciting perovskite nanocrystals, their structure progressively degrades, starting from the external layers. This can be seen looking at the

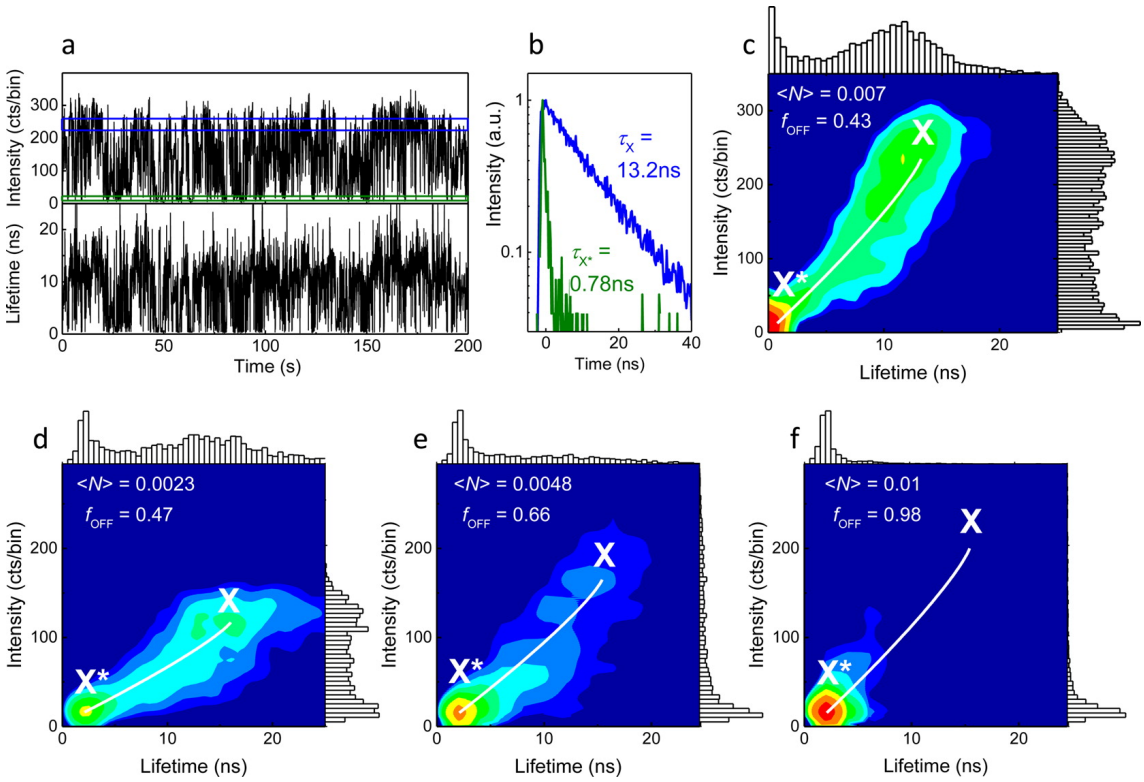

Figure 2.5 – a) Intensity trace of a single perovskite nanocrystal excited with a pulsed laser b) Lifetime histogram of the neutral (blue) and charged (green) states realised using photons in bins between, respectively, the blue and green lines of panel a. c-f) FLID images obtained at different excitation powers, showing the increasing prevalence of the charged ("off") state increasing the mean number of excitons created in each pulse of the laser $\langle N \rangle$. *(credits: Park* et al. *[4]).*

spectrum of the emitted light that, during the measurement, is blue-shifted: the easiest interpretation that we can do, is that the crystals progressively become smaller and the confinement increases, decreasing consequently the emission wavelength.

This can be seen in Figure 2.6: the central emission wavelength of the emitter decreases by 30 nm after around one minute of light illumination. It is possible to see that while the central emission wavelength decreases, the emission intensity decreases as well. At the end, the emitter becomes completely dark, as chemical reactions have irreparably modified its structure: this phenomenon of permanent loss of the emission is commonly called bleaching. An interesting study on this aspect has been performed by Rainò *et al.* [6]. The idea is thus to reduce the bleaching by encapsulating the emitters in a polymer matrix, to protect them from the combined action of moisture and light. To this end Rainò *et al.* tried different polymers. The result of their study is shown in figure 2.7. They selected and test five different polymers, among the mostly used poly-

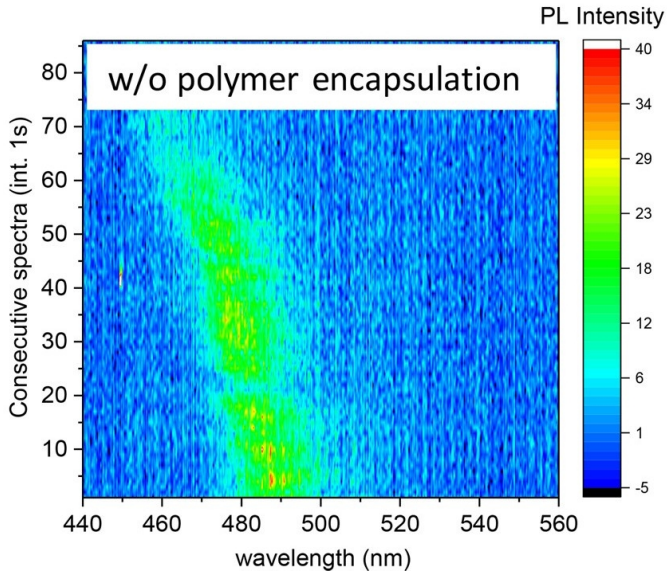

Figure 2.6 – Degradation of the emission spectra of a single perovskite nanocrystal. The green trace shows the evolution of the emitted signal during time. We observe a blueshift due to the degradation of the crystal. *(credits: Rainò* et al. *[6]).*

mers:

PMMA poly(methyl methacrylate), also known as acrylic, acrylic glass, or plexiglass, is a polymer with a refraction-index similar to the glass one;

TOPAS a commercial cyclic olefin copolymer;

SEBS styrene-ethylene-butylene-styrene block copolymer;

PS polystyrene, an aromatic polymer that is one of the most used plastics.

PMMA polymer is know for its good performance in replacing glass and it is commonly used as matrix for nanocrystals. Despite this, polystyrene provided better performances for this application. This is due, according to the authors, to the different binding it forms with the ligands that are at the surface of the perovskite itself.

2.2 Experimental setup for nanocrystal characterisation

To characterize our nanocrystals we prepare the samples via spin-coating deposition over a glass plate and we use an inverted microscope to perform the optical analysis.

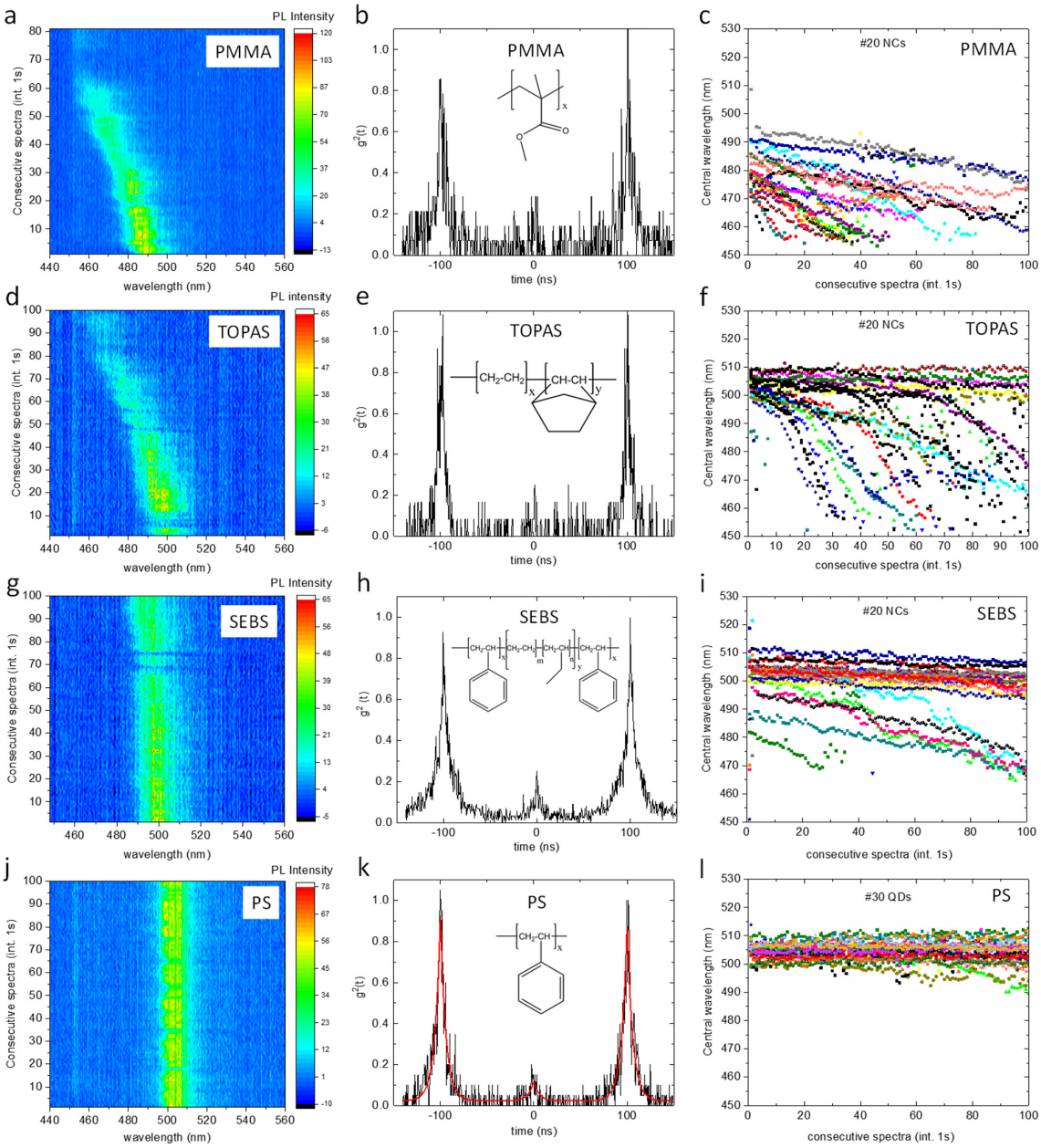

Figure 2.7 – Resistance of single photon perovskite nanocrystals protected by different polymers (Poly(methyl methacrylate) (PMMA), TOPAS, styrene-ethylene-butylene-styrene block copolymer (SEBS), Polystyrene (PS)). It is possible to see that the latter shows the best performance in protecting the emitter, as the emission drift is almost completely removed. *(credits: Rainò* et al. *[6]).*

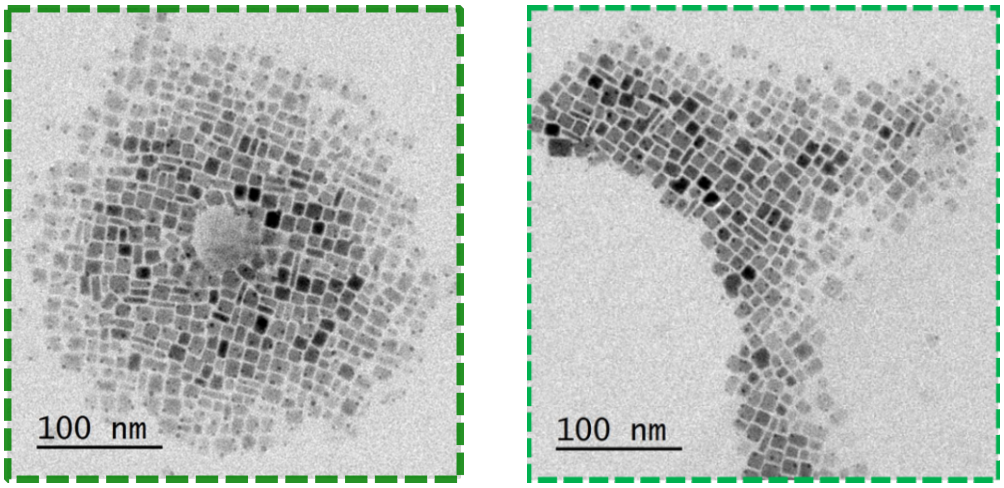

(a) (b)

Figure 2.8 – Scanning electron microscope images of for (a) Sample A and (b) Sample B. The nanocrystals present two sides of 10 nm while the other is shorter (between 2 nm and 6 nm). This difference is visible as some nanocristal appear leaning on the lateral side.

In this section I will discuss the experimental procedure and describe the scheme of the setup.

2.2.1 Perovskite fabrication

All the perovskite nanocrystals I studied were fabricated by Emmanuel Lhuillier at the "Nanoscience Institut of Paris" (INSP). I have studied perovskite nanocubes fabricated by two different ways which both required only few hours. This is one of the main advantages that perovskites share with other colloidal nanocrystals, with respect to other kind of single photons emitters, such as SiV defects in nanodiamonds, whose fabrication is longer and more complex.

Sample A

The sample was prepared using the procedure provided by Protesescu *et al.* [69]. This procedure leads to bright $CsPbBr_3$ nanocubes. Unfortunately the final solution is very concentrated and it is impossible to look for a single emitter without diluting it. The dilution procedure, even when performed with toluene (i.e. an appropriate solvent for perovskite nanocrystals), affects the stability of the emitters. A SEM image of the nanocrystals prepared with this method is shown in figure 2.8a. It is possible to see that they are

parallelepipeds, with two sides of the crystal of about 10 nm while the other one has a size of few nanometers.

Sample B

This procedure was initially intended to fabricate a slightly different kind of nanoemitters, the $CsPbBr_3$ nanosheets and was initially described by Weidman *et al.* [70]. Compared to the procedure used to prepare the sample A, there are three important changes:

1. a smaller amount of cesium oleate is introduced in order to favour the growth of the free phase of cesium;

2. two additional ligands are introduced during the process, to allow the crystallization of the cesium free phase;

3. the reaction is carried on for a longer time (from 10 s to 35 min).

With this method we obtained three different products.

$CsPbBr_3$ Nanoplatelets are the main product of the synthesis, or at least the product for which this synthesis was intended for; the obtained nanoplatelets can be written with the form $L_2[CsPbBr_3]_{n-1}PbBr_4$, where L represent the ligand.

Cs-free nanoplatelets consist in two-dimensional nanoplatelets where a plane of lead-bromide is sandwiched between two planes of ligands with C 8 chains.

$CsPbBr_3$ nanocubes are like the ones described for the sample A. These cubes are the ones we are actually interested in: I will show how they show a better stability compared to the cubes of the sample A, stability most likely due to the different ligands present in the solution.

In order to remove the first two products, we added a centrifugation step at the end of the procedure. This procedure removes the bigger compounds leaving only the third product in the solution. This provides us with a solution sufficiently diluted to be directly spin-coated and still allows us to find single photon emitters without any additional dilution as I will describe below. However, it was still too concentrated to be deposited directly on a nanofiber as I will show at a later stage. A SEM image of the nanocrystals prepared with this method is shown in figure 2.8b. As for sample A, they have a parallelepiped shape.

2.2.2 Sample preparation

Once fabricated, a new sample can be deposited on a glass coverslip to be observed with a microscope. First of all, we proceed with a suitable dilution, in order to reduce the concentration of the nanoemitters and to be able to resolve single emitters. Then we deposit it using a spin-coater that allows to spread almost homogeneously a thin film of the solution over the coverslip. This method avoids the unpleasant effects that happen when the droplet is inhomogeneously dried. Indeed the mechanism of droplet drying has been largely studied. An interesting review was done by Tarafdar *et al.* [71]. What is important to notice in our application is that during the drying process, the substances in suspension are often deposited at the edges and tend to form agglomerates that we want to avoid. The spin-coater rotates the sample at high velocity (usually 1500 rounds/min, distributing the solution over it and, at the same time, drying the sample.

Let us note that a different technique, often used in absence of a spin-coater, consists in using a solution of hexane-octane in the proportion of 9:1 as a solvent. This is known to naturally form a thin film over a glass plate simply by adhesion forces, without the need of spin-coating. However, to have the same concentration on the glass, the solution needs to be diluted more, with effects on the sample stability (as I will show later). For that reason, we decided to keep the same solvent used during the fabrication (toluene) and preferred the spin-coating method.

Once prepared, the samples need to be stored at room temperature, protected from light and moisture. With some exceptions, they does not last longer than a working week.

2.2.3 Experimental Setup

The experimental setup used to study the perovskite nanocrystal is shown in figure 2.9. To facilitate the understanding of the measurement principles, I will give a quick overview of the setup, discussing the details later on.

First of all, we spread the emitters over a glass coverslip using the spin-coater and we place it under the microscope. In order to address a single emitter, we need to find it and place it under the laser spot. Several methods are available to achieve this. A method that is often used, for example, is to create an image measuring the luminescence spot-by-spot scanning the sample under the laser light: this method has the inconvenience to be quite complicated to realize and slow to perform. Another method which is the one we chose, is to focus an intense light beam (such as the one coming from an LED) into

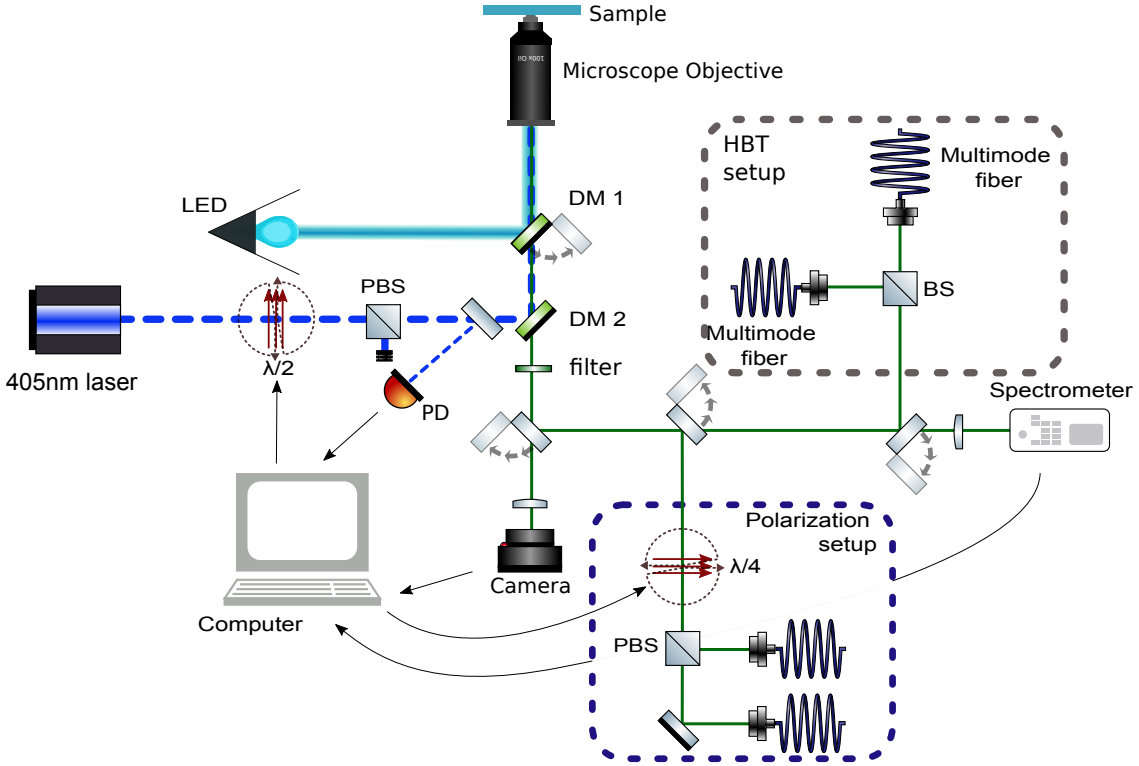

Figure 2.9 – Experimental setup for single nanocrystal analysis. For a wide-field view, a LED light is reflected by a 432 nm long pass dichroic beamsplitter and sent to the sample, via the microscope objective. For the excitation of a single nanocrystal, a pulsed laser light is reflected towards the microscope objective with a 432 nm filter, while the dichroic beamsplitter used for the LED is removed. The collected light is filtered to remove any trace of the excitation and then sent optionally to the camera, to the spectrometer or to the HBT setup. DM: dichroic mirror, BS: non polarizing beamsplitter, PBS: polarizing beamsplitter, PD: photodiode,$\lambda/2$: rotating half-wave plate, $\lambda/4$: rotating quarter-wave plate

the microscope, illuminating in this way the whole field of view. That way, we obtain a full image of the sample. This image, after filtering the excitation wavelength, allows us to visualize the emitters as bright spots on a dark background. A typical image obtained with this method is reported in figure 2.10.

This technique allows to directly "see" the image of the sample in a fraction of second, with all the advantages it has.

It is worth underlining that this method can be used as the intensity at which we need to excite each emitter to obtain a detectable emission is quite low. Indeed, as opposed to the "scanning" method where only a single spot is illuminated (area of the order of $1\,\mu m^2$), the light of the LED is shined over a much larger area (on the order of $0.1\,mm^2$, four order of magnitude bigger) and then the applicability of this method can be limited

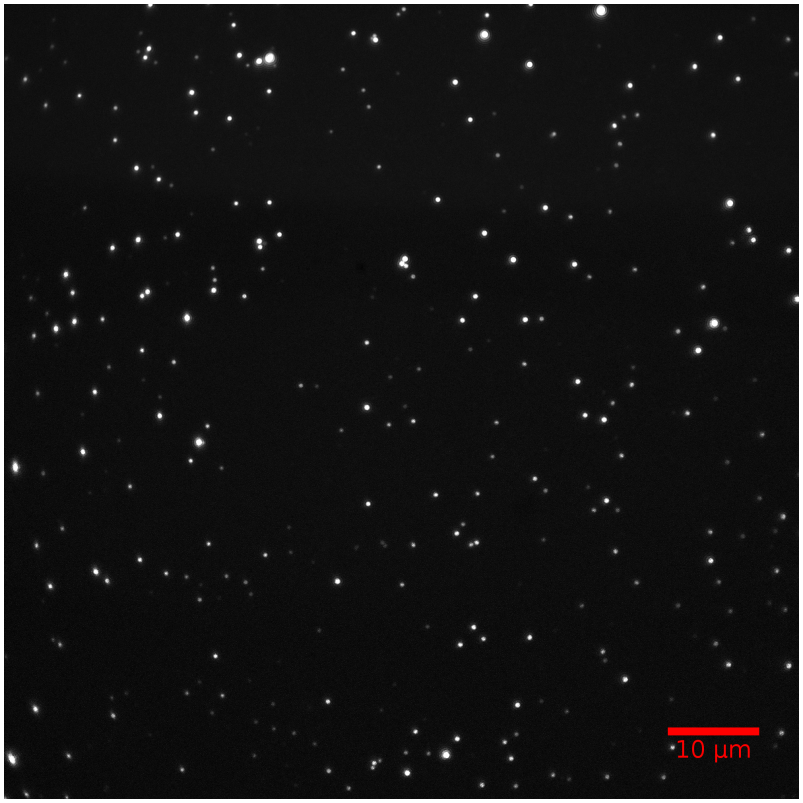

Figure 2.10 – Example of an image obtained with the CCD camera when the sample is illuminated by the LED. The bright spots are the nanoemitters, while the background is dark because the excitation light is filtered out.

by the difficulty to reach suitable intensities.

Once the image is performed and the emitter position identified, we move the sample via a precise translation stage to place the emitter under the laser illumination. The laser is aligned so that it focuses at the center of the image, so we know accurately its position. Except for the case of stability measurement that I will present later and where the whole image is recorded, at this point we switch from the LED to the laser illumination. For that, the first dichroic mirror (DM1) is removed and the laser is sent through the objective. The collected light cleaned from the excitation (or in other words the emitted light), can be analyzed with different instruments.

CMOS Camera: used to measure the emitted intensity, thanks to its linear response with the incident light;

spectrometer: to perform the spectrum of the emitted light, useful to know the wavelength of the emission and the spectral width;

HBT setup: used to perform the $g^{(2)}(0)$ measurement. Thanks to the time-tagged time

resolved technique, this setup allows us to know the arrival time of each photon allowing, at the same time, to measure the fluorescence lifetime of the emission, the fluorescence trace and to perform interesting blinking analysis;

polarization setup: used to perform polarization measurement. Two single photon detectors are used to correct the signal from the blinking effect, as shown below.

After the description of the main elements of the setup, it is important to detail the characteristics of some of the instruments used.

LED: Pizmatich 400nm LED, controlled with a digital interface that allows to tune the emitter power, it is collimated inside the objective to illuminate the full field of view.

405 nm LASER: Picoquant PDL800 (model LDH 405B) pulsed laser with pulse width smaller than50 ps, repetition rate from 2.5 MHz to 40 MHz.

rotating waveplate: controlled via a servomotor and combined with the following polarizing beam-splitter permits to control the excitation power sent by the laser inside the microscope with the computer.

photodiode: home made, receives a small fraction of the intensity, and through an initial calibration, permits to know the excitation power.

dichroic mirrors: both DM1 and DM2, are longpass dichroic mirrors with a cutoff wavelength of 432 nm. They reflect the excitation light inside the objective and transmit the emitted light to the detection part of the setup.

microscope objective: an oil microscope objective with a numerical aperture of 1.4 and a magnification of 100 $\times$. In this case the sample with the emitters lies on the opposite side with respect to the microscope. We used the oil objective for all the measurements, except to perform polarization measurements, indeed in this case an objective with a so large numerical aperture does not allow to measure the polarization correctly. Indeed, when collecting the emission with an high numerical aperture objective, we collect the emission into different directions, each of them having a different polarization: this results in a sum of different polarizations in the collected beam and thus in a lower degree of polarization measured. This point has been studied in detail by Lethiec *et al.* [72]. To reduce this problem, we used a dry objective with the same magnification and numerical aperture of 0.95. This is,

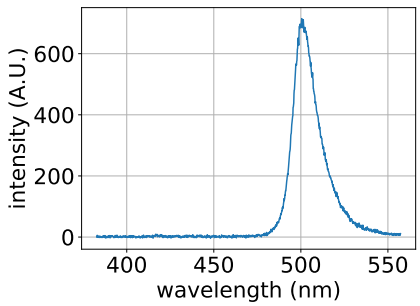

Figure 2.11 – Emission spectrum of a single perovskite nanocrystal. In this example we can see that the peak is at 501 nm and have a FWHM of 15 nm.

in our experiment, a good compromise between the need to use a lower numerical aperture objective and the need of collect enough signal.

filter: high quality long pass filter with a cutoff wavelength at 420 nm, to remove the residual excitation light.

CCD camera: Hamamatsu Orca, with a quantum efficiency between 70 % to 80 % at our detection wavelengths and squared pixels of 6.5 µm size.

spectrometer: Princeton Instruments Spectrum Analyzer, allows to record the spectrum of the light emitted by the perovskite nanocrystals.

mirrors: All the mirrors in the exciting path are dielectric mirror, while in the detection, when needed for polarization measurement, we have used silver mirrors to avoid changes in polarization.

2.3 Measurements

2.3.1 Perovskite Spectra

From the emission spectra, we can extract different information on the nanoemitters such as the central emission wavelength and the width of their emission. At room temperature, the fine structure of the emission with the different energy levels cannot be resolved in the spectrum. It is still very useful to have a quick characterization of the emitter we are measuring. An example of a single perovskite emission spectrum is shown in figure 2.11. Another interesting information can be obtained studying the distribution of the spectra of the two different samples. This analysis is reported in figure 2.12a.

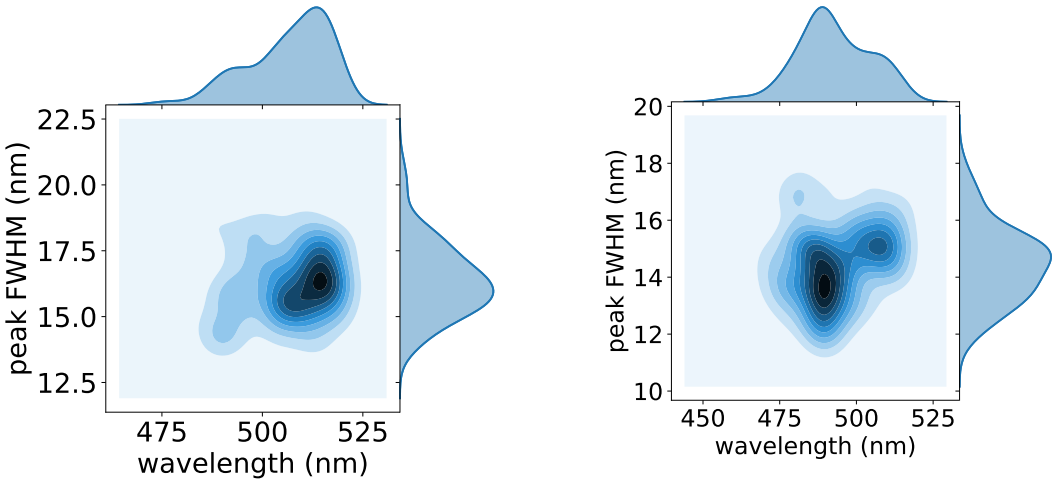

(a) (b)

Figure 2.12 – Distribution of central wavelength emission and the peak Full Width Half Maximum (FWHM) for the samples A (a) (calculated on 135 emitters) and B (b) (calculated on 74 emitters).

We can observe that sample A has both a broad FWHM and a higher central emission wavelength compared to sample B. These data can be correlated to the quantum confinement: we can thus expect a stronger confinement in sample B due to its lower wavelength of emission.

2.3.2 Saturation behaviour

The measurement of the saturation intensity also provides valuable information about the sample and each emitter. Such kind of measurement is usually performed by exciting the sample with different excitation powers and collecting its emission. This allows us to correlate the emitted power with the exciting one and plot a saturation curve. However, in presence of blinking or flickering, the measurement needs to be slightly adapted to minimize the influence of the emission fluctuations on the saturation curve.

Our emitters have two drawbacks that we need to consider to correctly interpret the results of the performed measurements: first of all, they bleach and this implies that we should excite them for the shortest possible time and with the lowest possible intensity. Secondly, they blink which affects the measurement of the emitted power by inducing strong fluctuations of the signal. To overcome these issues, we chose to automatize the acquisition process which allows us to perform the measurement quickly and collect more data points to reduce the effect of the blinking on the measurement. Via a *Python*

script, a computer controls the multiple instruments for the measurement, namely: a shutter, to block the excitation laser when not needed; a rotation wave-plate to tune the laser power, a photodiode and a camera to measure both input and output intensities. The photodiode (represented with *PD* in figure 2.9) returns an electrical tension proportional to the light power impinging on it, that is also proportional to the light power shined on the emitter. Before the measurement, we calibrate it in order to be able to convert the measured voltage in the power effectively shined on the emitter. The measurement steps are the following:

- First, the maximum power obtained from the laser, as well as the minimum one and the corresponding rotation position of the wave-plate are measured with a power-meter and recorded by the control program.

- The emitter is placed under the laser spot, we double check its position, firstly verifying with the LED that the emitter is in the position where the laser is, and then shining the laser to verify it really excites the selected emitter. We also verify that no-other emitter is excited by the laser.

- The region where the emitter appears in the camera is set in the code, permitting to exclude all the pixels that are not concerned and thus to increase the signal/noise ratio.

- When the measurement starts, with the shutter off, the wave-plate goes in the position of minimum intensity. At each cycle, the wave-plates moves by some degrees (depending on the settings) up to reach the maximum. At each step multiple operations are performed.

  - With the shutter closed, the camera is read to measure the background.
  - The excitation power measured by the photodiode is recorded
  - The shutter is opened and the emitted intensity on the camera is measured several times, keeping only the highest measured value to reduce the effect of the blinking. This allows to select the measure in which the state has been "on" for most of the time, minimizing the probability that the emitter is in the "off" state for a significant time duration.

- At the end of the measure, we plot the emission power as a function of the excitation intensity, in order to obtain the saturation curve.

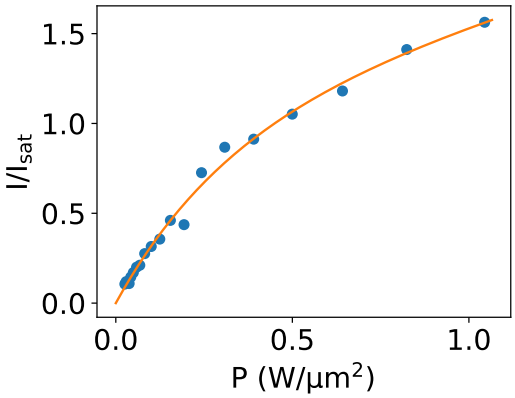

Figure 2.13 – Example of saturation measurement

An example of one of the measurements is presented in figure 2.13: the experimental points are represented by the blue dots. The orange curve is the fit with the usual saturation function

$$P = A \cdot \left[1 - e^{-\frac{I}{I_{sat}}}\right] + B \cdot I \tag{2.2}$$

Here, as seen in section 1.5.2, the first term of the sum represents the saturating part that is due to the single exciton component, while the second term is due to the bi-exciton emission. This curve can be used to compare more easily the characteristics of different emitters. Indeed exciting the sample with the same intensity ratio with respect to the saturation power leads to the same number of excitons created, and thus a similar excitation. To do this, anyway, the emitters need to be photo-stable enough; in the case of sample A, less stable than the sample B, it was not possible to perform a preliminary measurement of the saturation intensity, as the emitters were bleaching too fast.

2.3.3 Polarization measurements

A polarized emission for a single photon emitter is an important characteristic such as dot in rod nanocrystals [53]. To characterize the polarization of a given emission we can measure the Stokes parameters. The setup is shown in figure 2.9 and allows to measure all the Stokes parameters from the light transmitted after a polarizing beam splitter as a function of the position of a quarter-wave plate in front of it.

Let us consider only one transmitted beam in the polarization setup (represented in 2.14) and imagine for the moment the reflected beam to be absorbed by a beam-stopper. We can see the beam splitter as a fixed polarizer: when rotating the half waveplate,

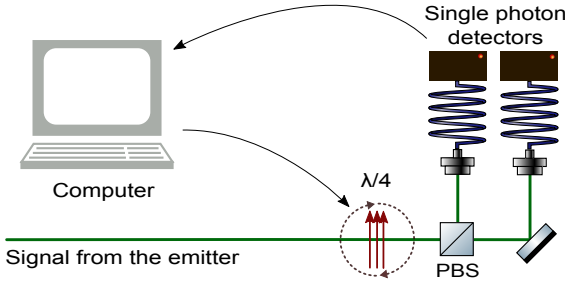

Figure 2.14 – Detail of figure 2.9 representing the experimental setup used to measure the polarization. The quarter-wave plate ($\lambda/4$) and the acquisition of are controlled by the computer.

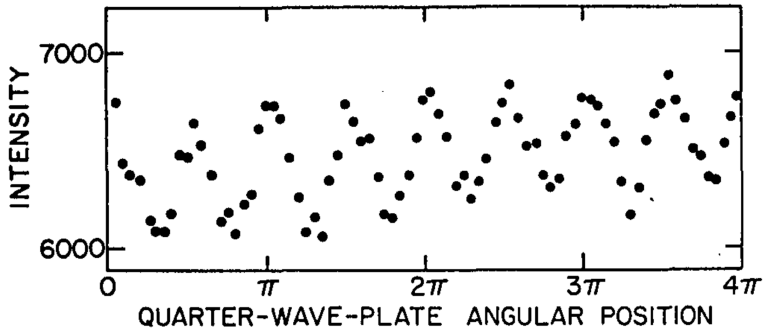

Figure 2.15 – Measurement of the emission Stokes parameters in case of a linearly polarized light. The intensity collected is reported as a function of the rotation of the quarter-wave plate. *(credits: Berry, Gabrielse, and Livingston [73]).*

we rotate the polarization of the incoming light, obtaining a variation on the number of counts detected by the single photon detector. Studying the obtained curve which represents the intensity collected by the photodiode as a function of the angle of the polarizer, it is possible to reconstruct the Stokes parameters of the light. This method is clearly reported by Berry, Gabrielse, and Livingston [73]. The result of one of these measurements is reported in figure 2.15. The curve is described by the equation (2.3):

$$\begin{aligned} I_T(\alpha,\beta,\delta) = \frac{1}{2}\left[S_0 + \left(\frac{S_1}{2}\cos 2\alpha + \frac{S_2}{2}\sin 2\alpha\right)(1+\cos\delta)\right] + \\ + \frac{1}{2}[S_3 \sin\delta \cdot \sin(2\alpha - 2\beta)] + \\ + \frac{1}{4}[(S_1 \cos 2\alpha - S_2 \sin 2\alpha)\cos 4\beta + \\ + (S_1 \sin 2\alpha + S_2 \cos 2\alpha)\sin 4\beta](1-\cos\delta). \end{aligned} \tag{2.3}$$

where S_0, S_1, S_2 and S_3 are the four Stokes parameters of the light as described in section 1.5.5, α is the rotation angle of the polarizer (in our case the polarizing beam splitter) and β is the rotation angle of the fast axis of the wave-plate, while δ is the delay introduced by the wave-plate, in our case the quarter wave-plate.

If we choose to rotate the polarizer, meaning varying the value of α, we need to pay attention to the fact that all the detection optics need to be polarization insensitive. For this reason, it is more convenient to keep the polarization fixed and to rotate the wave-plate. A deeper inspection on (2.3) allows to notice the following behavior: let us imagine a change in β at a frequency ω; the first term does not depend on β, while the second oscillates with a frequency 2ω and the third oscillates at a frequency 4ω. Therefore we can interpret this equation as a Fourier series.

Generally, if a real-valued function $f(x)$ is integrable in an interval P, its Fourier series is given by:

$$f_N(x) = \frac{c_0}{2} + \sum_{n=1}^{N} \left(c_n \cos\left(\frac{2\pi n x}{P}\right) + s_n \sin\left(\frac{2\pi n x}{P}\right)\right). \tag{2.4}$$

In equation (2.4), P is the interval and the period of f_N while c_n and s_n are defined as follow:

$$c_n = \frac{2}{P} \int_P f(x) \cdot \cos\left(2\pi x \frac{n}{P}\right) dx \tag{2.5}$$

$$s_n = \frac{2}{P} \int_P f(x) \cdot \sin\left(2\pi x \frac{n}{P}\right) dx \tag{2.6}$$

This is valid for a continuous function; as we measure N discrete points, the last two equations have to be rewritten as follows (δ, as before, is the delay introduced by the waveplate):

$$c_n = \frac{2}{N} \frac{1}{1+\delta_{n0}} \sum_{i=0}^{N-1} s_i \cdot \cos\left(2\pi x_i \frac{n}{P}\right), \tag{2.7}$$

$$s_n = \frac{2}{N} \frac{1}{1+\delta_{n0}} \sum_{i=0}^{N-1} s_i \cdot \sin\left(2\pi x_i \frac{n}{P}\right). \tag{2.8}$$

We can thus rewrite equation (2.3) as a function of β, with the substitution $\beta \longrightarrow \beta_0 + \beta$:

$$I_T(\beta) = c_0 + c_2 \cos 2\beta + c_4 \cos 4\beta + s_2 \sin 2\beta + s_4 \sin 4\beta \tag{2.9}$$

where β varies from 0 to 2π. This is a finite Fourier series and its non-zero coefficients c_0, c_2, c_4, s_2, s_4 can be computed using equations (2.7) and (2.8). Clearly, as in any experiment, the number of measured points cannot be infinite. In order to estimate the number of points necessary, from the Nyquist–Shannon sampling theorem [74], we know that to correctly sample a signal we need to sample it at least twice as much as its maximal frequency. In other words, we need to measure at least 8 points in our curve: if we choose to use an even number of samples $N = 2L$ and $L = 4$ we need to slightly modify the equations (2.7) and (2.8) in the following way [73]:

$$c_n = \frac{2}{N}\frac{1}{1+\delta_{n0}+\delta_{nL}}\sum_{i=0}^{N-1} s_i \cdot \cos\left(2\pi x_i \frac{n}{P}\right) \tag{2.10}$$

$$s_n = \frac{2}{N}\frac{1}{1+\delta_{n0}+\delta_{nL}}\sum_{i=0}^{N-1} s_i \cdot \sin\left(2\pi x_i \frac{n}{P}\right) \tag{2.11}$$

It can be experimentally more convenient to vary β from 0 to π as the signal is periodic with a period of π. In this case, we can make the formal substitution $\beta' = 2\beta$ in the equation (2.9) and obtain:

$$I_T(\beta) = c_0 + c_1' \cos\beta' + c_2' \cos 2\beta' + s_1' \sin\beta' + s_2' \sin 2\beta' \tag{2.12}$$

where, we have

$$c_1' = c_2, \qquad c_2' = c_4, \qquad s_1' = s_2, \qquad s_2' = s_4.$$

Once again, the equation (2.12) is a Fourier series (with respect to the angle β'), and we can thus calculate its Fourier coefficients. We can notice that in this case, using the fact that the measurement is periodic, we divided by two the maximal frequency. Thus, once again, the minimum number of points necessary to obtain the non-zero coefficients of the equation (2.12) is given by the Nyquist–Shannon sampling theorem: four points are sufficient. If four is the minimum number to correctly reconstruct the signal, experimentally it is always better to collect a bigger number of points.

Now we can compare equations (2.9) and (2.12), in order to obtain the Stokes coeffi-

cients [73]:

$$S_0 = c_0 - \frac{1+\cos\delta}{1-\cos\delta}\cdot[c_4\cos(4\alpha+4\beta_0)+s_4\sin(4\alpha+4\beta_0)] \tag{2.13a}$$

$$S_1 = \frac{2}{1-\cos\delta}[c_4\cos(2\alpha+4\beta_0)+s_4\sin(2\alpha+4\beta_0)] \tag{2.13b}$$

$$S_2 = \frac{2}{1-\cos\delta}[s_4\cos(2\alpha+4\beta_0)-c_4\sin(2\alpha+4\beta_0)] \tag{2.13c}$$

$$S_3 = \frac{c_2}{\sin\delta\sin(2\alpha+4\beta_0)} = \frac{-s_2}{\sin\delta\cos(2\alpha+4\beta_0)} \tag{2.13d}$$

$$|S_3| = \frac{\left(c_2^2+s_2^2\right)^{\frac{1}{2}}}{\sin^2\delta} \tag{2.13e}$$

We can choose the reference system in which $\alpha = 0$, β_0 and δ can be obtained by calibrating the system as explained by Berry, Gabrielse, and Livingston [73]. S_0 represents the intensity and we can renormalize the other Stokes parameters to it.

In our analysis we did not take into account the effect of the blinking: it has been shown [75] that the intensity fluctuations have a significant effect on the measurement. For this reason it is important to implement a normalization scheme: this is implemented by adding a second detection channel. This way, all the emitted light, transmitted and reflected, is collected. The signal transmitted by the beamsplitter is thus normalized by the entire signal collected, reducing the possible influence of the blinking.

An example of these measurements is shown in figure 2.16. The red dots are the experimental points while the red curve is obtained via the described Fourier analysis. Unfortunately, the light emitted by our emitters happened to be non-polarized. We repeated the measurement for several different emitters, with the same conclusion.

This behavior was expected due to the cubic symmetrical structure and shape which do not favor any preferential polarization. However, this finding does not exclude that future studies of asymmetrical perovskites could give polarized photons.

2.3.4 $g^{(2)}$ measurements

I've shown in the Introduction how important it is, from the quantum optics point of view, to perform $g^{(2)}$measurements. I detail here how the measurement is performed and how the data are treated to obtain the $g^{(2)}$autocorrelation function.

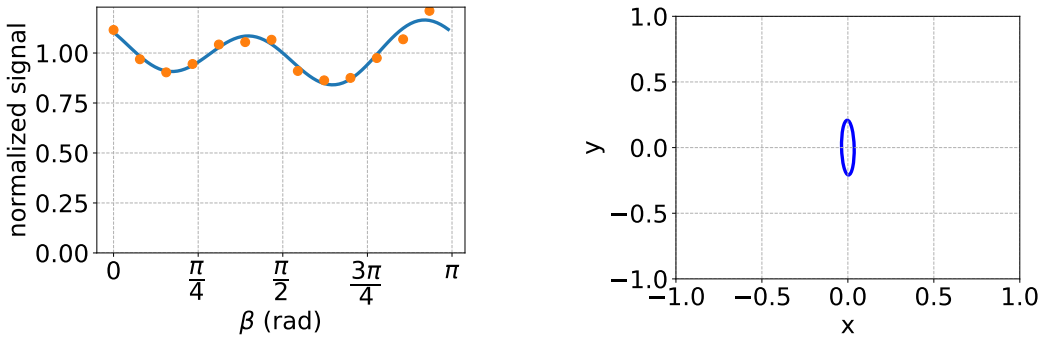

(a) (b)

Figure 2.16 – (a) Example of measure of Stokes parameters on a perovskite nanocrystal. The red dots are the experimental points while the blue curve is obtained via the described procedure. (b) Polarization ellipse. The degree of polarization is 0.18 and the degree of linear polarization is 0.17, showing an almost non polarized emission.

Acquisition

To perform an autocorrelation measurement, also known as $g^{(2)}$, we use the setup evidenced by a gray dashed line in figure 2.9. The signal is split in two parts and sent to two different avalanche photodiode single photon detectors (Excelitas SPCM-AQRH-14-FC) via two multimode fibers. To record the signal, a Picoquant PicoHarp 300 TCSPC card is used, together with a Picoquant PHR 800 router. In practice the "sync" channel of the laser, after an appropriate voltage conversion (the laser and the card use a different standard, thus the signal needs to be attenuated and inverted as explained in the manual), is sent to one channel of the PicoHarp card (usually channel 0) while the other channel receives the signal from the router. The router collects the signal from the two single photon detectors and is sent it to the card, recording in which channel the photon has arrived. The scheme of this mechanism is shown in figure 2.18. If we use this system with the Time Tagged Time-Resolved mode, we can record a huge amount of information. For each detected photon, we record:

- the laser pulse that generated it, as an integer number that starts from 1 (first laser pulse sent in the measurement) and increases at each pulse (even when no photons are collected);
- the delay between the collected photon and the laser pulse;
- on which channel, and thus on which APD the photon was detected.

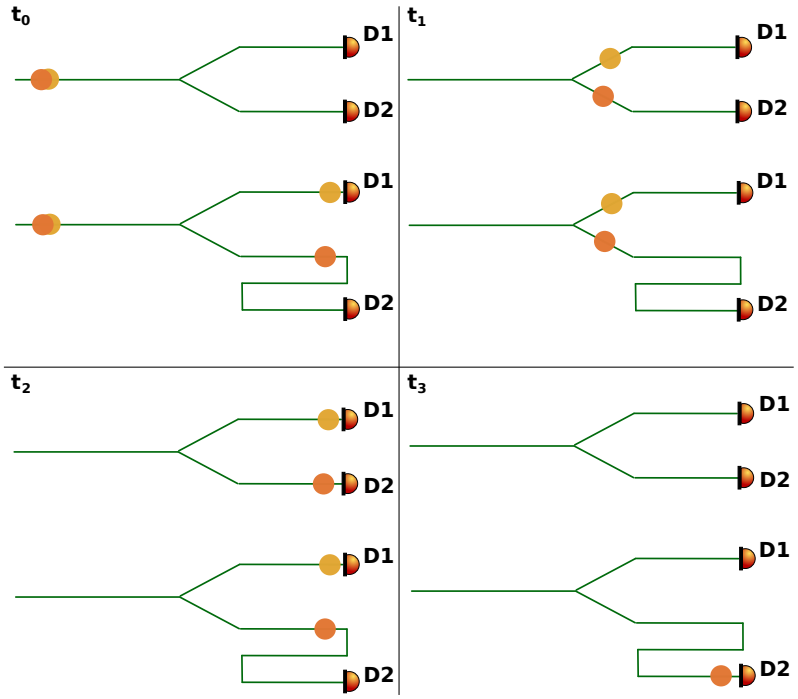

Figure 2.17 – Example of the delay line effect on photon detection. In each panel, the situation without (upper path) and with (lower part) the delay line is represented. t_0) Two photons are emitted simultaneously and t_1) separated on different paths by the beamsplitter. t_2) in case of no delay line, the two photons arrive at the two detectors and only one is recorded. In the other case, only one photon arrives on the detector, while the other arrival is delayed. t_3) In case of the presence of the delay line, the second photon arrives on the detector: its true arrival time with respect to the first one can be obtained by subtracting $\delta = t_3 - t_2$.

A disadvantage of this measurement technique is that the signal of both APDs is redirected from the router on the same channel on the card (channel 1 in figure 2.18). The channel 1 of the card that records all the photons arrived is the same for both APDs. After each photon detected, there is a dead time t_{dead} for the channel during which it is not able to collect any other signal. As we want to measure $g^{(2)}(0)$ this behaviour can be a huge problem, as the dead time prevents to measure delays t_δ shorter than t_{dead}. We can write this limitation in a more formal way by saying that we cannot measure τ if the following condition is satisfied:

$$|\tau| \leq t_\delta \tag{2.14}$$

This can be resolved with a workaround, we can delay the arrival of the photons of one of the two channels using a delay line: if we call this delay T_D we can rewrite the

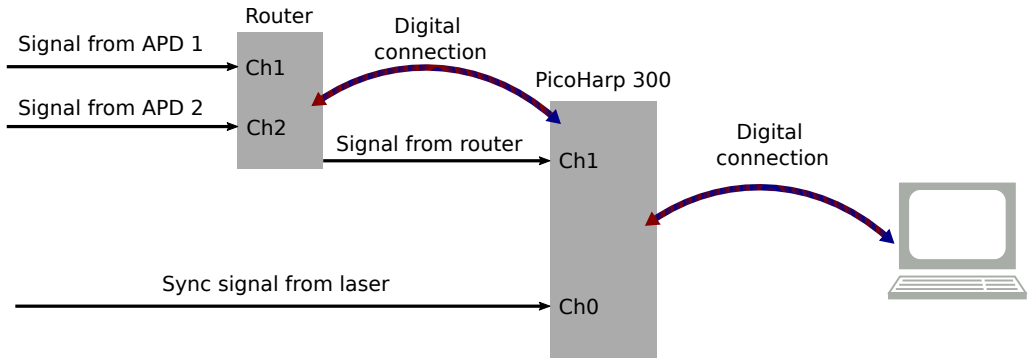

Figure 2.18 – Scheme of the detection apparatus: the router transmits the detected signal to the PicoHarp card, passing the information on which channel the signal arrived from. The PicoHarp card measures the arrival time of the sync signal from the laser, given by the channel 0.The detection signal from the router is received in channel 1. After the stop signal is received, the card has a dead time on the order of hundreds of nanoseconds before being able to detect another signal on the same channel.

condition (2.14) as

$$T_D - t_\delta \leq \tau \leq T_D + t_\delta \tag{2.15}$$

With a T_D long enough, the interval fixed by equation (2.15) does not contain $\tau = 0$.

To clarify the effect of the delay line in single photon detection it is useful to refer to the image 2.17. An ideal experiment is presented with and without the addition of a delay line and is shown at different times. Let us imagine two photons emitted almost simultaneously at the time t_0. They have the same trajectory until (time t_1) when they encounter the beamsplitter. They then get separated in two different paths. Clearly, the photons can also continue on the same path, but we will consider the case in which they propagate to different paths. In the case where no delay line is present, both signals will arrive almost at the same time t_2 onto different detectors, with the result that the card will be able to record only one of them. In the case where a delay line is present, the orange photon will arrive later, at time t_3; calling δ the fixed time delay introduced by the delay line. We have $t_3 = t_2 + \delta$ and it is sufficient to subtract δ from the time measured by the second detector to reconstruct the original signal.

Signal cleaning

An example of the signal acquired is shown in figure 2.19a. The inset clearly shows the dead time (as explained) while the real zero delay of the $g^{(2)}$ is moved to about 300 ns from the origin of the time axis. On the y-axis is reported the number of photon coincidences. This gives some useful information but it needs to be 'clean' in order to obtain the final

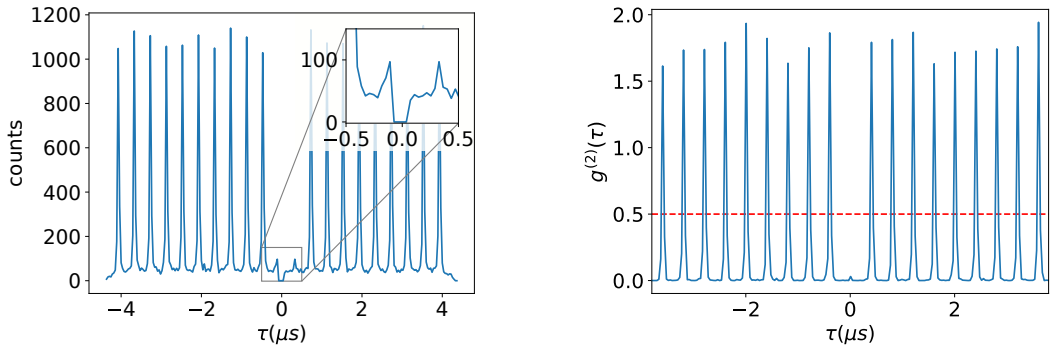

(a) (b)

Figure 2.19 – (a) $g^{(2)}(\tau)$ measurement without any treatment, in the inset is clearly visible the dead time of the instrument (b) $g^{(2)}(\tau)$ elaborated and cleaned. The emitters shows a $g^{(2)}(0) \approx 0$, thus a very good single photon emission.

signal.

To do this we need to:

1. move the zero of the time axis in order to remove the effect of the delay line,
2. normalize the data to have the $g^{(2)}$ function instead of the number of coincidences,
3. remove the effects caused by the background of the measurement.
4. remove the confusing zeros due to the dead-time

If the first point is straightforward the other two are not. For point 2, an approach is to look at the $g^{(2)}$ measurement at long delays compared to the blinking time. There, the $g^{(2)}$ function should converge to 1, due to its normalization. In our case, using the pulsed laser, it means the height of the peaks should converge to 1. We can therefore compute the $g^{(2)}(\tau)$ for $\tau \approx 10\,\text{ms}$ to find the mean height of the peaks and normalize it to one.

Concerning point 3, we can make some considerations on how the coincidences are counted. We call $M(\tau)$ the number of counts measured at a given delay τ. Each count can be generated either by a start from the signal or from the background and by a stop from the signal or from the background. Calling $s(\tau)$ the probability to have a start (or stop) generated by the signal and $b(\tau)$ the probability to have the start (or stop) generated by the background, we can write (when both $b(\tau)$ and $c(\tau) \ll 1$):

$$M(\tau) = C\,(b(\tau) + s(\tau))\,(b(\tau) + s(\tau)) \tag{2.16}$$

where C is a constant of proportionality. We define $M' = \frac{M}{C}$. We consider τ_b in between two consecutive peaks, we know that there is no signal there and $s(\tau_b) = 0$.

$$M'(\tau_b) = b^2(\tau) \tag{2.17}$$

To find $M_c(\tau) = Cs^2(\tau)$ we solve the system of these two equations and we find that

$$M_c(\tau) = M(\tau) + M(\tau_b) - 2\sqrt{M(\tau)}\sqrt{M(\tau_b)} \tag{2.18}$$

With this formula, we obtain the $g^{(2)}(\tau)$ histogram cleaned from the background counts.

The last step allows us to remove the "dead-time". This is easily done by removing a number of points equivalent to one peak and we can see that it does not perturb the result.

The resulting signal is shown in figure 2.19b. We can notice that the peaks around $\tau = 0$ (except for the one at $\tau = 0$), reach a value higher than one. This is a well known effect of the blinking [47]. We can understand this behaviour by taking into account the fact that the probability to have an emission is higher when a photon has recently been detected. In this case, indeed, the state is known to be "on". On the opposite, at far delays from the first detected photon, the state could be both in "on" and "off" states. It is thus normal, fixing the normalization of the $g^{(2)}(\tau)$ at 1 for large values of τ, that the $g^{(2)}(\tau)$for small values of τ will reach values bigger than 1.

2.4 Stability

As already explained, one of the main problems with perovskite nanocrystals is their stability under light illumination. To address this problem we initially chose to follow the approach of Rainò *et al.* [6], and see if the positive effect of polystyrene was confirmed with our setup. To this end, we tried to add polystyrene to the Sample A before the deposition, mixing a solution of this polymer to the solution containing the nanocrystals (both of them where dissolved in toluene), to see if we were able to measure an increased stability.

2.4.1 Role of the polystyrene

To perform the measurement, we decided to compare the sample with polystyrene and a sample without polystyrene under the emission of the light of an LED at maximum

power. Using the camera, we recorded an image of the sample each 20 s and counted the number of distinct bright emitters in each image via a program written for this purpose. This way, we were able to obtain a statistics of the emitters' behavior by a single set of images, directly measuring their bleaching time. The result of this measurement is reported in figures 2.20. On the left picture (2.20a) the images of the samples with and

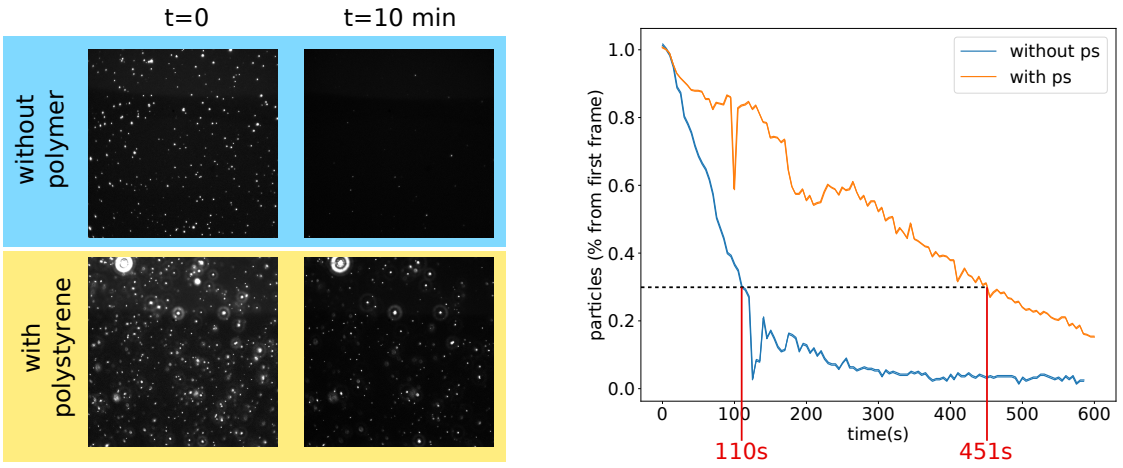

(a) (b)

Figure 2.20 – (a) Images of the samples at the beginning of the measurement ($t = 0$) and after 10 min ($t = 10$ min) under strong LED illumination, without and with polystyrene protection. (b) Quantitative analysis of the measurement: the stability is increased by a factor 4.

without polystyrene are shown at the initial time of the measurement and after 10 minutes of strong LED illumination. It is clearly visible that the stability is increased by the presence of the polystyrene. Indeed, after 10 minutes, most of the emitters are still bright. This effect can be quantified counting the number of emitters that are still bright in each frame. This is shown in figure 2.20b. If we measure the time at which the emission of the emitters is reduced by 30 % of the initial amount, we can see that this time is multiplied by four thanks to the polystyrene protection.

2.4.2 Role of the Sample preparation

Protecting the perovskite emitters with a polymer is not the best option suitable for photonic applications. For applications that need single nano-objects to be precisely positioned, the presence of the polymer, that takes space, can perturb the near field. For this reason we looked for alternative solutions and in particular we investigated different samples and different fabrication methods. Surprisingly, the fabrication of the sample B

that was intended to obtain two-dimensional platelets, produces also very stable perovskite nanocubes. To study the stability properties of these nanocubes, we performed a measurement similar to the one discussed in [6]. We illuminated a single photon emitter at the saturation power with a pulsed laser and measured the evolution of the spectrum as a function of time. This measure is shown in Figure 2.21. It is possible to see that

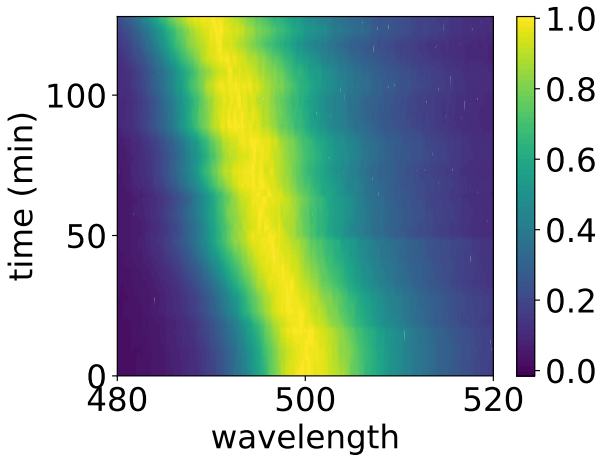

Figure 2.21 – Evolution of the fluorescence spectrum of a single perovskite nanocube of sample B as a function of time. The emitter was excited at the saturation intensity. In order to clear the image from the effect of the blinking, each spectrum (i.e. each row) is individually normalized. As a consequence, the image does not report the intensity evolution of the signal. A blue-shift of about 10 nm after two hours is visible.

there is a blue shift, as already observed in previous works[6] but with a very different timescale. In our case we were able to measure the emission up to 2 h with a shift of about 10 nm. We can compare our results with those shown in figure 2.6, where a degradation of more than 20 nm is observed in some tens of seconds. The blue shift can be attributed to the degradation of the external layers of the emitters, that become smaller and thus are more confined. It is interesting also to perform the same measurement shown in section 2.4.1 for this sample. We performed this measurement for different dilutions of the original solution, finding that the robustness of the emitters is strongly concentration-dependent. This is shown in figure 2.22 where the blue curve represents the number of emitters that are still alive as a function of time for a sample prepared by spin-coating directly from the original solution. The other curves represent the same measurement for samples prepared by diluting the initial solution with toluene at different ratios. It is clear that, while the concentrated sample is stable even after 20 min, any subsequent dilution reduces the sample stability with the result that only 30 % of

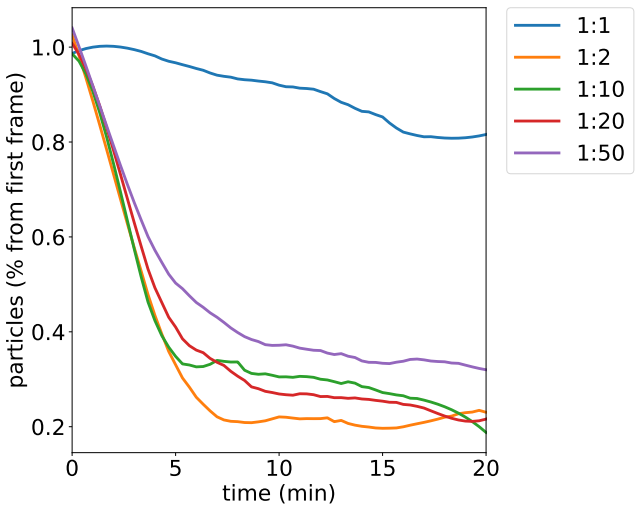

Figure 2.22 – Measure of the robustness of perovskites nanocrystals for samples with different concentrations. The samples were obtained by diluting the original solution in toluene.

the emitters are still alive after few minutes of strong excitation with the LED. This is probably due to the presence of ligands alongside the perovskites in the original dilution. When we increase the amount of solvent, we reduce the ratio ligands/solvent in the solution, affecting this way the stability.

The effect of dilution on the stability can be a limit for using these emitters for photonic applications as often very diluted samples are needed. With this study, we have shown that the preparation of the emitters plays a crucial role on their stability under light illumination and suggest a possible strategy to increase the emitters stability compensating the effect of the dilution. For example, we can add, along with toluene, the appropriate proportion of ligands needed to maintain the initial ratio ligands/solvent.

2.5 Blinking properties

It is interesting to characterize the blinking behavior of single quantum dots. Indeed, blinking is usually an undesired characteristic of nano-emitters and its characterization helps to find the possible path to reduce it. In addition, studying the blinking, we can access interesting information about the states contributing to the emission.

In other kind of colloidal quantum dots, such as CdS/CdSe rods, this behavior has been widely studied, as shown in the section 1.5.4. Previous studies have shown that perovskite nanocrystals present luminescence fluctuations, similar to those observed

for other kinds of analogous emitters. The first study of this behavior, described in section 2.1.2 was performed by Park *et al.* [4]. We decided to perform a similar study with our emitters in order to understand their behavior. In order to acquire a good statistics and to have a good signal to noise ratio, we need the emitters to stay in the bright state for a sufficient long time: for this reason I will limit this study to the sample B.

First of all, it is useful to observe the timetrace to have a rough idea of the kind of blinking we are dealing with. This is reported in figure 2.23 Specifically, from figure 2.23a

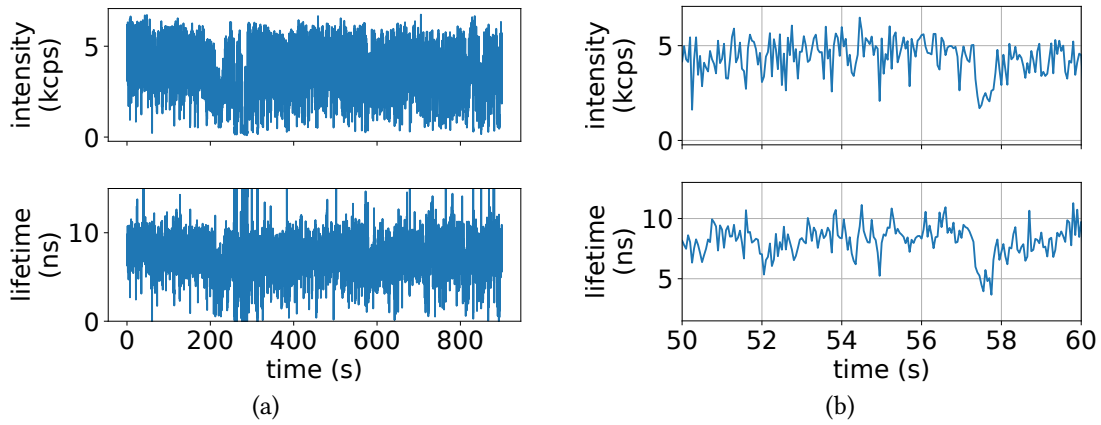

Figure 2.23 – Fluorescence trace acquired for a single photon emitter excited at half of the saturation intensity (top panels) correlated with the mean measured lifetime (bottom panels). (a) Full trace acquired. (b) Zoom on a part of the trace.

on the top panel, the full trace recorded for this emitter is shown. It is possible to see that there are fluctuations of the intensity, but it is not possible to identify regions completely "dark". This is confirmed by inspecting the zoomed curve reported in the top panel of figure 2.23b. This means that the characteristic blinking time is actually shorter than our binning time: in this case, it is better to talk about flickering [51].

On the lower panels of figure 2.23, the evolution of the lifetime as a function of time is reported. It is calculated by averaging the arrival time of the photons in each bin.

Comparing this evolution with the fluorescence trace shown in the top panels, we can identify a correlation between the emission state and the emission lifetime. This is clearer in figure 2.23b where, thanks to the zoom, we can clearly see that a reduction in the emission at $t = 57$ s reflects in a shorter lifetime. This is the signature of a type A blinking.

Concentrating our analysis on these emitters, we can observe the normalized lifetime histogram shown in figure2.24. The blue curve is the experimental points, while the

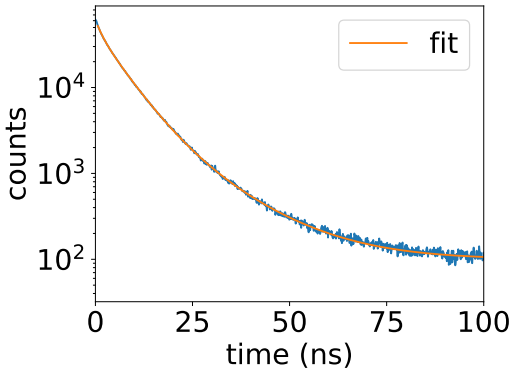

Figure 2.24 – Lifetime of a single perovskite nanocrystal, fitted with a triple exponential decay model. We obtain 1.4 ns, 6.1 ns and 14.7 ns, corresponding respectively to the lifetimes of the biexciton, grey and neutral emission states.

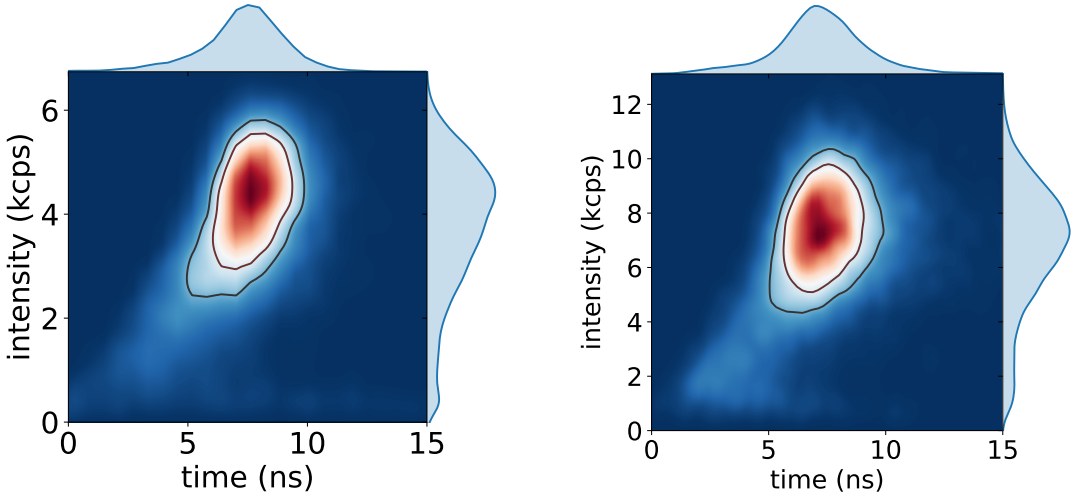

(a) (b)

Figure 2.25 – fluorescence lifetime intensity distributions (FLID) for a single perovskite nanocrystal excited at half ((a)) and twice ((b)) the saturation intensity. The enclosed black curves contain respectively 50 % and 68 % of the occurrences.

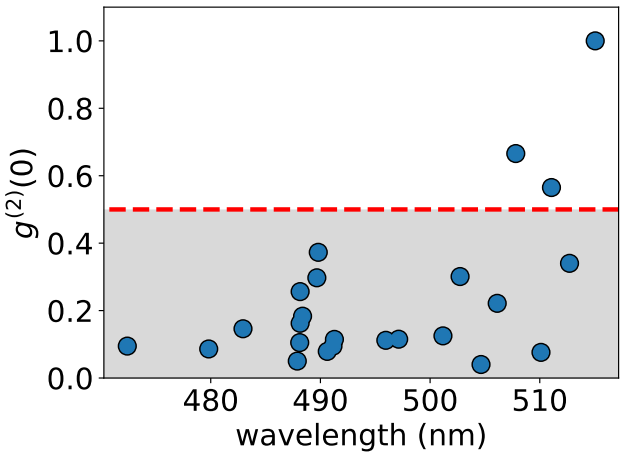

Figure 2.26 – $g^{(2)}(0)$ distribution as a function of the central emission wavelength for 33 different emitters excited at the saturation intensity.

orange curve is a fit using a triple exponential decay model:

$$A_1 \cdot e^{-\frac{t-t_0}{\tau_1}} + A_2 \cdot e^{-\frac{t-t_0}{\tau_2}} + A_3 \cdot e^{-\frac{t-t_0}{\tau_3}} + B \tag{2.19}$$

where the three different lifetimes τ_1, τ_2 and τ_3, corresponds to the neutral, the charged and the biexciton emission respectively [51] (see in section 1.5.3). A_1, A_2 and A_3 are the respective amplitudes while B represents the background counts.

We can now study the lifetime as a function of the emitted intensity with the fluorescence lifetime intensity distributions (FLID) that are represented in figure2.25. The same emitter has been excited with two different intensities, at half of the saturation intensity (figure 2.25a) and at twice the saturation intensity (figure 2.25b). In both cases, the area surrounded by the closed curves contains 50 % (inner curve) and 68 % of the occurrences. If we compare these distributions with the ones measured by Park *et al.* [4] shown in figure 2.5, we can see that, even at high excitation intensity, our emitters remain in a bright state. This property shows again the robustness of the emitters produced with this fabrication method. A good level of emission remains even under non-optimal strong excitation conditions as the ones presented here.

2.6 $g^{(2)}$ distribution

We have seen before how it is possible to measure the spectrum and the $g^{(2)}$ for single photon emitters, as well as the information we can extract from these measurements. It

is also interesting to combine this information and visualize the distribution of the $g^{(2)}$ as a function of the wavelength. We performed this for sample B and it is reported in figure 2.26. For each emitter, the $g^{(2)}(0)$ function is shown as a function of the central emission wavelength. The shaded region contains the emitters that can be considered emitting single photons. We can observe a degradation of the single photon emission when the central emission wavelength increases. In order to find an explanation to this phenomena it is interesting to study the size distributions of the cubes in our sample, as well a the mean central emission wavelength for larger nanocubes.

In figure 2.27a the ensemble emission spectra obtained for sample A is shown in comparison to what obtained for larger bulk-like cubes obtained using Protesescu's method[69]. From this image we can see how the size plays a role on the central emission wavelength of the cubes. In panel b) of figure 2.27 the size distribution of nanocubes in sample A is reported, while panels c) and d) reports images of the cubes in sample A obtained with a scanning electron microscope. It is possible to see a variability in the sizes of produced cubes, the larger cubes having a lateral size of several times the smaller ones. A similar variability can be observed for nanocrystals of sample B.

It seems reasonable to attribute to size variability the different central emission wavelengths observed for nanocrystals as shown in figure 2.12. In addition, knowing that the bulk perovskite does not show single photon emission, the increase of the size induces, at a certain point, the loss of the single-photon emission. For this reason we attribute the effect reported on figure 2.26 to the loss of the confinement due to the larger size of the emitters.

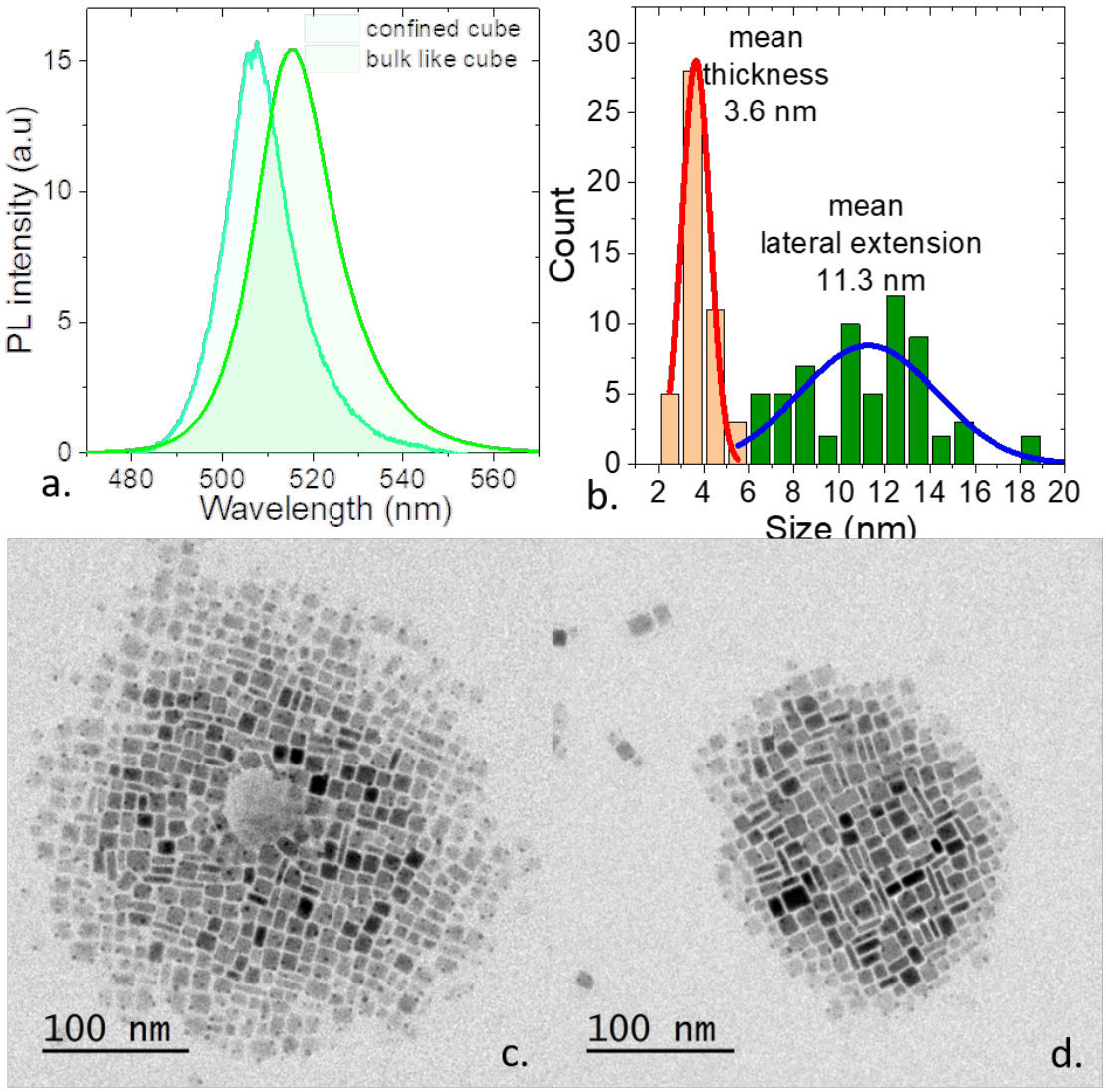

Figure 2.27 – a) PL spectra for confined cubes obtained in sample A and for the bulk like $CsPbBr_3$ cubes from the Protesescu's method[69]. b) Size histogram for the confined cubes showing two peaks which are fitted by two gaussians leading to a mean thickness of 3.6 nm and a mean lateral extension of 11.3 nm. c) and d) are TEM images of the confined cubes

Conclusions

- Perovskites are well known chemical structures in which the interest of the scientific community increases.
- Perovskite nanocrystals are promising single photon emitters but they have stability problems
- polymers can improve the stability of the nanocrystals protecting them from moisture and light, but have the inconvenience to make difficult the coupling of the emitters with integrated platforms
- different fabrication methods can have a huge effect on the emitters' stability
- I have described a fabrication method that
  - improves the stability of the emitters, making them last for more than 1 h
  - produces nanocrystals with a shorter characteristic blinking time and they remain in a bright state even at high excitation power
- I have shown the relation between the central wavelength emission of the emitters and their $g^{(2)}(0)$, showing a loss of single photon emission for higher emission wavelengths

Chapter 3

Coupling nanoemitters to nanofibers

Contents

3.1 Optical fiber 73
3.2 Light propagation inside optical fibers 75
3.2.1 Propagation in a planar guide 75
3.2.2 Propagation in optical fibers 78
3.2.3 Modes of a tapered optical nanofiber 84
3.3 Nanofiber fabrication 90
3.3.1 Choosing the profile of the fiber 90
3.3.2 Pulling mechanism 91
3.3.3 Experimental details 94
3.4 Experimental Setup 97
3.5 Nanocrystal deposition and antibunching measurement on the nanofiber 100

3.1 Optical fiber

By optical fiber, we mean a transparent and flexible cylinder made by a dielectric material that is able to guide light using total internal reflection.

This is a fundamental principle in optics and its discovery is usually attributed to Johannes Kepler[76]. He did not derive the right laws of refraction but he was the first scientist to observe that, while the angle of light incident in water is varied between 0 and 90 deg, the angle of the light propagating inside the water is at maximum for 42 deg. After this first observation and thanks to the contribution of René Descartes, Christian Huygens and Isaac Newton (amongst others), it became clear that light, when going from

a more refractive to a less refractive medium, can be refracted only if the incidence angle is small enough. When the angle is larger than a certain threshold, light is completely reflected. This phenomenon, called total internal reflection, is described by the Snell law which is given by:

$$\frac{\sin \vartheta_2}{\sin \vartheta_1} = \frac{n_1}{n_2} \tag{3.1}$$

where ϑ_1 and ϑ_2 are the incidence angle and the refraction angle respectively, n_1 and n_2 are the refraction index of the first and the second medium respectively (figure 3.1a). It

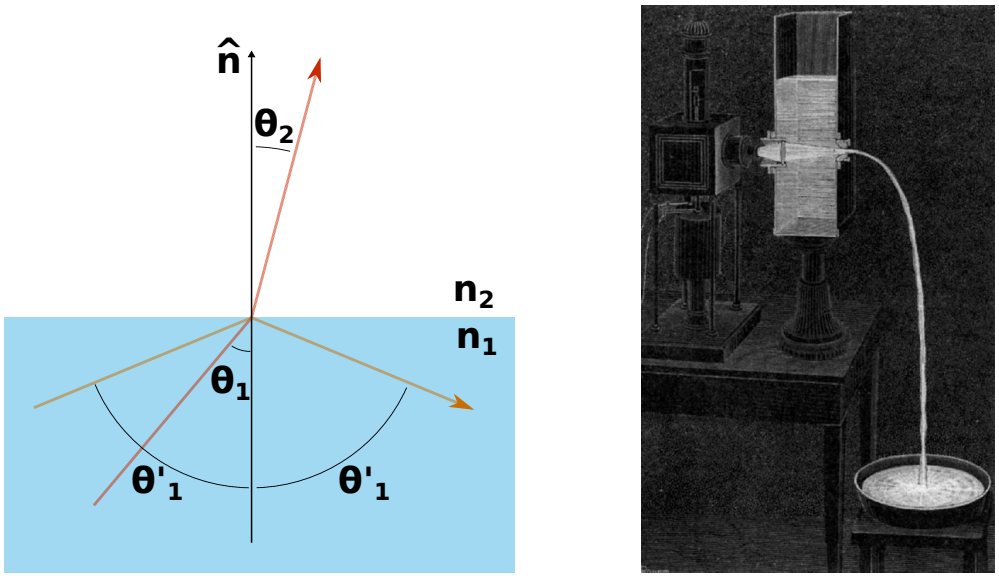

(a) (b)

Figure 3.1 – (a) Low of refraction: the ray in red hits the surface with an angle $\vartheta_1 < \vartheta_l$ with respect to the normal and it is refracted with an angle ϑ_2; the ray in orange hits the surface with an angle $\vartheta_1' > \vartheta_l$ and it is totally reflected. (b) Jean-Daniel Colladon experiment: A tank contains water that falls down through a hole in open air. The light from the lamp on the left side is guided by the water. This image was published in the "La Nature" review in 1884.

is seen that when $n_1 > n_2$, the equation does not have a solution for any ϑ_1. Indeed, we can multiply by $\sin \vartheta_1$ both sides of the equation to obtain

$$\sin \vartheta_2 = \frac{n_1}{n_2} \sin \vartheta_1 \tag{3.2}$$

For this equation to have a solution, we need to have:

$$\frac{n_1}{n_2} \sin \vartheta_1 \leq 1 \Longrightarrow \vartheta_1 \leq \arcsin\left(\frac{n_2}{n_1}\right) \tag{3.3}$$

The angle for which the equality is true is known as limit angle, ϑ_l. We can thus reformulate the description of total internal refraction saying that when the incidence angle is larger than the limit angle, light is completely reflected at the incidence plane. With this principle and neglecting the roughness of the surface, it is possible to guide light. Today this seems trivial, but this possibility has been demonstrated for the first time only in early 1840 by Colladon [77]. The first practical applications of this discovery were used to guide light to illuminate body cavities (as surgical lamp). The scientists tried earlier on to use optical guides to transport information. The first attempt was done with the photophone invented by Bell that used the sun light focused with a lens and a vibrating mirror to translate the vibration of the mirror in optical signal. The vibration on the ray was converted back in electrical signal at the arrival. This system had unfortunately the problem to be unusable in cloudy days, limits that forced Bell to abandon it.

The technique of transmission of information via optical fibers was then used in the second half of the XXth century to capture images from inside the human body and by NASA in cameras that were sent to the moon. For long distance communications, unfortunately, the main problem was the losses too high. At the beginning, the origin of the losses was not understood. The discovery that the losses were caused mainly by glass impurities, (effect that go the Nobel prize to Charles Kuen Kao in 2009) opened the path to low loss fibers that nowadays are broadly used in communication technologies providing a repeater each 150 km is used for very long distance communications.

A fiber is usually made of two collinear cylinders: the core and the cladding, the second one with a refraction index that is slightly lower than the first one. Depending on the cladding size and thus on its ability to transport one ore more optical modes, fibers can be classified into single mode and multi-mode fibers for a given wavelength.

Single mode fibers have usually a core of few micrometers in diameter and a cladding of 125 µm.

In the following I will first explain in detail the mechanism of guiding light inside an optical fiber and the peculiarity of nanofibers before describing the nanofiber fabrication method.

3.2 Light propagation inside optical fibers

3.2.1 Propagation in a planar guide

The intuitive explanation given in the previous section is not sufficient to explain all the underlying physics. To go a step further, let us start with the simple example of

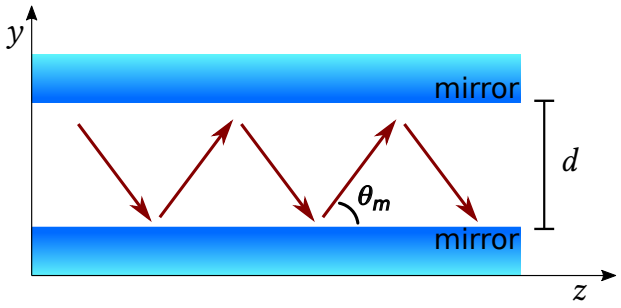

Figure 3.2 – Scheme of the geometrical model for a plane wave propagation between two mirrors. In blue are represented the mirrors, spaced by a distance d. The light propagates along the path indicated in red.

the light guided between two planar mirrors and consider a transverse electric plane wave propagating inside them. This is illustrated in figure 3.2. With transverse electric (TE) we indicate an electromagnetic wave with no electric field in the direction of the propagation. In analogy, transverse magnetic (TM) waves are electromagnetic waves with no magnetic field in the direction of the propagation. Considering the mirrors extending indefinitely in both directions, in order to have constructive interferences, we need to impose the so called "self consistent" condition: all the waves propagating downwards must be in phase, in order to not destructively interfere (this is also valid for all the waves propagating upwards).

A wave that satisfies this condition is called *Mode*: in other words the modes are specific distributions of the electromagnetic field that maintain the same transverse shape (i.e. on the surface orthogonal to the waveguide) and polarization at all the locations along the waveguide axis [78]. If the incident angle for a given mode is ϑ_m, to be self consistent, the optical path between two different reflections has to be an integer multiple of 2π. In this case we have.

$$\sin \vartheta_m = m\frac{\lambda}{2d} \tag{3.4}$$

where λ is the wavelength of the radiation in the medium, d the distance between the planes and m a positive integer, called order of the mode. When this condition is fulfilled, the upward and downward components interfere destructively and only the horizontal component is present. We recall that $\lambda = \lambda_0/n$, where λ_0 is the wavelength of the radiation in void and n the refraction index of the medium. The propagation constant β is given by the modulus of the projection of $\vec{k}$-vector over the y-axis:

$$\beta_m = k \cos \vartheta_m \tag{3.5}$$

using the equation (3.4) and we recall that $\sin^2\vartheta + \cos^2\vartheta = 1$, we can write:

$$\beta_m^2 = k^2 - \frac{m^2\pi^2}{d^2} \tag{3.6}$$

This means that modes of higher order travel with a smaller β constant. The amplitude of the electric field $E_x(y,z)$ can be written as [78]:

$$E_x(y,z) = a_m u_m(y)\, e^{-i\beta_m z} \tag{3.7}$$

where a_m is the amplitude of the mode m, i is the imaginary unit and the u_m are given by equation (3.8).

$$u_m(y) = \begin{cases} \sqrt{\dfrac{2}{d}}\cos\left(m\pi\dfrac{y}{d}\right), & m = 1,3,5,\ldots \\ \sqrt{\dfrac{2}{d}}\sin\left(m\pi\dfrac{y}{d}\right), & m = 2,4,6,\ldots \end{cases} \tag{3.8}$$

From equation (3.4), we can also extract the maximal number of modes M that a mirror guide can accept, given the fact that $\sin\vartheta_m \leq 1$

$$m\frac{\lambda}{2d} \leq 1 \qquad \Longrightarrow \qquad M = \frac{2d}{\lambda} \tag{3.9}$$

the maximal number of modes thus decreases as the ratio between the distance of mirrors and the wavelength of the propagating light decreases.

We can also note that when $\lambda < 2d$, no mode is allowed to propagate in the waveguide and for this reason $\lambda < 2d$ is called the cut-off wavelength. A guide that can guide only one mode (i.e. with $\lambda_c \leq \lambda < 4d$) is called a single-mode waveguide. It is also important to note that, as each mode has a different β_m, it propagates with a different group velocity. The group velocity dispersion is a peculiarity that makes difficult the transmission of information over long distances with multimode waveguides (and fibers).

To conclude the description of the planar waveguide example, we can note that if we want to consider TM modes instead of the TE ones, the mathematical treatment will be similar: an extensive analysis of the physics governing the light propagation in planar waveguides can be found in the book of Saleh and Teich [78].

3.2.2 Propagation in optical fibers

To study light propagation inside an optical fiber, we need to take care of two main differences with respect to the waveguide geometry discussed in the previous paragraph: the cylindrical geometry and the presence of a dielectric core and cladding. In optical fibers, as well as in the planar waveguide seen before, the light propagates in the form of modes of the electromagnetic field : if the core of the fiber is small enough, only one mode can be guided and the fiber is called a single mode fiber, if it is bigger, thus more than one mode can be guided and the fiber is called a multimode fiber. In this second case, as evidenced in the case of planar guide, the optical modes have different group velocities: this normally limits the repetition rate of a pulse that can be transmitted in a long fiber avoiding the overlap with the following pulse. To reduce this problem, graded index multimode fibers can be used, where instead of an abrupt jump between the values of the refraction indices of the core and the cladding, the index decreases continuously from the center to the edge.

In the following, I will first recall the main properties of the step index fibers, with a focus on single mode fibers and I will then describe single mode nanofibers, which will be coupled to a single perovskite nanocube towards building up a hybrid photonic device. A detailed description of these systems can be found in the ninth chapter of *Fundamentals of Photonics* by Saleh and Teich [78].

To obtain the propagation modes for an optical fiber, we need to consider Maxwell equations in a dielectric medium:

$$\begin{aligned} \nabla \times \mathcal{H} &= \frac{\partial \mathcal{D}}{\partial t} \\ \nabla \times \mathcal{E} &= -\frac{\partial \mathcal{B}}{\partial t} \\ \nabla \cdot \mathcal{D} &= 0 \\ \nabla \cdot \mathcal{B} &= 0 \end{aligned} \tag{3.10}$$

For simplicity, we consider our medium to be:

linear – the polarization density vector $\mathcal{P}$ and the electrical field $\mathcal{E}$ are linearly related;

non dispersive – meaning that, at a certain time t, $\mathcal{P}(t)$ is determined by $\mathcal{E}(t)$ but not by $\mathcal{E}(t')$ for any time $t' \neq t$

We can thus write $\mathbf{D} = \varepsilon(\mathbf{r})\,\mathbf{E}$ and $\mathbf{B} = \mu\mathbf{H}$. Now we can distinguish two cases, the case in which the medium is homogeneous and the case in which it is not.

Homogeneous medium

In this first case, the medium is homogeneous i.e. $\varepsilon(\mathbf{r}) = \varepsilon$. Let us consider a monochromatic wave and let us write the electric and magnetic fields as:

$$\begin{aligned}
\mathcal{E}(\mathbf{r},t) &= \Re\left\{\mathbf{E}\left(\mathbf{r}e^{i\omega t}\right)\right\} \\
\mathcal{H}(\mathbf{r},t) &= \Re\left\{\mathbf{H}\left(\mathbf{r}e^{i\omega t}\right)\right\} \\
\mathcal{B}(\mathbf{r},t) &= \Re\left\{\mathbf{B}\left(\mathbf{r}e^{i\omega t}\right)\right\} \\
\mathcal{D}(\mathbf{r},t) &= \Re\left\{\mathbf{D}\left(\mathbf{r}e^{i\omega t}\right)\right\}
\end{aligned} \tag{3.11}$$

where $\mathbf{E}$ and $\mathbf{H}$ are the complex amplitudes vectors of the electric and magnetic fields, respectively, and $\Re$ indicates the real part operator. Maxwell equations (3.10) can thus be simplified as

$$\begin{aligned}
\nabla \times \mathbf{H} &= i\omega\varepsilon\frac{\partial \mathbf{E}}{\partial t} \\
\nabla \times \mathbf{E} &= -i\omega\mu\frac{\partial \mathbf{H}}{\partial t} \\
\nabla \cdot \mathbf{D} &= 0 \\
\nabla \cdot \mathbf{B} &= 0.
\end{aligned} \tag{3.12}$$

By applying the curl operator to the first and the second equations of (3.12), we can derive the wave equation to be satisfied by each complex component u of the electric and the magnetic fields:

$$\nabla^2 u + \frac{1}{c^2}\frac{\partial^2 u}{\partial t^2} = 0 \tag{3.13}$$

where c is the velocity of light in the medium $c = 1/\sqrt{\mu\varepsilon}$. This equation, using the time dependace expressed by the equations (3.11) can be rewritten as

$$\nabla^2 u + k^2 u = 0 \tag{3.14}$$

where $k = nk_0 = \omega\sqrt{\varepsilon\mu}$ with $n = \sqrt{\varepsilon\mu/(\varepsilon_0\mu_0)}$, $k = \omega/c_0$ and $c = c_0/n$, as usual.

Inhomogeneous medium

In this second case, more general, we do not make the homogeneity hypothesis. By following the same mathematical procedure and applying the curl operator to the first and the second equations in (3.10), we obtain different equations for the magnetic and

electric fields:

$$\frac{\varepsilon_0}{\varepsilon}\nabla\times(\nabla\times\mathcal{E}) = -\frac{1}{c_0^2}\frac{\partial^2\mathcal{E}}{\partial t^2} \tag{3.15a}$$

$$\nabla\times\left(\frac{\varepsilon_0}{\varepsilon}\nabla\times\mathcal{H}\right) = -\frac{1}{c_0^2}\frac{\partial^2\mathcal{H}}{\partial t^2} \tag{3.15b}$$

Equation (3.15a) can be rewritten in a different form, more useful. First of all, we can use the relation (valid in a system of linear coordinates):

$$\nabla\times(\nabla\times\mathcal{E}) = \nabla(\nabla\cdot\mathcal{E}) - \nabla^2\mathcal{E}; \tag{3.16}$$

substituting it in (3.15a) we obtain:

$$\frac{\varepsilon_o}{\varepsilon}\left[\nabla(\nabla\cdot\mathcal{E}) - \nabla^2\mathcal{E}\right] = -\frac{1}{c_0^2}\frac{\partial^2\mathcal{E}}{\partial t^2}. \tag{3.17}$$

Now, we multiply both terms by $\varepsilon/\varepsilon_0$ and we use the fact that $c_0 = 1/\sqrt{\varepsilon_0\mu_0}$ to write:

$$\nabla(\nabla\cdot\mathcal{E}) - \nabla^2\mathcal{E} = -\varepsilon\mu_0\frac{\partial^2\mathcal{E}}{\partial t^2}. \tag{3.18}$$

From Maxwell equations (3.10) we know that $\nabla\cdot\mathcal{D} = 0$ and thus $\nabla\cdot(\varepsilon\mathcal{E}) = 0$, so it is true that:

$$0 = \nabla\cdot(\varepsilon\mathcal{E}) = (\nabla\varepsilon)\cdot\mathcal{E} + \varepsilon(\nabla\cdot\mathcal{E}) \Rightarrow \nabla\cdot\mathcal{E} = -\frac{(\nabla\varepsilon)\cdot\mathcal{E}}{\varepsilon} \tag{3.19}$$

Using the result of equation (3.19) in equation (3.18) and moving all terms to the left we obtain:

$$\nabla^2\mathcal{E} - \varepsilon\mu_0\frac{\partial^2\mathcal{E}}{\partial t^2} + \nabla\left(\frac{\nabla\varepsilon}{\varepsilon}\cdot\mathcal{E}\right) = 0 \tag{3.20}$$

We notice here that the last term of this equation is the one that mixes the vector components. In other words, when this therm is zero, the first two terms give rise to 3 scalar equations, one for each component, that are independent. When the last term is not zero on the other hand, the 3 equations are coupled as any component appears in any equation. When the last term is zero, each component satisfies an equation analogous to (3.14).

It is thus important to know the amplitude of these terms to see if the last one can be neglected and when. In particular, the order of magnitude of the different terms is the

following:

$$\nabla^2 \mathcal{E} \approx \frac{E}{\lambda^2} \tag{3.21a}$$

$$\varepsilon\mu_0 \frac{\partial^2 \mathcal{E}}{\partial t^2} \approx \frac{E}{\lambda^2} \tag{3.21b}$$

$$\nabla\left(\frac{\nabla\varepsilon}{\varepsilon}\cdot\mathcal{E}\right) \approx \frac{E}{\lambda^2}\frac{n_1^2 - n_2^2}{n_2^2} \tag{3.21c}$$

where E is the modulus of the electric field and λ the radiation wavelength. When $n_1^2 - n_2^2 \ll 1$ we refer to weak guiding and this is the case for standard fibers. In the opposite case, when this is not true, the third term cannot be neglected. This is the case in tapered optical nanofibers where, as I will show in the following, $n_1 \approx 1.4$ and $n_2 = 1$. In this case, we need to solve the general equation (3.26) and the solution is a bit trickier.

Step index fibers

Let us now consider a monochromatic wave in the form described by equations (3.11), propagating inside a step index fiber. We consider, for simplicity, a core surrounded by a cladding and that the cladding extends indefinitely in space. This is a good approximation when the core is much smaller than the cladding, such as in single mode fibers. The third term in equation (3.21) is thus zero both in the core and the cladding and the equation becomes the Helmholtz equation. When written in radial coordinates, it reads as:

$$\frac{\partial^2 U(r,\varphi,z)}{\partial r^2} + \frac{1}{r}\frac{\partial U(r,\varphi,z)}{\partial r} + \frac{1}{r^2}\frac{\partial^2 U(r,\varphi,z)}{\partial \varphi^2} + \frac{\partial^2 U(r,\varphi,z)}{\partial z^2} + n^2 k_0^2 U(r,\varphi,z) = 0 \tag{3.22}$$

with the modes traveling in the z direction. As done before for the planar waveguide, we chose the z-axis laying in the same direction of the fiber axis. In addition, $U(r,\varphi,z)$ is periodic with respect to the angle φ with a period of 2π, thus we can write:

$$U(r,\varphi,z) = u(r)e^{-jl\varphi}e^{-j\beta z} \tag{3.23}$$

Equation (3.23) implicitly defines l and β: we will see that l corresponds to the order of the solution, while β is called the propagation constant, and has the same physical meaning described for planar waveguides (cfr. equation (3.5)). Substituting equation (3.23) in

equation (3.22) we obtain

$$\frac{d^2u}{dr^2} + \frac{1}{r}\frac{du}{dr} + \left(n^2(r)k_0^2 - \beta^2 - \frac{l^2}{r^2}\right)u = 0 \tag{3.24}$$

.

In order for a mode to be guided, the following conditions must be valid $n_2 k_0 < \beta < n_1 k_0$, where n_2 is the refraction index of the cladding and n_1 the refraction index of the core. It is convenient to define k_T and γ as:

$$k_T^2 = n_1^2 k_0^2 - \beta^2, \qquad \gamma^2 = \beta^2 - n_2^2 k_0^2. \tag{3.25}$$

where k_T and γ are real quantities for guided waves. We can use them to rewrite equation (3.24) in two separate expressions for the core and the cladding:

$$\frac{d^2u}{dr^2} + \frac{1}{r}\frac{du}{dr} + \left(k_T^2 - \frac{l^2}{r^2}\right)u = 0, \quad r < a \quad \text{(core)} \tag{3.26a}$$

$$\frac{d^2u}{dr^2} + \frac{1}{r}\frac{du}{dr} - \left(\gamma^2 + \frac{l^2}{r^2}\right)u = 0, \quad r > a \quad \text{(cladding)} \tag{3.26b}$$

The differential equations (3.26) have well known solutions given by the Bessel functions of the first kind $J_l(k_T r)$ for equation (3.26a) and the modified Bessel functions of the second kind $K_l(\gamma r)$ for any order l.

It is useful to note that from equations (3.25), we can deduce that $k_T^2 + \gamma^2$ is constant and equal to $\left(n_1^2 - n_2^2\right)k_0^2$.

With some geometrical considerations [78], it is possible to show that:

$$\sqrt{n_1^2 - n_2^2} = \mathrm{NA} \tag{3.27}$$

where the numerical aperture NA is defined as the sine of the maximal acceptance angle, i.e. the maximal angle ϑ_a with respect to the longitudinal axis the light, previously propagating in air, can have to be guided: $\mathrm{NA} = \sin\vartheta_a$. Thus we can state that:

$$k_T^2 + \gamma^2 = (\mathrm{NA})^2 k_0^2. \tag{3.28}$$

An important parameter in fibers is the so called fiber parameter or V-parameter, defined as:

$$\mathrm{V} \stackrel{\text{def}}{=} \mathrm{NA}\, k_0 a = 2\pi\frac{a}{\lambda_0}\mathrm{NA} \tag{3.29}$$

where a is the fiber radius. The V-parameter, also called fiber parameter, determines the number of allowed modes in the fiber, as I will show in the following and their propagation constant. Additionally if we define $X = k_T a$ and $Y = \gamma a$ as the normalized parameters, we can write:

$$X^2 + Y^2 = V^2 \tag{3.30}$$

.

If now we consider the case of a weakly guiding fiber, as most of the fibers are, most of guided rays are paraxial, as $n_1^2 - n_2^2 \ll 1$. In this case the term (3.21c) is negligible and equation (3.20) becomes analogous to equation (3.14). By imposing the continuity of the function $u(r)$ and of its derivative at $r = a$, we obtain [78] the following equation, known as characteristic equation:

$$X\frac{J_{l\pm1}(X)}{J_l(X)} = \pm Y\frac{K_{l\pm1}(Y)}{K_l(Y)} \tag{3.31}$$

Using the fact that $X^2 + Y^2 = V^2$ we can rewrite Y in function of X

$$X\frac{J_{l\pm1}(X)}{J_l(X)} = \pm\sqrt{V^2 - X^2}\frac{K_{l\pm1}(\sqrt{V^2 - X^2})}{K_l(\sqrt{V^2 - X^2})} \tag{3.32}$$

. This equation can be solved graphically, plotting the left and the right side terms as a function of X and looking for their intersections. This is represented in figure 3.3: in blue is represented the term on the right side, while in orange is represented the term on the left side. The solutions are represented by the intersections between the two curves. Any intersection represents a possible solution, i.e. a possible guided mode. As the first term is independent from V, it is clear that the number of intersections can be determined looking at the second term. In particular, when $V < 2.405$ there will be only one intersection between the blue and the orange curves, meaning that only the mode LP_{01} is a solution and is thus allowed. In this case, the fiber is a single mode fiber. We can rewrite this condition recalling the definition of V in the form:

$$\frac{2\pi a}{\lambda_0}\mathrm{NA} < 2.405 \qquad \Rightarrow \qquad a < 2.405\frac{\lambda_0}{2\pi\sqrt{n_1^2 - n_2^2}} \tag{3.33}$$

Equation (3.33) represents a very important condition in order to obtain single mode fibers in practice.

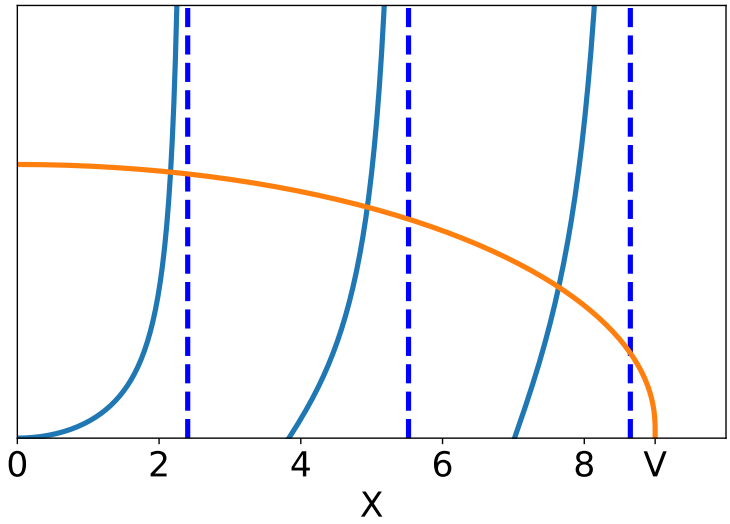

Figure 3.3 – Graphical solutions of the equation (3.31) for $l = 0$. In blue, the term on the left side, independent from V, in orange the term on the right side. The dashed lines marks the asymptotes where the equation is not defined.

3.2.3 Modes of a tapered optical nanofiber

We described in the previous section the main characteristics of a standard optical fiber. In the following, we detail the case of a nanofiber. A nanofiber is also an optical waveguide but with a diameter dimension comparable or even smaller than the wavelength of the guided light. In this case, we cannot consider anymore that the light is traveling totally inside the nanofiber. We will see that, in this case, there is a strong evanescent field extending outside the nanofiber. The light is guided between the nanofiber and the air surrounding it, thus in this case the approximation that $n_1^2 - n_2^2 \ll 1$ is not valid anymore. It is still possible to use equations (3.26) and their solutions are given by the solution of a generalized characteristic equation:

$$\left[\frac{J_v'(\mathrm{X})}{\mathrm{X}J_v(\mathrm{X})} + \frac{K_v'(\mathrm{Y})}{\mathrm{Y}K_v(\mathrm{Y})}\right]\left[n_1^2\frac{J_v'(\mathrm{X})}{\mathrm{X}J_v(\mathrm{X})} + n_2^2\frac{K_v'(\mathrm{Y})}{\mathrm{Y}K_v(\mathrm{Y})}\right] = \beta^2\frac{l^2}{k^2}\left(\frac{1}{\mathrm{X}^2} + \frac{1}{\mathrm{Y}^2}\right)^2 \tag{3.34}$$

where X, Y, and V are the same quantities defined in the previous section.

Equation (3.34) gives origin to different families of modes: HE_{vm} and EH_{vm}, where v and m characterize the azimuthal and the radial distributions respectively. In the special case in which $v = 0$, the z component of the electric field and the magnetic fields are zero, giving origin to the transverse electric and transverse magnetic modes TE and TM.

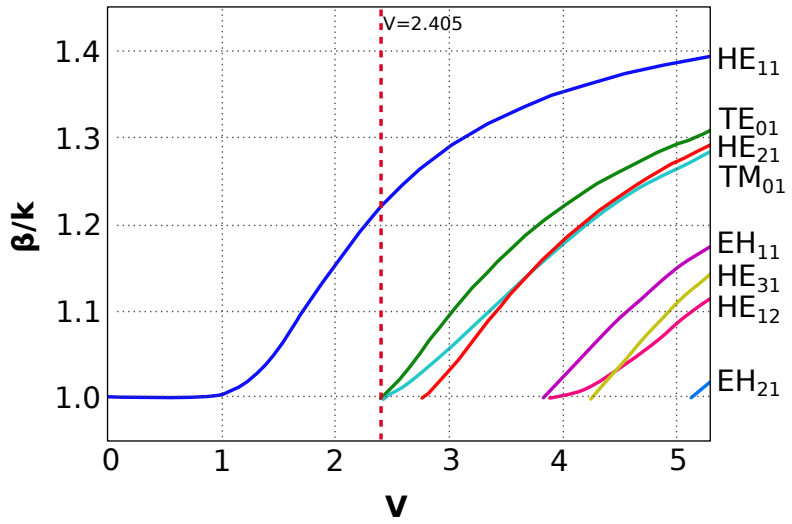

Figure 3.4 – Guided modes of a nanofiber, allowed values of β/k as a function of V. The red dashed line indicates the threshold of V under which the nanofiber is single mode where the HE_{11} mode only is allowed. The graphs are obtained by solving numerically equations (3.35) for a silica glass waveguide with a constant refraction index $n_1 = 1.46$.

We thus obtain [79]:

$$\left\{\frac{J_v'(\mathrm{X})}{\mathrm{X}J_v(\mathrm{X})}+\frac{K_v'(\mathrm{Y})}{\mathrm{Y}K_v(\mathrm{Y})}\right\}\left\{\frac{J_v'(\mathrm{X})}{\mathrm{X}J_v(\mathrm{X})}+\frac{n_2^2K_v'(\mathrm{Y})}{n_1^2\mathrm{Y}K_v(\mathrm{Y})}\right\}=\left(\frac{v\beta}{kn_1}\right)^2\left(\frac{\mathrm{V}}{\mathrm{XY}}\right)^4 \qquad \boxed{\begin{matrix}HE_{vm}\\EH_{vm}\end{matrix}} \qquad (3.35a)$$

$$\frac{J_1(\mathrm{X})}{\mathrm{X}J_0(\mathrm{X})}+\frac{K_1(\mathrm{Y})}{\mathrm{Y}K_0(Y)}=0 \qquad \boxed{TE_{0m}} \qquad (3.35b)$$

$$\frac{n_1^2J_1(\mathrm{X})}{\mathrm{X}J_0(\mathrm{X})}+\frac{n_2^2K_1(\mathrm{Y})}{YK_0(\mathrm{Y})}=0. \qquad \boxed{TM_{0m}} \qquad (3.35c)$$

It is possible to solve numerically these equations and to find the mode solutions. The first solutions of these equations for a glass nanofiber are reported in figure 3.4. When $V < 2.405$, only one solution, the mode HE_{11}, is admitted while the others are not. This means that in the case of $V < 2.405$ the nanofiber can be considered a single mode fiber and for this reason the mode HE_{11} is called the fundamental mode of the fiber. In our experiment, we choose the diameter of the nanofiber so that we only have the fundamental mode guided by the nanofiber. Looking at figure 3.4, we can also notice that in all the solutions we have $n_2k < \beta < n_1k$. For this reason, we can define an effective refractive index of the nanofiber as

$$n_{eff} = \frac{\beta}{k} \qquad (3.36)$$

and consider at it as the index propagation of the light that a certain mode actually "sees". From this point of view, it is clear that it has to be in between n_2 and n_1.

Considering now the fundamental mode, it is useful to calculate the field distribution of this mode. Indeed, in order to optimize the near field coupling, the knowledge of the spatial distribution of electrical field is important. The characteristic equation for this mode becomes:

$$\frac{J_0(\mathrm{X})}{\mathrm{X}J_1(\mathrm{X})} = -\frac{n_1^2+n_2^2}{2n_1^2}\frac{K_1'(\mathrm{Y})}{\mathrm{Y}K_1(\mathrm{Y})} + \frac{1}{\mathrm{X}^2} - \left\{\left[\frac{n_1^2-n_2^2}{2n_1^2}\frac{K_1'(\mathrm{Y})}{\mathrm{Y}K_1(\mathrm{Y})}\right]^2 + \frac{\beta^2}{n_1^2k^2}\left(\frac{1}{\mathrm{X}^2}+\frac{1}{\mathrm{Y}^2}\right)^2\right\}^{1/2} \tag{3.37}$$

It is useful to define the parameter s as follows:

$$s = \frac{\frac{1}{\mathrm{Y}^2}+\frac{1}{\mathrm{X}^2}}{J_1'(\mathrm{X})/(\mathrm{X}J_1(\mathrm{X})) + K_1'(\mathrm{Y})/(\mathrm{Y}K_1(\mathrm{Y}))} \tag{3.38}$$

The electric field can be written as follows for $r < a$:

$$E_r(r,\varphi,z,t) = iA\frac{\beta}{2k_T}\left[(1-s)J_0(k_Tr) - (1+s)J_2(k_Tr)\right]e^{i(\omega t-\beta z)} \tag{3.39a}$$

$$E_\varphi(r,\varphi,z,t) = -pA\frac{\beta}{2k_T}\left[(1-s)J_0(k_Tr) + (1+s)J_2(k_Tr)\right]e^{i(\omega t-\beta z)} \tag{3.39b}$$

$$E_z(r,\varphi,z,t) = fAJ_1(k_Tr)e^{i(\omega t-\beta z)} \tag{3.39c}$$

where A is a normalization constant that can be determined *a posteriori*, p depends on the polarization ($p = 1$ in case of a clockwise polarization and $p = -1$ in case of an anticlockwise polarization) and f depends on the propagation direction ($f = 1$ for a forward propagating mode and $f = -1$ for a backward propagating mode). Similarly, we can write these equations for $r > a$:

$$E_r(r,\varphi,z,t) = -iA\frac{\beta}{2\gamma}\frac{J_1(\mathrm{X})}{K_1(\mathrm{Y})}\left[(1-s)K_0(\gamma r) + (1+s)K_2(\gamma r)\right]e^{i(\omega t-\beta z)} \tag{3.40a}$$

$$E_\varphi(r,\varphi,z,t) = -pA\frac{\beta}{2\gamma}\frac{J_1(\mathrm{X})}{K_1(\mathrm{Y})}\left[(1-s)K_0(\gamma r) - (1+s)K_2(\gamma r)\right]e^{i(\omega t-\beta z)} \tag{3.40b}$$

$$E_z(r,\varphi,z,t) = fA\frac{J_1(\mathrm{X})}{K_1(\mathrm{Y})}K_1(\gamma r)e^{i(\omega t-\beta z)} \tag{3.40c}$$

In this case, by analogy with the weakly guiding case [80, 81], has been referred in literature as *quasi-circular* modes [82, 83]. Anyway, this does not mean that the polarization is truly circular. The field intensity distribution for these modes is represented in

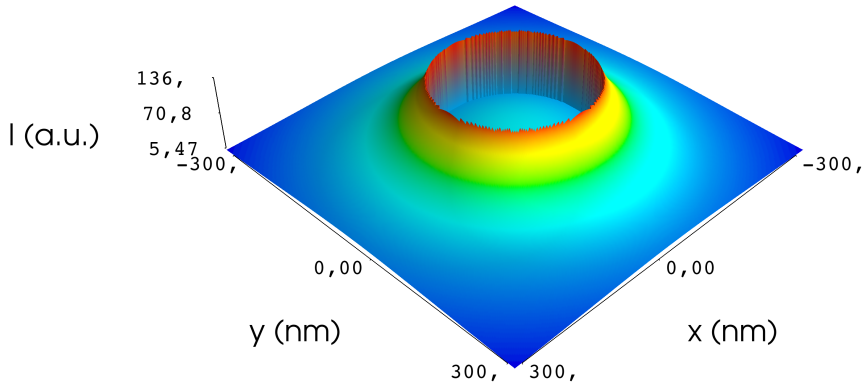

Figure 3.5 – Quasi circular modes: calculated intensity distribution for the modes HE_{11}^{+} and HE_{11}^{-} guided by a nanofiber with a radius $a = 125\,\text{nm}$. The light used in the simulation has a wavelength $\lambda = 500\,\text{nm}$.

figure 3.5. It is important to note that any linear superposition of any two orthogonal

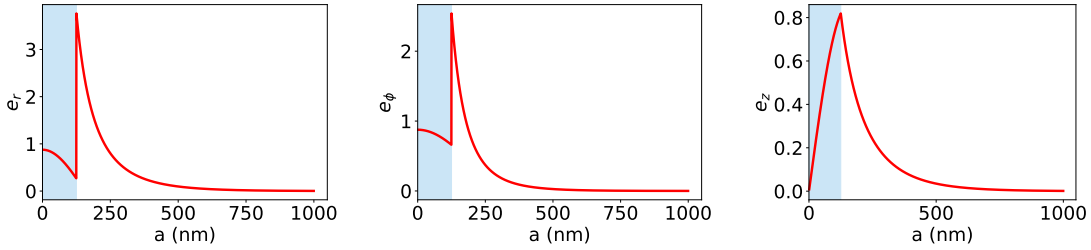

(a) (b) (c)

Figure 3.6 – (a) Modulus of the electrical field E_r of the mode HE_{11} of the fiber, calculated for $t = 0$ and $z = 0$, (b) Modulus of the electrical field E_φ of the mode HE_{11} of the fiber, calculated for $t = 0$ and $z = 0$, (c) Modulus of the electrical field E_z of the mode HE_{11} of the fiber, calculated for $t = 0$ and $z = 0$.

modes is still a solution. If we call HE_{11}^{+} and HE_{11}^{-} the modes with $p = \pm 1$, we can create a new pair of orthogonal modes $\left\{HE_{11}^{+} \pm HE_{11}^{-}\right\}$. It is useful to express them in cartesian

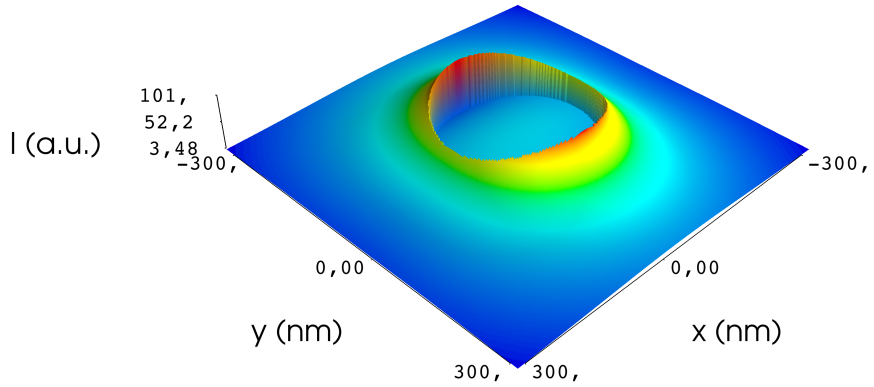

Figure 3.7 – Quasi-linear modes: calculated intensity distribution for the modes $\left\{HE_{11}^{+} \pm HE_{11}^{-}\right\}$ guided by a nanofiber with a radius $a = 125\,\text{nm}$. The light used in the simulation has a wavelength $\lambda = 500\,\text{nm}$. The reported mode is the quasi-polarized one along the y-axis, the other is similar but rotated by 90° and thus quasi-polarized along the x-axis.

coordinates, for $r > a$ we obtain:

$$E_x(r,\varphi,z,t) = -iA\frac{\beta}{2q}\frac{J_1(\mathrm{X})}{K_1(\mathrm{Y})}\left[(1-s)K_0(\gamma r)\cos(\varphi_0) + (1+s)K_2(\gamma r)\cos(2\varphi-\varphi_0)\right]e^{i(\omega t-\beta z)} \tag{3.41a}$$

$$E_y(r,\varphi,z,t) = -iA\frac{\beta}{2\gamma}\frac{J_1(\mathrm{X})}{K_1(\mathrm{Y})}\left[(1-s)K_0(\gamma r)\sin(\varphi_0) + (1+s)K_2(\gamma r)\sin(2\varphi-\varphi_0)\right]e^{i(\omega t-\beta z)} \tag{3.41b}$$

$$E_z(r,\varphi,z,t) = A\frac{J_1(\mathrm{X})}{K_1(\mathrm{Y})}K_1(\gamma r)\cos(\varphi-\varphi_0)\,e^{i(\omega t-\beta z)} \tag{3.41c}$$

with φ_0 defining two orthogonal polarizations, usually $\varphi_0 = \{0, \pi/2\}$. The intensity distribution for these modes is represented in figure 3.7. As we can see, in this case the axial cylindrical symmetry is broken. These modes, by analogy with free space, are called quasi linear modes.

From the field distribution it is clear that the guided field in our example is strongest outside the nanofiber, in its proximity. This, as expected, depends on the radius of the fiber: increasing the radius will decrease the evanescent field and the field is more and more guided inside the nanofiber. Vice-versa, decreasing the nanofiber radius will increase the evanescent field while the field contained inside the nanofiber will decrease. This can be understood thinking in terms of different limit cases: when the fiber radius is much bigger than the wavelength we have a standard fiber where the light is fully

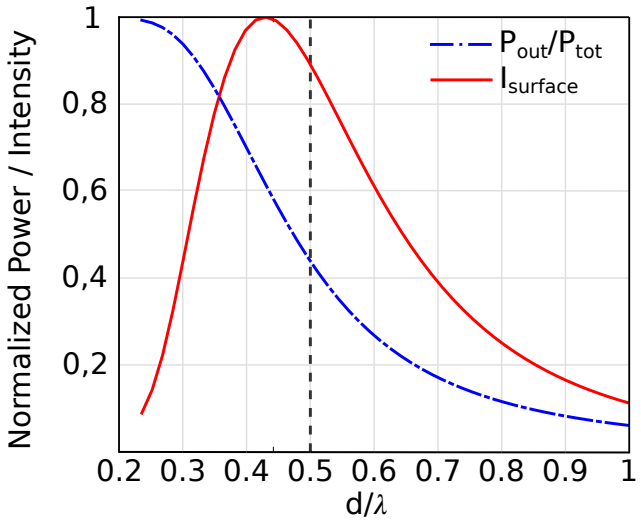

Figure 3.8 – In the figure, we show the comparison between the power and the intensity of the fundamental mode. The blue curve represents the ratio between the power that is guided inside and outside the fiber, while the red curve represents the intensity of the field at the surface, both of them are normalized. Both the curves are normalized to their respective maximum. These curves are calculated for $n_1 = 1.46$ and $n_2 = 1$. The black dashed line represents the diameter we choose for the pulling (fabrication of the nanofiber). Smaller diameters present problems of mechanical stability.

guided inside the fiber; in the opposite case, when the radius is much smaller than the wavelength the light is almost completely outside the nanofiber. In this second case, in the ideal case, with the radius equal to zero, there is no fiber anymore and the light is not guided anymore, we have the propagation of a plane wave. This means that there is an optimal radius in order to have a strong evanescent field together with a guided mode and a nanofiber sufficiently mechanically stable. The optimum turns out to be $r \approx \lambda/4 = 125\,\text{nm}$. This can be seen in figure 3.8, where the comparison between the intensity at the surface and the ratio of the power guided outside the fiber is shown. The dashed line represents our fiber diameter: a slightly smaller diameter can be done to increase the intensity at the surface of about 10 % but it comes with more stability problems.

As we will see in the following sections, this allowed us to obtain a transmission in the fiber up to 98% while preserving a good mechanical stability of the nanofiber which could be fabricated and manipulated without breaking it.

3.3 Nanofiber fabrication

I will describe in this section the experimental setup we use in the laboratory to fabricate the nanofibers. Beside the desired final diameter, we need to be able to control also the shape of the nanofiber in order to adiabatically guide the light from the standard fiber to the nanofiber and vice-versa as I will describe.

3.3.1 Choosing the profile of the fiber

A possible way, which is probably the simplest solution, to obtain a nanofiber from a standard fiber without loosing the transmission is to slowly reduce the radius up to reaching the targeted diameter. This procedure can theoretically work and if the radius variation is slow enough, in principle it is possible to adiabatically guide the mode of the original fiber towards the one of the nanofiber. Unfortunately this procedure necessitates very long transition regions, that presents numerous practical inconveniences. One of the main problem is the mechanical stability: when the tapered and thin part of the fiber is very long, the fiber is much more sensitive to the mechanical vibrations. Therefore, when the transition region becomes too large, moving the fiber from a setup to another is a complex operation with a high risk of breaking the fiber. In addition, the fabrication setup is usually limited in space and it does not allow to fabricate long tapered regions. In our setup, it is possible to obtain tapered regions of few centimeters.

For all of these reasons, it is preferable to produce a transition region that is as short as possible, compatible with our requirements about the transmission. A good method to calculate the ideal profile has been described by Nagai and Aoki [84]. In practice the tapered angle needs to be in any point small enough such that the power coupling from the fundamental mode to the higher-order modes is negligible. To quantify this, it is useful to define the delineation angle Nagai and Aoki [84] and Love *et al.* [85] $\Omega(r)$ such that:

$$\Omega(r) = \frac{r}{2\pi}\left(\beta_1(r) - \beta_2(r)\right). \tag{3.42}$$

This angle provides an approximate delineation between approximately adiabatic and lossy tapers [85]. In the previous equation, $\beta_1(r)$ and $\beta_2(r)$ are the propagation constants of the first and second order modes, respectively. In addition, we can define the adiabaticity factor as:

$$\vartheta(r) < F\Omega(r). \tag{3.43}$$

The smaller F is, the best transmission we can expect from the nanofiber. In particular

when keeping $F < 0.4$, it is possible to obtain fibers with a transmission over 98 %[84].

In our platform, we use a Matlab routine to calculate and simulate the fiber profile before the pulling, routing that generates the instructions for the motors used during the pulling itself as I explain in the following.

3.3.2 Pulling mechanism

One of the most reliable ways of producing a nanofiber is to start with a standard fiber, heat the glass and pull it in order to reduce its diameter. This is conceptually not very different from the standard way to shape glass. It relies on the fact that the glass is an amorphous material that can be easily shaped by heating it to change its viscosity coefficient. In the case of standard glass, this is usually heated at 800 °C inside an oven. A man heating the glass for this purpose in the Murano island is shown in figure 3.9. In order to

Figure 3.9 – A man heating up glass in order to obtain the desired shape in the Island of Murano, Italy. *credits: Zanetti Murano Studio.*

pull the nanofiber, we use the setup shown in figure 3.10. The fiber is clamped between two translation stages and pulled over a clean flame of oxygen and hydrogen. The procedure is detailed in section 3.3.3. Before the practical description of the experiment, i is useful to understand the physical model on which it relies.

In the case of fiber pulling, the procedure has been described in details by Birks

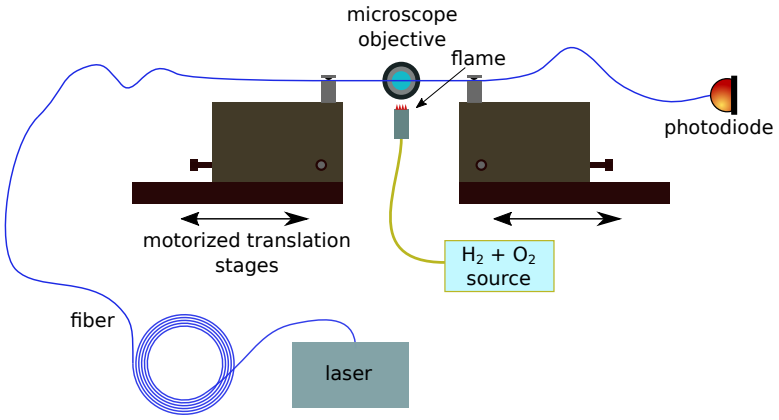

Figure 3.10 – Experimental setup for pulling nanofibers. The laser is used to constantly monitor the transmission during the process.

and Li [86]. The variation of the viscosity of the fiber is generally described by fluid-mechanics [87], but it can be approximated as a cylindrical melting zone of a length L_0 also called in the following effective flame diameter. If we pull the fiber without moving the flame we obtain a waist with the diameter described by the following equation:

$$r(x) = r_0 \exp -\frac{z_e}{2L_0} \tag{3.44}$$

where r_0 is the initial fiber radius, rx the radius after extending the fiber of a length z_e, while in the transition area the profile is given by

$$r(z) = r_0 \exp -\frac{z}{2L_0} \tag{3.45}$$

where we placed the origin in the last unprocessed point of the fiber and it increases towards the waist. In this way, by simply pulling the fiber over the flame, only one shape can be produced and for this reason a more versatile technique is needed, to be able to realize the appropriate profile.

To understand better the physics behind it, we need to make two simple assumptions:

- the glass in the heated region is soft enough to be stretchable but is hard enough not be stretched by its own weight and the other parts of the fiber, outside the heated region, are solid and non stretchable,
- the volume of the glass does not change significantly due to the heating and the conservation of the volume comes from the conservation of the mass.

From these assumptions, we can use the mass conservation to state that the volume of

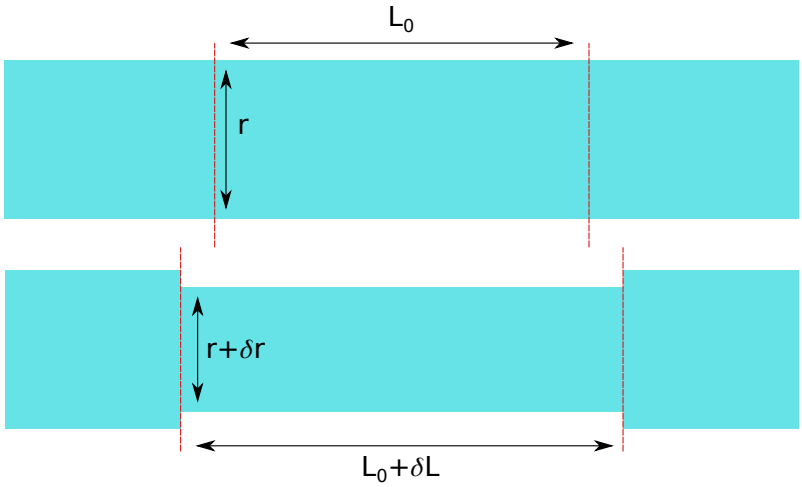

Figure 3.11 – Scheme of the fiber pulling. When the fiber is pulled by a small length δL, the region heated by the flame increases its length from L_0 to $L_0 + \delta L$. At the same time, the radius of the region changes due to the volume conservation and becomes $r + \delta r$ with $\delta r < 0$. This scheme is valid when δL is small enough to allow the transition region to be neglected.

the heated cylinder at the time t and the volume after the pulling at the time $t + \delta t$ must be the same leading to equation (3.46):

$$\pi (r + \delta r)^2 (L_0 + \delta L) = \pi r^2 L \tag{3.46}$$

where δr is the variation of the radius (and thus a negative quantity), L is the length of the taper and δL is the length of the fiber which has been pulled. The meaning of the parameters is clarified in figure 3.11.

In the limit $\delta L \longrightarrow 0$, we can derive equation (3.47) from equation (3.46) [86]:

$$\frac{dr}{dL} = -\frac{r}{2L} \tag{3.47}$$

We thus found that, by controlling the pulling, we can control the final radius of the heated zone. We can deduce that with multiple pulling steps and L small enough so that we can obtain an arbitrary profile. To obtain from equation (3.47) the pulling procedure necessary to obtain a given profile, there is no analytical solution and it is necessary to proceed numerically (see Birks and Li [86]). In conclusion, it is possible to find a procedure in order to obtain the desired shape for the transition region. This involves the ability to pull while translating the flame under the nanofiber in order to be able to choose δL and the heated region. For practical reasons, it is more suitable to keep

the flame fixed and to move the fiber back and forth instead, resulting in a translation movement superposed to the pulling one. Usually, the pulling procedure is constituted by different consecutive pulling steps that reduces progressively the radius, approximating at the best the calculated optimal desired profile .

To perform these calculations, in the lab we use a matlab code, that generates a file with the instructions in terms of movements of the stages in order to produce the correct profile.

The heating can be performed using a flame or a focused CO_2 laser. In our case, a flame of hydrogen and oxygen was chosen as it presents less alignment inconvenience than a laser spot. In different situations, especially when spatial constraints are present, the laser can be the best option.

3.3.3 Experimental details

The fiber is placed over a pure flame of hydrogen and oxygen. The amount of gas is controlled by two gas mass flow controllers that allows a fine control over the gas flow and, consequently, over the flame size. When the pulling starts, a motor moves the flame near the fiber. At the same time, the fiber is translated and pulled via two precise translation stages following the instructions written in a text file. The whole procedure is controlled by the computer: at the end of the pulling phase, the flame is moved away from the fiber. During the process, we constantly monitor the transmission of the fiber in order to have information on the quality of the pulling. The transmission is monitored measuring the transmitted light with a photodiode as a function of the time normalized to the power transmitted at the beginning of the pulling. This is accurate as long as all the other parameters of the set-up are unchanged (laser emitted power, coupling of the laser, etc). An example of the intensity trace measured is reported in figure 3.12.

A microscope objective with a large working distance is used to monitor the fiber position and to correctly place the flame under the fiber. A picture of the pulling setup is reported in figure 3.13

The procedure for the fiber pulling is composed of several steps, all of them are crucial for obtaining an optimal result.

1. We start from a standard fiber. In this particular case of the experiment, I start with a Thorlabs SM450 fiber. The first step is to couple the laser inside the fiber and send the output light from the fiber to the photodiode in order to monitor its transmission

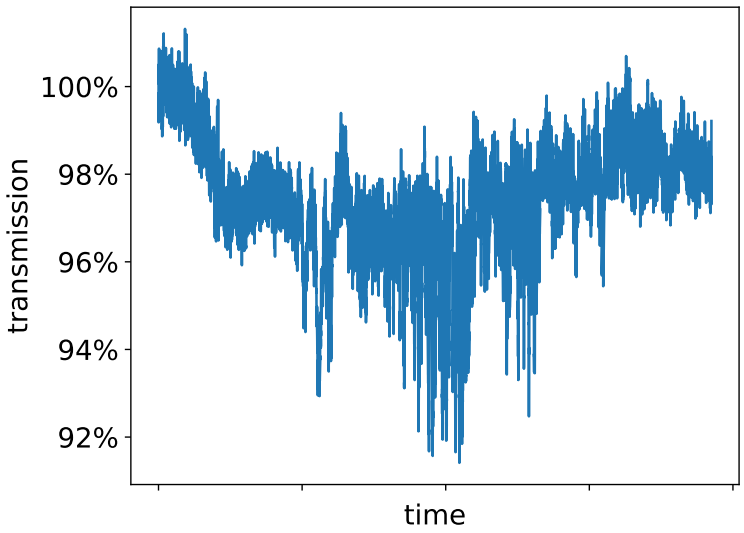

Figure 3.12 – Intensity trace measured during the fiber pulling process. The trace starts at the beginning of the pulling phase and it is recorded until its end. At the beginning, the transmission is 100 %, during the pulling we loose part of the transmission (down to 92 %) while the profile is not optimal, but it is partially recovered when the nanofiber reaches its final shape.

2. We switch on the flame opening the flux of oxygen and using an electrical gas lighter. We then open the hydrogen flux, verifying that the flame changes color and gets from red to blue, meaning that the correct temperature is reached (the burning temperature of hydrogen and oxygen is 2660 °C).

3. Commercial fibers are covered by an acrylate jacket to give them a better mechanical resistance. It is important to remove it in the part that we want to pull (few centimeters are normally enough), using a fiber stripper.

4. A special care needs to be done for cleaning the fiber in order to remove any dust. Any residual dust will burn under the flame and reduce the final achieved transmission. The first step is to wipe the fiber with isopropanol to remove any trace of grease present on it as well as the powder left by the jacket removal. Secondly, we use acetone on the uncovered part to dissolve residual traces of the jacket that are still in place. We finally clean again with isopropanol.

5. The fiber is placed on the holder and blocked with two mechanical clamps. The whole setup is under a clean laminar air-flow, to avoid the presence of dust and to reduce the oscillation of the fiber.

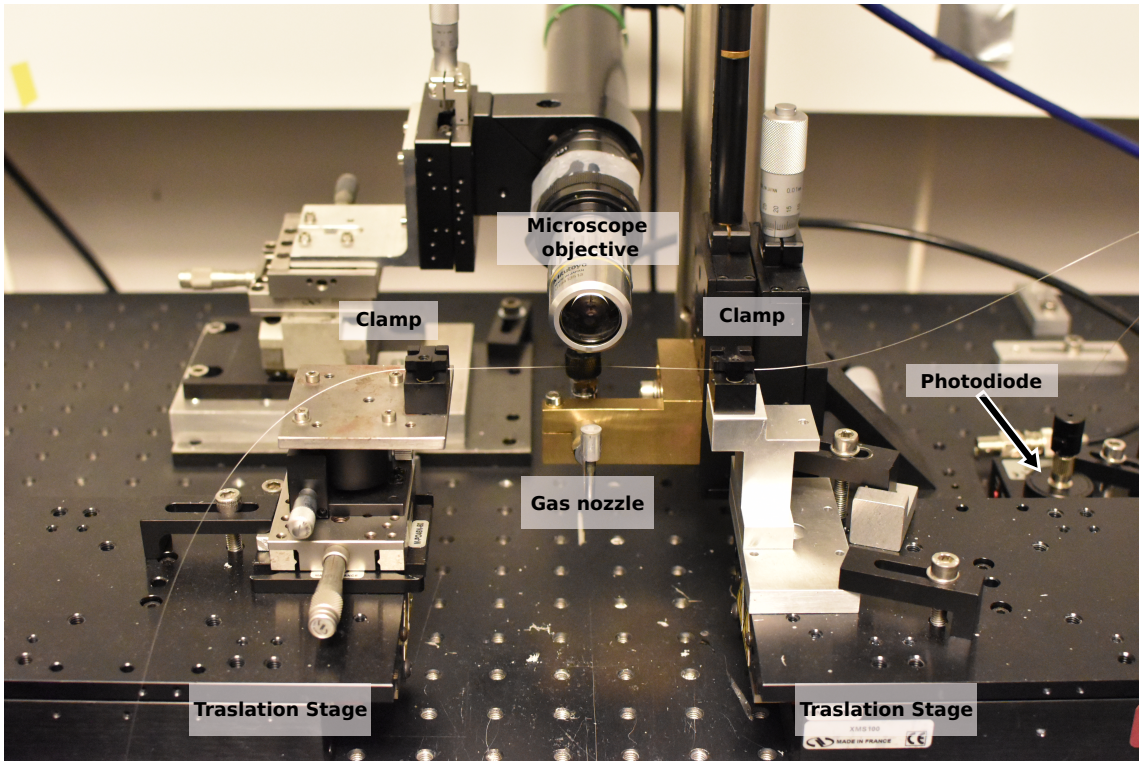

Figure 3.13 – Photo of our pulling setup: the fiber has been pulled and it is clamped between two supports. At the center is visible the microscope objective, while under the fiber, it is possible to see the gas nozzle where the flame burns. At the left and right bottom of the picture, the two translation stages that control the pulling are visible.

6. The pulling starts with the profile previously calculated. The computer controls the movement of the translation stages (left and right) and of the flame (up and down). During the pulling, it is necessary to adjust the flame position as the fiber is slightly pushed up by the lifting hot air around the flame.

7. Once the pulling is successfully achieved the flame is moved away from the fiber by the computer. It is important to automate this task as timing is crucial in the success of the pulling procedure, if the flame is not removed when the pulling stops, the fiber can break.

8. It is useful to slightly increase the tension of the nanofiber to reduce its vibrations. This is done by monitoring the fiber position with the microscope and moving the translation stages (usually few micrometers is enough). In this situation, the nanofiber dimension is below the microscope resolution but it is possible to see its luminescence if we keep the room in the dark.

9. The fiber is now ready and we can switch off the flame.

Following this protocol we are usually able to produce nanofibers with a transmission of 98 % which is enough for our experiments. Better transmissions have been reported in the literature. With accurate optimization of the setup and of the fiber profile, Nagai and Aoki [84] claim to be able to produce nanofibers with more than 99.7 % of transmission. The pulling phase requires few minutes, but if we consider the whole procedure, we can estimate that two hours is necessary to fabricate a nanofiber. The success rate depends largely on the ability of the experimenter but we can consider one success for two trials.

Once the pulling is completed, we need to move the fiber to the experiment. This is how it is done:

1. In order to move the fiber, we need to fix it to its final support. We asked the mechanical service of the lab to produce some U-shaped support that can maintain the fiber fixed during the experiment. To fix the fiber onto it we:
   - use a translation stage to place the holder directly under the nanofiber, until it gently touches it;
   - we glue the fiber on the holder using a UV glue. This step needs a particular care as the nanofiber is very fragile.
2. We place the nanofiber in a clean and hermetic plastic box to avoid the deposition of dust over the nanofiber. We made two small notches in the box to allow the fiber to exit from it.
3. Once the box is closed, we can disconnect the fiber from the photodiode and stop monitoring the transmission. We cut the fiber in order to have about 50 cm at each ends and we carefully move the box with the nanofiber from the pulling setup to the experiment.
4. We weld the two extremities of the tapered fiber to the fibers of the experiment using a splicing machine in order to minimize losses. Usually, losses in the connection are below the instrument sensitivity (i.e. 0.1 dB) and thus small enough.

3.4 Experimental Setup

The setup used for our experiment is shown in figure 3.14. A photo of the setup is reported in figure 3.15. The setup allows to excite the emitter on the fiber both from

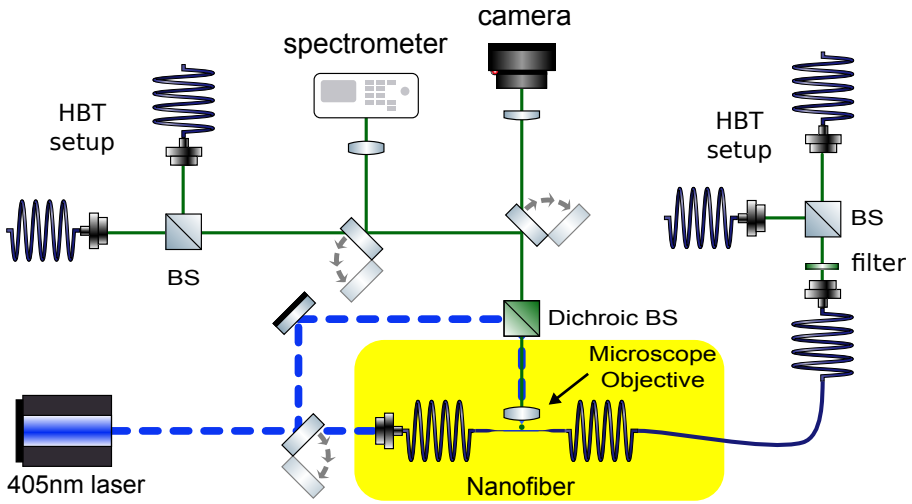

Figure 3.14 – Setup for the nanofiber experiment: a blue pulsed laser can excite the emitter both from the nanofiber and from freespace. The image and the spectra of the nanocrystals can be recorded using a camera. Ultimately, it is possible to perform the $g^{(2)}$ measurement in both configurations. The part surrounded by in yellow is placed in a box under a clean laminar air-flow. BS: non polarizing beamsplitter, HBT: Hanbury Brown and Twiss.

the nanofiber and from the free space thanks to a home-made confocal microscope. By the same token, the luminescence of the emitter can be collected by the microscope objective, analyzed with the camera or the spectrometer or sent to the HBT setup to perform the $g^{(2)}$ measurement. It is also possible to connect directly the fiber to the $g^{(2)}$ measurement, in order to study the light that is coupled to the nanofiber via the near field coupling.

It is important to stress the fragility of the nanofiber in any experimental procedure. In particular we have shown that most of the mode propagates outside the nanofiber: this makes it possible to couple the light emitted by the nanocrystal directly into the fiber through the near field coupling but it implies also that any kind of dust lying over the nanofiber can disturb the light propagation and reduce the transmission. For this reason, it is essential to protect the fiber from dust using a clean air laminar glow. This is obtained by surrounding the part of the experiment in yellow in figure 3.14 with a box and sending a laminar flow inside it. This has also the advantage of protecting the fiber from any accidental shock and to protect the experimentalist from accidentally touching the nanofiber. Indeed, the diameter of the nanofiber is smaller than the size of the pores of the skin (usually 50 µm) and for this reason can be dangerous to touch it.

In the following, I will explain how we deposit the nanocrystals on the nanofiber and I will discuss the experiment we performed, concluding with the results we obtained.

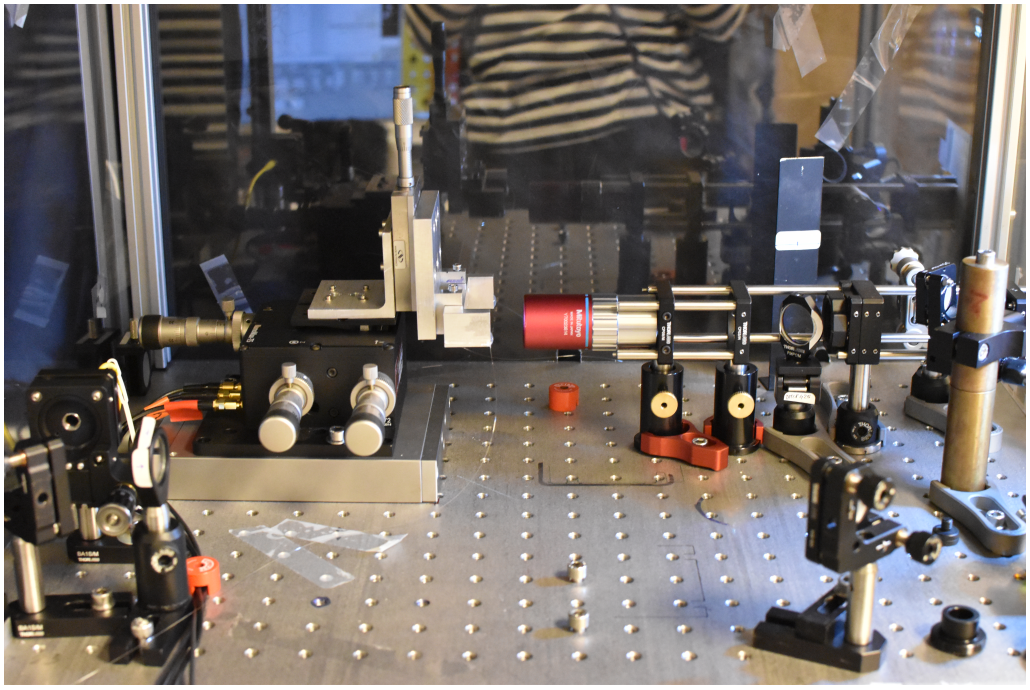

(a)

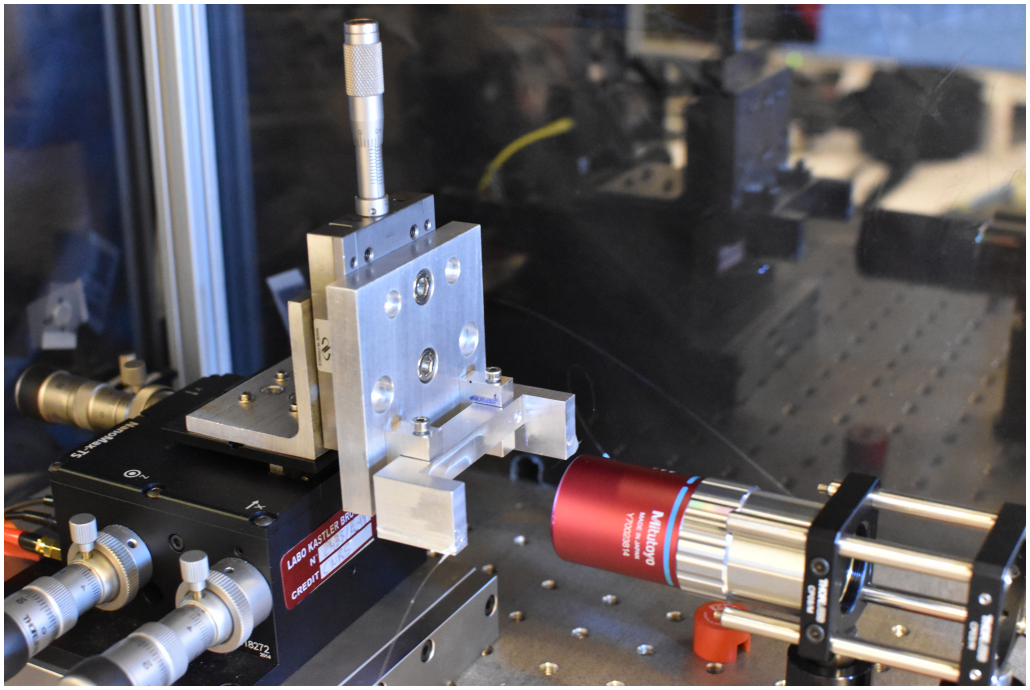

(b)

Figure 3.15 – Photo of the experimental setup for observing single photon emitters on the nanofiber from different prospective. The U-support to which the fiber is glued is visible.

3.5 Nanocrystal deposition and antibunching measurement on the nanofiber

The coupling of the light emitted by the nanocrystals with the modes of the fiber happens via the strong evanescent field present at the nanofiber surface. This technique has been used in the past to couple with nanofibers different emitters, such as single atoms[88, 89], nanodiamonds containing NV centers[90, 91] and CdS/CdSe colloidal quantum dots[92, 11]. However, to the best of our knowledge no references about perovskite nanocrystals coupling with nanofibers nor with other integrated photonic structures are available in literature. The poor photostability of these emitters made indeed particularly challenging the integration with this kind of structures. Different techniques to place the emitters in the proximity of the nanofiber have been used. In case of atoms, this is obtained placing the nanofiber under vacuum and trapping atoms near it using optical trapping. Differently, in case of solid emitters, deterministic deposition can be achieved using and AFM tip to place the emitter at the desired position making use of another nanofiber to deposit the emitter. In the case of our perovskites, we decided to use a technique for non-deterministic deposition consisting in touching the fiber with a droplet of solution containing the nanocrystals. Compared to more complex techniques, this method, detailed in the following, allows a faster and simpler deposition, important in case of fragile emitters. When further optimization of perovskites stability will be performed, the other techniques could be applied to deterministically place them on the fiber.

To deposit the nanocrystals on a nanofiber, we first take a droplet of 20 µL with the solution containing the nanocrystals with a micropipette. Then, with the droplet at the extremity of the micropipette, we move the droplet towards the fiber until we touch it, leaving some nanocrystals over the fiber. In order to make a sturdy movement, we use a 3-axis translation stage to control the position of the micro-pipette. The scheme of the procedure is shown in figure 3.16.

We monitor the procedure with the microscope objective shown in figure 3.14. Once the droplet is in contact with the fiber, we gently move the droplet away from it. This procedure often results in one or more emitters deposited over the fiber. This can easily be verified by shining the excitation laser inside the fiber and filtering out the excitation beam to collect only the perovskite nanocube emission wavelength. Figure 3.17 shows how we can verify when we deposit the emitter over the nanofiber. During the procedure a laser is shined trough the fiber. First of all, we see the fiber, thanks to the light diffused by small imperfections on the nanofiber surface, and the approaching droplet

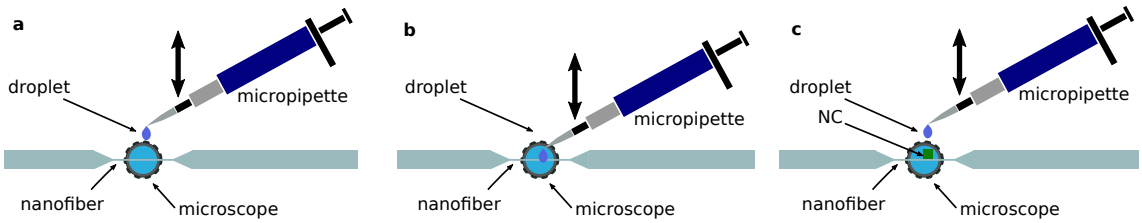

Figure 3.16 – Scheme of the procedure for deposition of single nanocrystals over a nanofiber. A droplet of 20 µL is created (a), and the fiber is touched with it (b) using a precise translation stage. The droplet is removed and this results in one or more NCs deposited on the fiber (c).

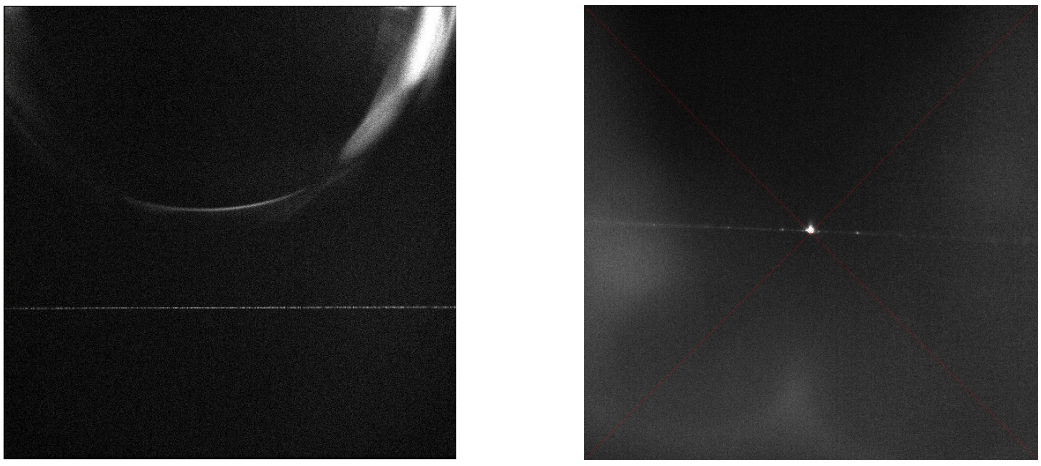

(a) (b)

Figure 3.17 – Image of the nanofiber detected from the camera. A laser is shined trough the fiber. (a) Before the deposition, the nanofiber is visible on the camera thanks to the weak diffused light from small imperfections at on the nanofiber surface; (b) after the nanoparticle deposition, the nanocrystals scatter light and they are visible as a strong bright spot on the fiber viewed by the camera. Both of the images were taken without filtering the excitation light.

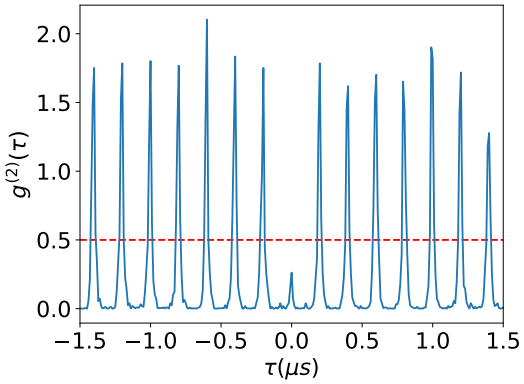

Figure 3.18 – $g^{(2)}$ function of a single perovskite nanocrystal placed onto a nanofiber: the photons are emitted directly throw the nanofiber and collected via the fiber output. We obtain a $g^{(2)}(0) = 0.24$.

(both of them visible in figure 3.17a). At the end of the procedure, an emitter is stuck to the nanofiber and scatters light resulting in a bright spot on the camera (as shown in figure 3.17b).

In order to deposit the emitters sufficiently spaced from one to another, we need to reduce the nanocrystal concentration. To do this, we were forced to dilute the initial solution by 100 times. As I have shown in section 2.4.2, this results in perovskites that bleach in a very short time: this means we have to illuminate the emitters for very short times and we cannot perform long statistical measurements.

We illuminate the nanocrystals via the nanofiber in order to find them and place them under the laser light coming from the microscope objective. We then use the fiber to collect the photons, sending the collected light to the antibunching setup and use the laser through the microscope objective to excite the emitter.

Even by having a short measurement time, we were able to measure a good single photon emission from the signal collected via the nanofiber. The result of this measurement is shown in figure 3.18. With this proof of principle measurement we demonstrate the possibility to couple a single perovskite nanocrystal with a tapered nanofiber. In order to perform a deeper study on this hybrid photonic device, a strong effort needs to be done to improve the nanocrystal stability to be able to use them for a long time after having reached the correct dilution.

Conclusions

- Fiber optics allow to guide light in very efficient way.
- I have reported a brief introduction on the fiber development and the theory of the light propagation in fibers.
- Depending on the fiber V parameter, the fiber can allow either the propagation of one single mode or of several modes, which propagate with different group velocities.
- When the fiber diameter is smaller than the wavelength of the guided light, it propagates mostly outside the fiber: it is the case for a so-called nanofiber.
- It is possible to fabricate an optical nanofiber by tapering a standard optical fiber.
- It is important to have an accurate control on the transition region between the standard fiber and the nanofiber in order to reduce the losses.
- It is possible to use the evanescent field to directly excite a nanocrystal that is placed on a nanofiber and vice-versa, to collect the light emitted by the nanocrystal via the nanofiber.
- I have shown that it is possible to couple the single photon emission of a perovskite nanocrystal directly inside the nanofiber

Chapter 4

Outlook and future perspectives

Contents

4.1 Introduction 105
4.2 Perovskite optimization 106
4.3 Single defects in nanodiamonds 106
4.3.1 Nitrogen-Vacancy color centers 107
4.3.2 Silicon-Vacancy color centers 108
4.4 Ion-exchange glass waveguides 111
4.4.1 Deterministic positioning of emitters on top of a waveguide . 112
Single waveguide dose characterization 114
Fluorescence emission spectra 114
Double waveguiding behavior 116

4.1 Introduction

Despite the versatility of the nanofiber platform integrated with perovskite nanocrystals there are some limitations that need to be overcome in order to be able to practically use it. In this chapter I will discuss some possible paths to address the main problems of this platform, keeping in mind the final goal: to produce integrated single photons sources for quantum applications. First of all, I will concentrate on the emitters, describing how perovskites nanocrystals could be improved and presenting also different kinds of emitters that could solve the main limitations of perovskites in the future, such as single defects in nanodiamonds.

In the second part of the chapter, I will describe another integrated platform I had the opportunity to work with, that could improve the nanofiber limitations, mainly its

fragility, while keeping its advantages: this platform is the Ion-exchange glass waveguide platform.

4.2 Perovskite optimization

Perovskite nanocrystals have shown to be high quality emitters, with a narrow emission at room temperature and easy fabrication method. The versatility of the chemical structure is so wide that almost any interesting wavelength can be reached: at the moment, emission in visible and near infrared ranges has been shown.

In addition, recent studies on perovkite nanoplatelets have shown that the emission wavelength depends on the number of layers: with the improvement of the growth techniques, this can be an advantage to produce several identical emitters [93, 94, 69].

The main drawback of perovskite nanocrystals is their photo-stability: this is the direction on which it is important to focus the research to start with. Our study [95] has shown that one of the factors is the role of the ligands. That is actually not completely understood but that could offer in the near future the key to obtain stable perovskite nanocrystals.

A recent study in this direction has demonstrated that it is possible to stabilize nanocrystals replacing the oleic acid with a more appropriate ligand, the 2-hexyldecanoic acid [96]. That could be the way out for such emitters.

4.3 Single defects in nanodiamonds

Defects in diamonds are interesting sources of single photons, as they are very stable.

Crystallographic defects in diamonds results from crystal irregularities, as well as from substitution or interstitial impurities. When present in huge quantity, they have effects in the crystal color and electrical conductivity. In jewelry, they are used to produce colored diamonds. More than 100 luminescent defects are known in diamond, and a large part of them has been studied in detail [97]. Diamond luminescent defects are of great interest for single photon generation, due to their great stability. During my PhD, I studied two different single-photon emitting defects in diamonds, Nitrogen-Vancancy and Silicon-Vacancy, whose main characteristics are detailed below. At L2n laboratory, Germanium-Vacancy color centers are also currently studied [98], but I did not have the opportunity to work with them and, for this reason, I will not treat them here.

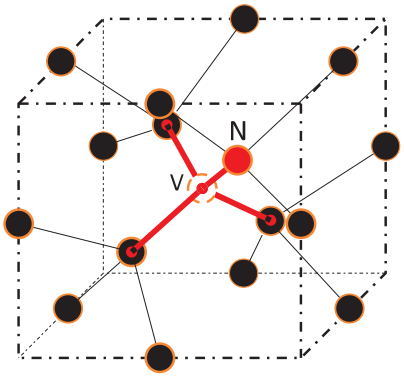

Figure 4.1 – Representation of an NV center defect in a diamond crystal. *(credits: Trupke et al. [99]).*

4.3.1 Nitrogen-Vacancy color centers

One of the most important defects in diamonds for quantum photonics is the Nitrogen-Vacancy/NV defect. It is very abundant due to the presence of nitrogen in atmosphere which makes it highly probable to find them even in a clean production environment.

The structure of NV defect is reported in figure 4.1. This defect is present in both the neutral NV^0 state and in the charged state NV^-. I focused in my thesis on the NV^- defect which is the most studied for single-photon generation as its fluorescence is easy to detect, compared to the neutral one. As other defects in diamonds, the NV^- does not present stability issues so much. A very strong laser illumination can transform a NV^- center in a NV^0 one, but this problem is not present with standard excitation power. As opposed to perovskite quantum dots, NV^- nanodiamonds have a broad spectrum at room temperature, due to the thermal broadening, i. e. due to coupling with phonons from the diamond crystal structure. As an example, a spectrum of a NV^- defects in a nanodiamond is reported in figure 4.2a, while in figure 4.2b is sketched the level diagram with a focus on the emission wavelengths. The setup used to measure the spectrum is the same as described for perovskites at page 46, using a 532 nm continuous wave laser and appropriate dichroic and long-pass filters. Here, it is interesting to note that the usual excitation, out of resonance and typically with a wavelength of 532 nm does not mix the spin states $|0\rangle$ and $|\pm1\rangle$. In addition the non radiative decay rate from $\left|^3E, 0\right\rangle$ to $\left|^1A_1, 0\right\rangle$ is much lower than the one from $\left|^3E, \pm1\right\rangle$: as a result, by exciting repeatedly the emitter, it is possible to bring the spin of the NV center to the $m_s = 0$ level; such phenomenon is called spin polarization [100] and allows to easily reset the spin state for applications that use the spin to encode the qubit [101, 102]. At cryogenic temperatures, most of the emission is in the zero-phonon-line and the linewidth is reduced to a width

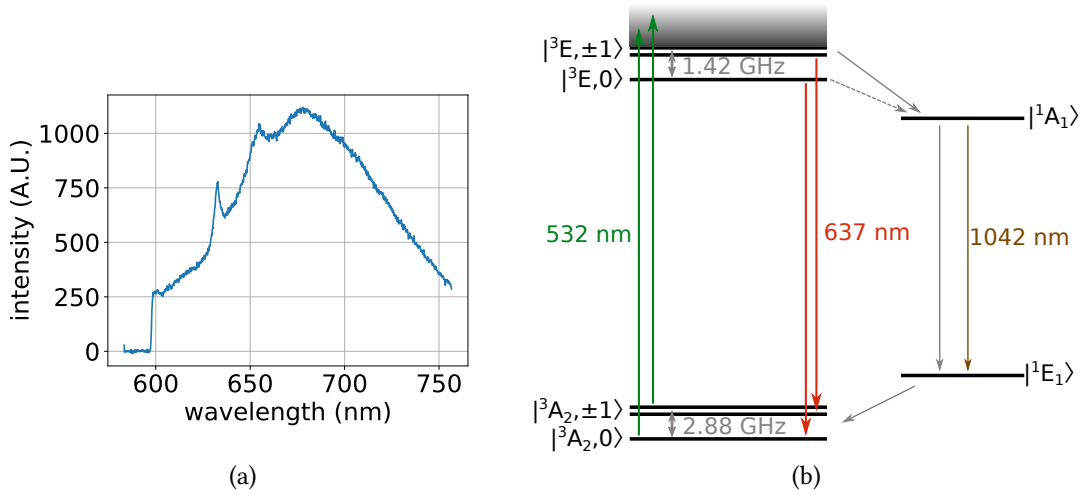

Figure 4.2 – (a) Fluorescence emission of a single NV center in a nanodiamond. The fluorescence is cut by a 600 nm long-pass filter. The first peak on the left, at about 634 nm is the zero phonon line: in single defects in bulk it is at 637 nm but reticular strains can slightly modify its wavelength. (b) Level structure of an NV defect. The green line represent the usual excitation light (out of resonance), while the red represent the emission wavelength. The gray lines represents non-radiative relaxation process.

of few megahertz.

In conclusion, NV^- color centers in diamond are interesting sources of single photons that show, with respect to the perovskite nanocrystals, the advantage of the stability and the possibility to control and use their spin state. The main limitation is that the broad spectrum makes it difficult to obtain two photons at the same frequency at room temperature. The coupling of NV^- nanodiamonds with nanofibers have been successfully achieved by different groups both at room and at cryogenic temperatures [92, 91, 90].

4.3.2 Silicon-Vacancy color centers

Less abundant than the NV^- color centers, the silicon-vacancy defects are gaining interest as single photon emitters: indeed, they have most of their emission in the zero phonon line even at room temperature [105, 106]. The structure of this defect is more symmetrical, as the Si atom is in between the places left by the two missing carbon atoms as shown in figure 4.3a. Its spectrum is shown in figure 4.3b.

The fluorescence wavelength of the zero phonon line is in the near-infrared range, at about 737 nm and at room temperature 70 % of the light is emitted in it [105, 107]. This is a very large amount if compared with other kind of nanodiamonds. In figure 4.4 the energy levels of an SiV color defect are shown, as well as a low-temperature zero

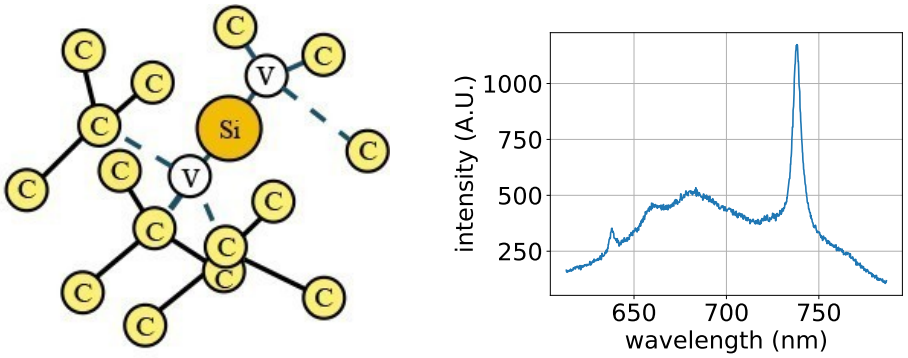

(a) (b)

Figure 4.3 – (a) Structure of a SiV color center in a nanodiamond. The Si atom is in between two vacancies.*(credits: Zeleneev* et al. *[103])*. (b) Measured emission of SiV defects in a nanodiamond at 737 nm. It is clearly visible that the emission of NV defect is also present with the SiV emission.

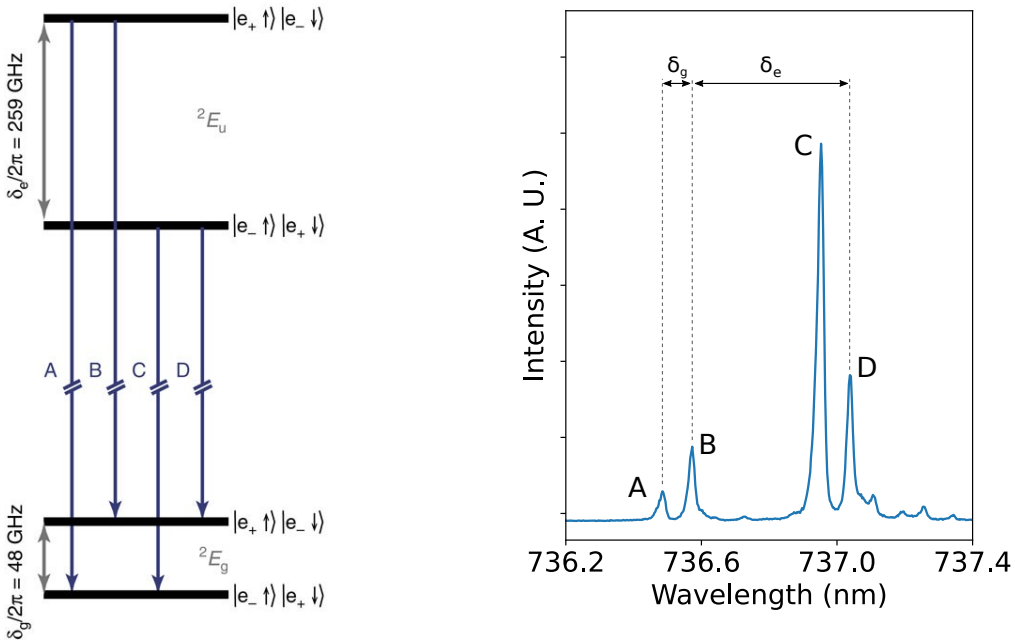

(a) (b)

Figure 4.4 – (a) Energy levels of an SiV color defect in diamond *(credits: Becker* et al. *[104])* and (b) emission spectrum at 4 K of the zero phonon line transition of the SiV color defect *(measured by M. Nahra at L2n)*.

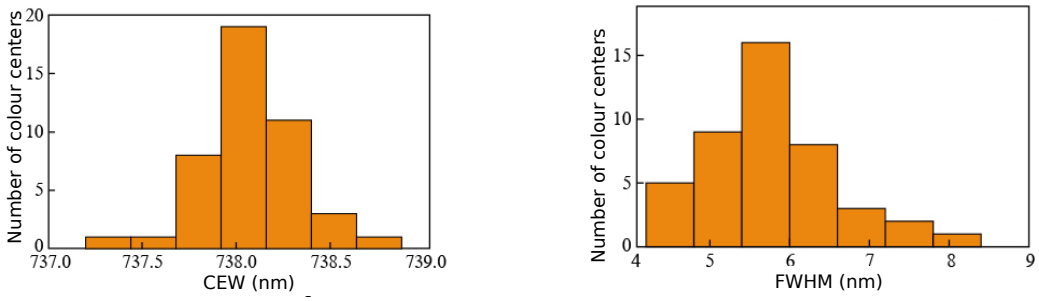

Figure 4.5 – Characteristics of SiV nanodiamonds obtained by Zeleneev *et al.* [103] (a) Central emission wavelength of the peak (CEW) at room temperature (b) Full width at half-maximum of the peak at room temperature.*(credits: Zeleneev* et al. *[103]).*

phonon line emission: four transitions are present, all of them are included in the larger emission obtained at room-temperature [104] (figure 4.3b).

As the silicon is less abundant with respect to nitrogen, this kind of defect is naturally less abundant, it is thus more difficult to fabricate nanodiamonds with a single SiV center and without any other defect. One interesting way to produce high quality nanodiamonds containing SiV color centers is to create them directly in nanodiamond form, avoiding mechanisms that can induce reticular strain inside them: this is of importance as the reticular strain can affect the emission spectrum; the absence of reticular strains is indeed the main advantage of the direct fabrication of nanodiamonds with respect to the method based on nanodiamond explosion [108, 109]. Recently, a fabrication procedure to obtain single high-quality nanodiamonds with a size of few nanometers has been described by Zeleneev *et al.* [103]: with this fabrication technique the authors obtained the remarkable wavelength distribution and full width at half maximum of the fluorescence peak shown in figure 4.5. This results show that these emitters are good candidates for future integration on nanofibers: we started for this reason a collaboration with Prof. Viatcheslav Agafonov from the university of Tours in order to study the application of his nanodiamonds in our platform.

In the test we made, it was not possible to integrate them, as the first samples were not small enough and contained, together with SiV color centers, also some NV color centers, as clearly visible in the spectrum reported in figure 4.3b. Recent improvements within the fabrication shown in Zeleneev *et al.* [103] seems to point towards solving this issue. The spectrum observed is shown in figure 4.6.

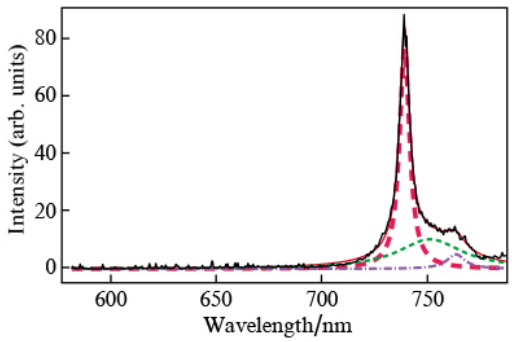

Figure 4.6 – Typical spectrum of SiV color center fluorescence from a nanodiamond fabricated via the procedure described in Zeleneev *et al.* [103]. The red dashed line represents the fit of the zero phonon line with a sum of three Lorenz functions, while the others represent the fit of the phonon wings. *(credits: Zeleneev* et al. *[103]).*

4.4 Ion-exchange glass waveguides

The ion-exchange glass waveguide ion-exchange glass waveguide is an alternative platform that can overcome some fragility problem of nanofibers, while keeping most of their advantages. In order to produce an ion-exchange glass waveguide, an appropriate amount of Ag^+ ions are diffused in glass, creating a gradient in the refracting index that can weakly guide the light [110]. A representation of this kind of waveguide is reported in figure 4.7. By using simple thermal diffusion, the Ag^+ ions diffuse inside the glass: their concentration is smaller the farthest we go from the glass surface towards the inner region of the guide, creating a gradient of concentration (and consequently of the refraction index) that is indicated in red in the image. A mask is used to ensure the ions diffuse only in the desired region; it can be a metallic mask (made of titanium or aluminum), or, better [111, 112], a dielectric mask (aluminum oxide or silicon oxide). The guide can then be left in place (this was the case for the guides I used) or can be moved deeper in the glass by applying an electrical field. These guides are produced by the company TeemPhotonics in Meylan as part of an on-going collaboration between the L2n-UTT and TeemPhotonics for many years now. By using the near field interaction, as explained for the nanofibers in the same way, it is possible to couple light from emitters deposited over the waveguide directly inside it. However, as opposed to the nanofiber, the near field of an Ion-exchange glass waveguide is weak and the guided mode is mostly contained inside the guide. As a solution to this problem, it has been proposed to use a TiO_2 layer in order to "pull" the mode outside the waveguide and use it to couple the emitters [113]. Simulations and experiments conducted at the L2n-UTT by Josslyn Beltram-Madrigal showed that this mechanism works well [113].

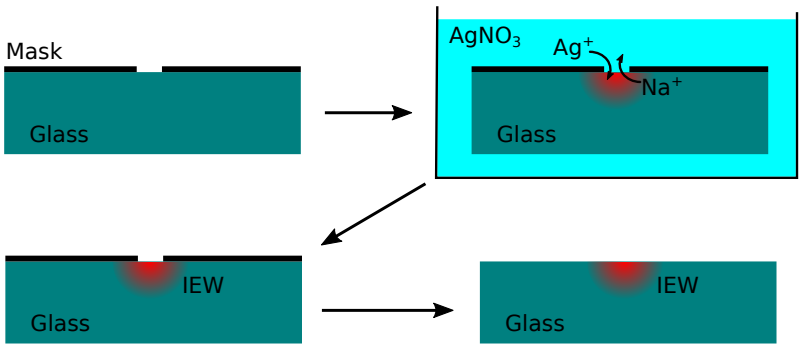

Figure 4.7 – Fabrication procedure of Ion-exchange glass waveguide: first of all, a mask is created on the surface of a glass plate; then the glass is immersed in a solution containing Ag^+ ions, as for example a solution of $AgNO_3$. Some of the Ag^+ ions replace some of the Na^+ of the glass, modifying its refraction index. Eventually the support is extracted and the mask is removed.

4.4.1 Deterministic positioning of emitters on top of a waveguide

The deposition procedure described for the nanofibers is not applicable to the waveguides, as the support is now two-dimensional and an emitter could get stuck far from the guide: we need a different way to deposit the emitters on the waveguides. The most simple one is to spin-coat a given amount of solution containing the emitters, hoping that some of them will be in the right place over the guide; however this method is completely non-deterministic and it is completely based on randomness. For this reason, it is not adequate for more complex experiments, like the ones involving creating plasmonic antennas over the guide. A more deterministic approach can consist in positioning the emitter at the right place by using an AFM tip: this approach allows a fine control of the position of the nanoemitter [114] but requires time and is difficult to imagine a possible integration for industry processes. An alternative promising approach to address this problem is the one we proposed in the work with Lio *et al.* [115]: the idea is to use a polymer to encapsulate the emitters at the desired place. Photopolymerization is a process in which a polymerization reaction is induced by light: the region of the liquid irradiated by light reacts and changes state becoming solid, while the non-illuminated regions remain in the liquid state and can be washed out by using the appropriate solvent. If the emitters are dispersed in the polymer, there is a significant probability that one (or more) of them will be trapped in the solidified part, while all the others will be eliminated during the washing procedure. As any light-induced process, usually the smallest size reachable is diffraction limited. However different techniques can be used to overcome this limit, as for example by using two photon polymerization techniques[116, 117]. One of the most

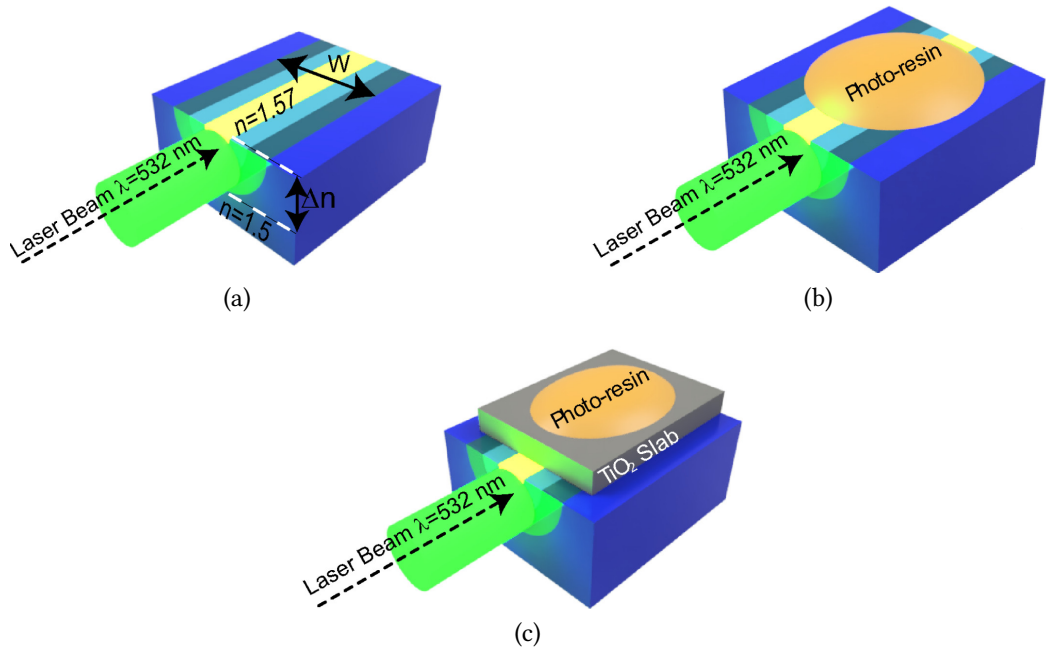

Figure 4.8 – (a) The Ion-exchange glass waveguide studied, the refraction index changes from 1.5 in the blue region (glass substrate) to 1.57 in the inner zone of the guide, represented in yellow. The green cylinder represents the curing laser used to obtain the photopolymerization reaction. In the first configuration considered (b) the photo-resin is directly placed over the Ion-exchange glass waveguide. In the other, (c) the waveguide is firstly covered by a TiO_2 layer in order to create a double dielectric waveguide and increase the near field coupling. The resin is placed over the TiO_2 layer. *(credits: Lio et al. [115]).*

promising techniques that was recently investigated is polymerization by evanescent waves polymerization by evanescent waves[118, 119].

This technique consists in using the near field of the guided mode of the waveguide to induce the polymerization of the photo-resin. This method allows obtaining a layer of the polymer with a thickness of few nanometers, trapping in the contained quantum dots/emitters on the waveguide surface. We performed the experiment in two different configurations showed in figure 4.8: in one case we deposit the photo-resin directly over the waveguide, while in the other case, we deposit the photo-resin over a TiO_2 layer present on top of the guide. As explained before, the TiO_2 layer has the effect of creating a double dielectric waveguide and increases the intensity of the near field compare to having the Ion-exchange glass waveguide alone.

In the experiment, we used two different resins: one containing CdSe/ZnS nanocrystals while the other not. The details on the composition are reported in table 4.1.

resin 1	**resin 2**
pentaerythritol triacrylate (PTEA) 4 % methyl diethanolamine (MDEA) 0.5 % eosin Y	pentaerythritol triacrylate 4 % methyl diethanolamine 0.5 % eosin Y 1 % CdSe/ZnS nanocrystals

Table 4.1 – Composition of photoresins used in the experiment: both of them are based on pentaerythritol triacrylate (PETA) with the addition of other components (the percentage indicates the molar concentration). The second resin contained the nanocrystals.

Single waveguide dose characterization

The first interesting experiment to perform to develop this technique is to characterize the minimal dose needed to polymerize the resin. A standard time of 60 s was used to cure the resin with different laser powers. The characterization of the thickness of the polymer layer deposited over the waveguide was performed using an atomic force microscope (AFM). It Was found that the minimal power to trigger the photopolymerization process was 0.56 mW for the resin without the quantum dots/nanocrystals and 0.70 mW for the resin containing the quantum dots. This difference can be explained by the greater absorption of the mixed resin due to the quantum dots. Once we defined the minimal threshold, it is interesting to have information on how the thickness evolves by increasing the energy: this was studied using an exposure time five times longer for each polymer. The AFM images and their section profiles are shown in figure 4.9. The obtained thicknesses are as low as (18 ± 2) nm in case of resin 1 and (24 ± 2) nm in case of resin 2. These values are of the same order of the diameter of the involved nanoemitters, which is about 12 nm. This type of thin film containing nanoemitters (in this case nanocrystals) could be used in the future to obtain deterministic positioning of nanoemitters on plasmonic nanostructures.

An interesting application of near-field two-photons induced polarization has been developed in our group by Ge *et al.* [120] with the development of a single-photon switchable hybrid nano-emitter. The near-field is used to polymerize a photo-resin containing quantum-dots near a gold nanocube, obtaining a single photon-emitter with an excitation efficiency strongly dependent of the polarization of the excitation light.

Fluorescence emission spectra

The emission spectra were measured with an home-made confocal microscope at the L2n-UTT, similar to the one used for the measurements of the perovskite optical properties. The emitters were excited with a blue laser ($\lambda = 405$ nm) which was removed

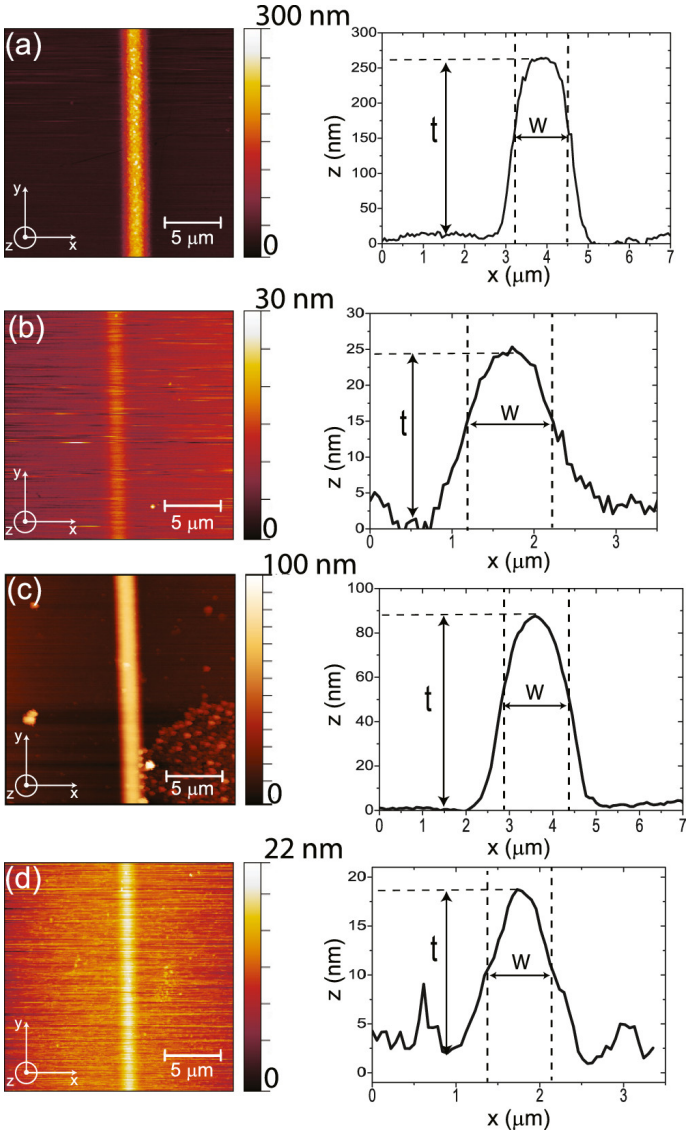

Figure 4.9 – On the left hand-side, AFM images of photopolymerized resins. On the right hand-side the profile of the polymer section. (a) and (b) are obtained using the resin without the nanocrystals, respectively with a power of 0.56 mW and an exposure time $t_e = 300$ s and $t_e = 60$ s; (c) and (d) are obtained using the resin with the nanocrystals, respectively with a power of 0.70 mW and an exposure time $t_e = 300$ s and $t_e = 60$ s. In presence of nanocrystals the power is higher due to the greater absorption of the polymer. *(credits: Lio* et al. *[115]).*

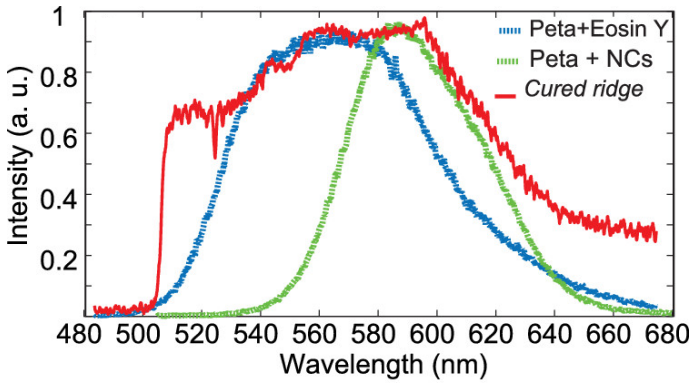

Figure 4.10 – In red, emission spectrum of the fluorescence of the photopolymerized ridge on the Ion-exchange glass waveguide. In blue, emission spectrum of the fluorescence of PETA + 0.5 % eosin Y while in green, we have the fluorescence of a drop of PETA containing the nanocrystals used in the experiment. *(credits: Lio* et al. *[115]).*

from the detected light with a long-pass filter with a cutoff wavelength of 500 nm. The result is shown in figure 4.10 where the blue and the green curves represent respectively the emission of the two drops of PETA + 0.5 % eosin Y and PETA +NCs. The red one is the emission of the cured polymer. It is possible to see that the red curve is the composition of the two others, as expected. The first part of the red curve, that has not a correspondence in the other two, is due to Methyl diethanolamine (MDEA) emission, the central part is due to the PETA + 0.5 % eosin Y component while the part at higher wavelengths is due to the nanocrystals.

Double waveguiding behavior

As already mentioned before, adding a TiO_2 layer over the Ion-exchange glass waveguide has the effect to create a double dielectric waveguide: the light is now guided by both waveguides. A thickness of 85 nm was chosen for the TiO_2 layer as it allows an optimal working range for the visible light (from 400 nm to 800 nm) where the guide is a single mode one in this range.

The procedure to photopolymerize the resin is similar to what was described before, with the only difference that, in this case, it is not spin-coated directly on the glass but on the TiO_2 layer. Only resin 2 (the one with nanocrystals) was used for this experiment and we chose to use an exposure time $t_e = 300$ s and an input power of 0.7 mW (the same values used in the case of a single waveguide). The result is shown in figure 4.11.

What is new here, is that the polymer presents a periodic modulation clearly visible in the AFM measurements (figure 4.11b). We can explain this modulation as an effect of

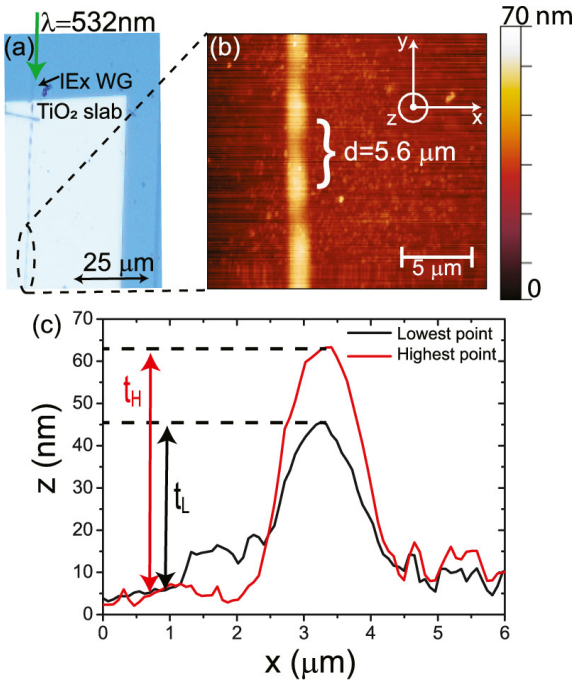

Figure 4.11 – (a) Image of the sample, where the TiO_2 slab is present, (b) obtained atomic force microscope image, showing a modulation of the thickness of the resin with a periodicity of 5.6 µm; (c) profile of the fabricated ridge; the red one is taken where the thickness of the ridge is maximal, while the dark one was taken were the thickness of the ridge is minimal. *(credits: Lio* et al. *[115]).*

a modulation of the near field intensity during the curing of the resin: this modulation is due to a periodical beating between the two waveguides. The beats is present between the Ion-exchange glass waveguide and the TiO_2 layer.

This beating was observed also in previous experiments, performed in our lab by Beltran Madrigal *et al.* [113], in which a SNOM analysis on a double waveguide was performed with the goal of measuring the evanescent field present during the light propagation in the double waveguide. The results of the simulations with a finite element method validated this hypothesis [115].

Conclusions

In this chapter I presented an insight of possible options and different approaches that can improve in the near future our system. From the emitters side:

- I explained the potential improvements that are possible with perovskite nanocrystals;
- I showed the potential improvements that the study of defects in nanodiamonds can offer in general;
- I detailed the main properties and advantages of the two kinds of single defects in nanodiamonds I studied during my PhD.

From the photonic platform side, I presented a promising alternative approach, the Ion-exchange glass waveguide platform.

- The Ion-exchange glass waveguide has the potential to be more stable with respect to the nanofiber, as it is more robust and less affected by dust,
- I detailed the methods of nanoemitters deposition and differences with respect to the nanofiber case.
- I detailed the results of an original study in which I was involved in order to use photo-polymerization as a strategy of deposition of quantum dots over a waveguide.

Conclusions

In this manuscript I presented the results obtained during my PhD thesis as well as the theory required to understand them.

Regarding perovskite nanocrystals, I explained their properties and their main limitation, that is the stability under laser excitation. This limitation, due to the degradation under moisture and light, can be reduced with different approaches:

- It is possible to protect the emitters using a polymer. This technique allows an improvement on the stability: our measurements show that, using a polymer, the degradation happens in a time-scale four time larger. However, this approach is not suitable for depositing emitters on the nanofiber, which was my final goal during my thesis.

- The preparation of the emitters plays an important role for their stability: with a slight different preparation process we were able to obtain emitters whose stability can be measured in hours instead than in minutes.

I have shown, in addition, the role of the dilution in the stability. This is important for applications that need a diluted solution, but is also an indication of the role of ligands in the stability. This can opens new research paths to increase the stability of these perovskites.

The performed measurements showed that our perovskites are not only more stable from an emission point of view, but also the spectra stability is increased, with a drift of the spectrum less than 20 nm in more than two hours.

The increased stability allowed to study the blinking properties of our emitters: in particular the analysis of the fluorescence-lifetime intensity distributions had shown that our emitters stay in an excited state for the most of the time.

Thanks to the improvement on fabrication it was possible to couple single photons emitted by the nanocrystals with a tapered nanofiber. Tapered nanofiber are obtained by pulling a standard optical fiber over a pure flame of hydrogen and oxygen: in this way it

is possible to adiabatically change the the taper profile in order to couple almost all the light coming from fiber in the nanofiber and vice-versa, by obtaining a nearly unitary transmission that can be over 98 %. In the nanofiber part, a strong near-field is present around the fiber: this allows to couple the light from a single photon emitter deposited on the nanofiber directly inside it. This was demonstrated by performing an antibunching measurement on the photons collected at the output of the nanofiber. Such measurement showed a $g^{(2)}(0) = 0.24$, proving the presence of single photons in the nanofiber.

In addition, I also had the possibility to work on a different platform, that can in future be used instead of nanofibers: the ion-exchange glass waveguide platform. In particular we have shown a technique for nanocrystal deposition on waveguides. We dispersed the emitters in a photo-resin, and we used a two photon polymerization technique in order to deposit on the glass waveguide a few nanometers thick ridge of resin containing the emitters. With future developments this technique, combined with plasmonic nanoantennas, could bring to deterministic positioning of colloidal quantum dots on the waveguide.

The work accomplished in this thesis gave origin to three publications on peer-review journals and an invited oral presentation at the “Smart Nanomaterials, Advanced Innovations and Applications” international conference in Paris.

Appendix A

Analysis software for TTTR3 files

A.1 Introduction

During the time-tagged time resolved measurement (TTTR) used for the characterization of single photon emitters a large amount of data is produced. Indeed, any detected photon arrival is recorded with its arrival time and the channel where the event was detected. If we consider a standard $3 \cdot 10^4$ cps, we have more than $5 \cdot 10^7$ counts in half-an-hour of measurement. For this reasons data are stored in a binary format, that allow to save them in a file size smaller than the one allowed by a plain-text file. PicoQuant decided to give to this file the extension `.ptu` and to release demo codes in different programming languages in order to allow to access it. Among them I chose C++, as it presents two main advantages.

- It is a stable open source language, which ensures the availability of the written code for the lab and guarantees it will be usable in the future without the need of license.
- It is a compiled language which is faster to run on a computer.

This was a judicious choice as the computation of the $g^{(2)}$ is resource and time consuming.

In addition, C++ has a wide variety of tools to create stable graphic interfaces in order to make the program user friendly.

The first version of the program was a command line code generating the $g^{(2)}$ graph and writing the values in a file format readable with gnuplot. This approach was working, but in the long term the increased needs of analysis, and thus of options, made it not practical and its use quite complex. For this reason I wrote a second version of the

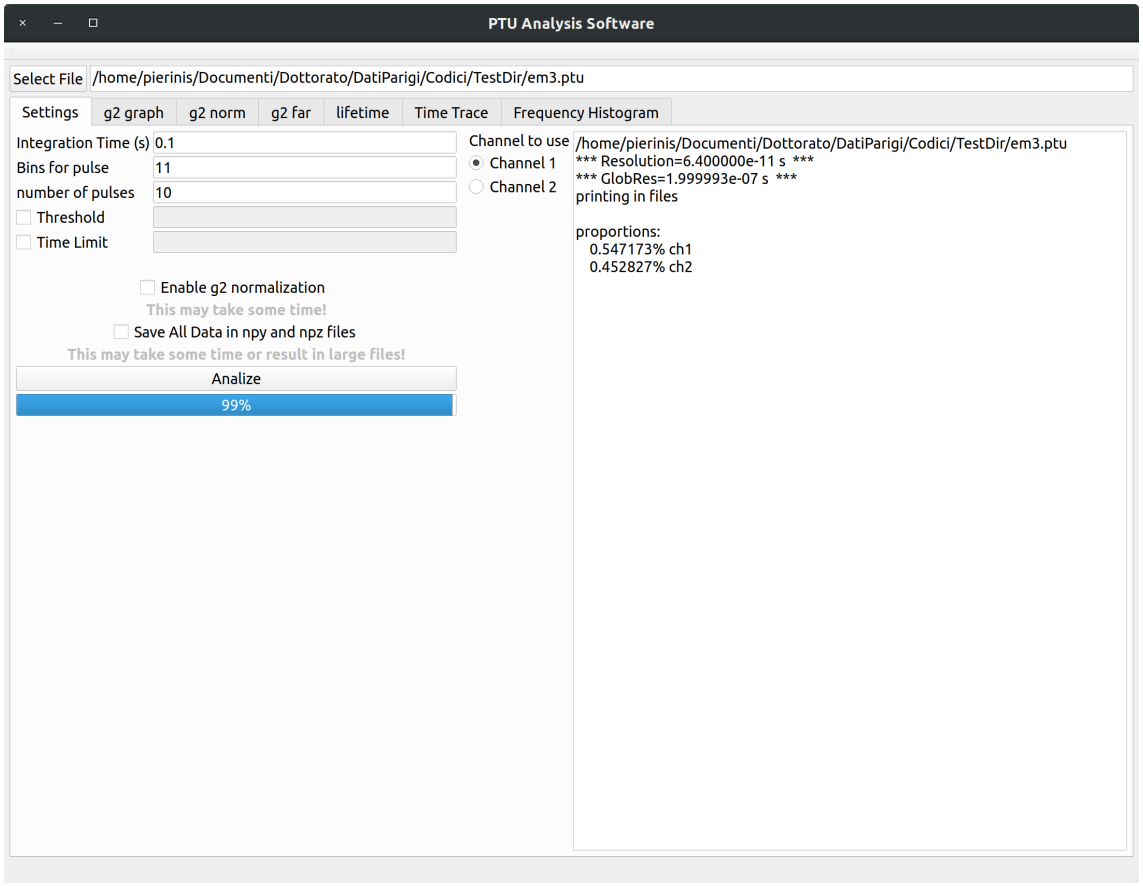

Figure A.1 – PTU Analysis Software: the main window that is opened when the program is started.

program, using C++alongside with Qt framework that allows the creation of a graphical interface. Here I will describe only the actual version of the software. However, in order to understand some choices, it can be useful to take in account that it has been written firstly for a command line use and then it has been adapted to the Qt framework to add a graphical user interface.

I this appendix I will describe the usage of the software, without entering in the details of the underlying code, then I will describe the tools I used to write it and the algorithms on which it is based.

A.2 The software usage

When the software is launched, appears the window reported in figure A.1. In the first line is possible to paste the path to the interested file, or alternatively to select the file using the *Select File* button. The name of the output files is automatically chosen by the

software using the original name and appending a specific suffix for each file, depending on the content. This line is visible in any page of the application. Multiple panels are available under it, the first one (*Settings*) is the one used to set the analysis parameters and perform the analysis while the others are used to display the analyzed data. In the following I will explain in detail these panels.

A.2.1 *Settings* panel

Multiple settings are available on the left of the panel to correctly perform the Analysis (see figure A.1). In the following their behavior and function are explained one by one.

- The *Integration Time (s)* line, contains, in seconds, the time used to create the time trace histogram and to possibly define the thresholds.
- The *Bin for Pulse* line contains the number of bins for each laser impulsion used in the $g^{(2)}$ histogram. In other words, if the laser sends a pulse every 200 ns and we set 11 bins for pulse, the bin size will be 200 ns/11. In this way, each laser impulsion contains exactly a entire number of bins, which reduces the artifacts in the histogram. In my experience, an odd number of bin per pulse is better than an even one, as in this case the maximum falls in the middle of the bin and not on the border of it.
- The *Threshold*, when set, introduces a threshold that the signal has to reach in order to consider the emitter "ON". In practice the time trace is traced, and only the photons arrived in bins that contains more than a certain number of counts are considered. This can be useful, if the emitter blinks between a bright and a gray state. Indeed it allows to analyse separately the bright state excluding the gray one.
- The *Time Limit* field, when set, introduce a time limit on the analysed signal. This is useful if we realize that the emitter died after a certain time and we know that after that time only noise has been recorded.
- Option *Enable* $g^{(2)}$ *normalization* is useful to normalize the $g^{(2)}$ histogram as explained in section 2.3.4. of chapter 2.
- The *Channel to use* settings ask which channel the user wants to use to calculate the TimeTrace and the lifetime histograms. The choice is between one of the two channels.

On the right of the panel, a non-editable text panel is available: here the processing details and some information on the analysis are written during the process. This is useful to know the progress status of the analysis. In addition, the last two lines printed on the right panel tell us which proportion of photons is arrived in each channel: this is very useful, as to efficiently measure the $g^{(2)}$ this must be the nearest possible to the 50 % in each channel. This can be seen with a simpler calculation: first of all, let $p(\Delta t)$ be the probability of getting a photon in a time interval of Δt, corresponding the the size of the bin in the $g^{(2)}$ histogram. Now, the probability to obtain it in the first channel will be $p_1(\Delta t)$ and the probability to obtain it in the second channel will be $p_2(\Delta t)$, and suppose it to be constant in any time interval with the same width. Now, we can say that the following equation is valid (for definition of $p(\Delta t)$):

$$p(\Delta t) = p_1(\Delta t) + p_2(\Delta t). \tag{A.1}$$

If now we define x as $p_1(\Delta t)/p(\Delta t)$ we can write:

$$p_1(\Delta t) = xp(\Delta t) \qquad \text{and} \qquad p_2(\Delta t) = xp(\Delta t). \tag{A.2}$$

The probability to register a coincidence event in the $g^{(2)}$ graph p_e will be given by to the product of p_1 and p_2 as it happens only when a photon is detected in each of the two channels. Thus we write:

$$\begin{aligned} p_e &= p_1(\Delta t)p_2(\Delta t) \\ p_e &= x(1-x)p^2(\Delta t) \end{aligned} \tag{A.3}$$

the last equation is the equation of a parabola, with a maximum on $x = 0.5$. Its graph is reported in figure A.2. Is interesting to note that when $0.4 \leq x \leq 0.6, p_e(x) \geq 0.96 p_e(0.5)$: in other words we can tolerate a slightly non-homogeneous distribution of the counts in the two channels conserving more than the 95 % of counts.

A.2.2 Visualization panels

Three different panels are available to visualize the $g^{(2)}$ histogram once the file has been analyzed. The first one (figure A.3a) reports the raw $g^{(2)}$ graph as it is measured by the instrument. Here is clearly visible, around $t = 0$ s, the effect of the dead time of the instrument described in chapter 2. In this graph the time axis refers to the delay in arrival of the signal to the instrument; we are instead interested in the delay in the

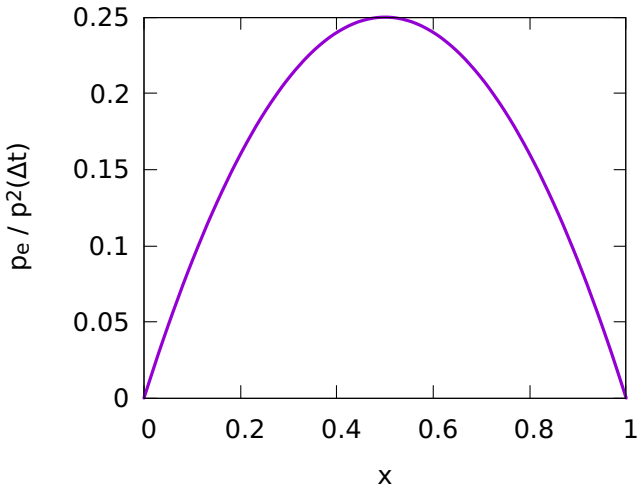

Figure A.2 – Graphical representation of the parabola in equation (A.2). The maximum is located in $x = 0.5$.

arrival of the photons in the APDs. These is calculated in the following panel, the $g^{(2)}$ *norm* panel, reported in figure A.3b. The first thing we note here is the presence of multiple text field. The first one, marked with *x_0*, is editable: here it is important to insert the length of the delay line, while the others are calculated by the program and cannot be modified. Once *x_0* value set, if the analysis has been performed with the *Enable* $g^{(2)}$ *normalization* option enabled, it is possible to click on the *plot it!* button to visualize the plot. This time, the zero delay is what we are looking for, while the dead time has been artificially removed to make the graph more readable. It it also important to note that the height of the last peaks is lower due to the fact that the last peak falls on the border of the chosen window: this is not a physical effect, and they not need to be considered in the analysis.

The panel $g^{(2)}$ *far* is shown in figure A.4a and reports the maximal values of the $g^{(2)}$ histogram at long delays. The graph is created only when the analysis is performed with the *Enable* $g^{(2)}$ *normalization*. These is useful in case of blinking studies.

In panel *lifetime* reported in figure A.4b is possible to plot the lifetime histogram on the selected channel. It is often useful to plot it in semi-log scale. For these purpose, the *y logscale* option can be selected.

In panel *Time Trace* reported in figure A.5a is possible to plot the intensity trace of the emitter along the measurement.

In panel *Frequency Histogram* panel reported in figure A.5b it is possible plot the frequencies histogram: it reports the occurrence of a certain value in the intensity trace.

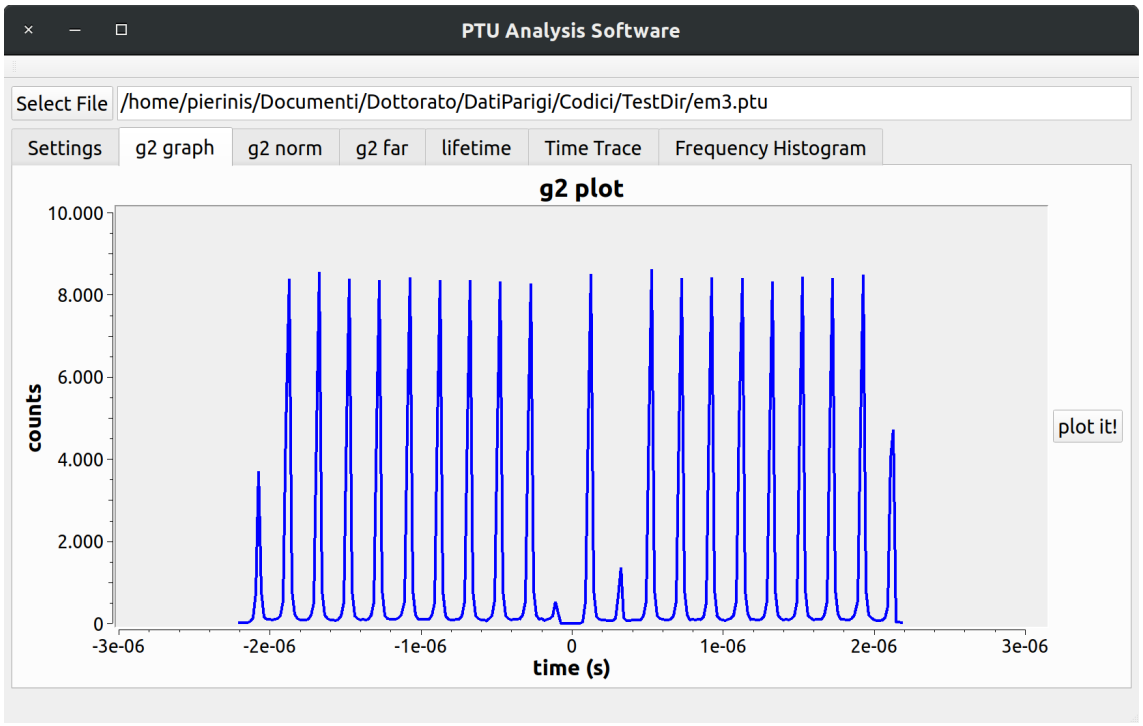

(a)

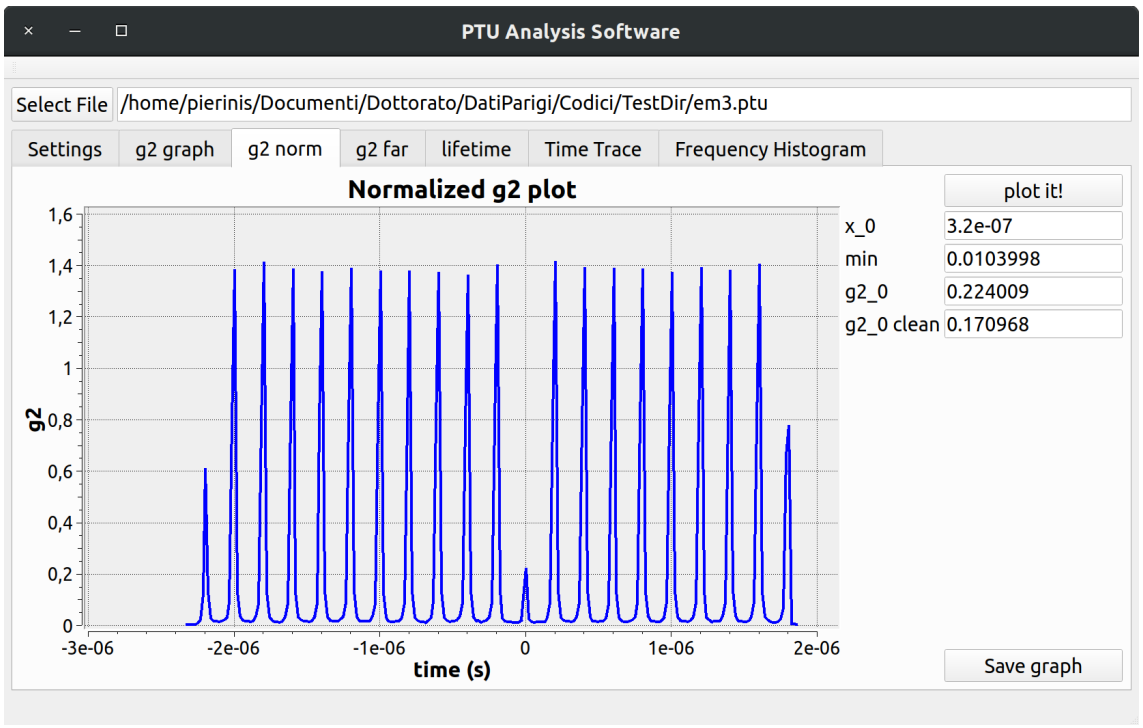

(b)

Figure A.3 – Example screenshot of $g^{(2)}$ *graph* A.3a and $g^{(2)}$ *norm* A.3b panels.

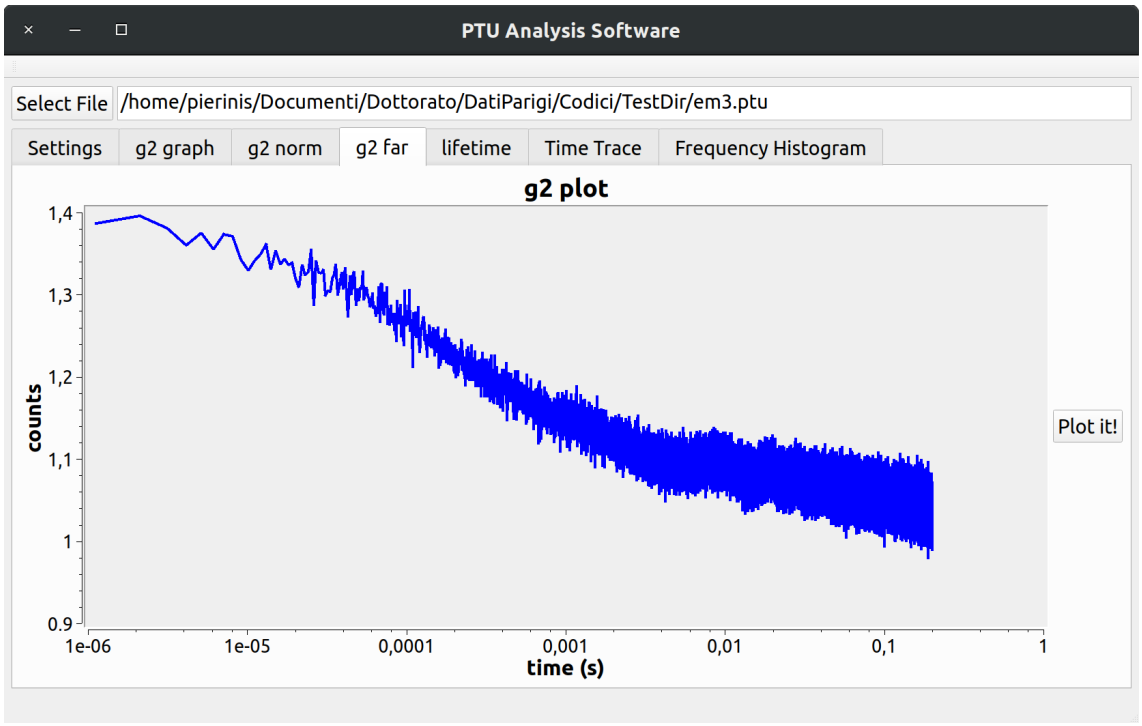

(a)

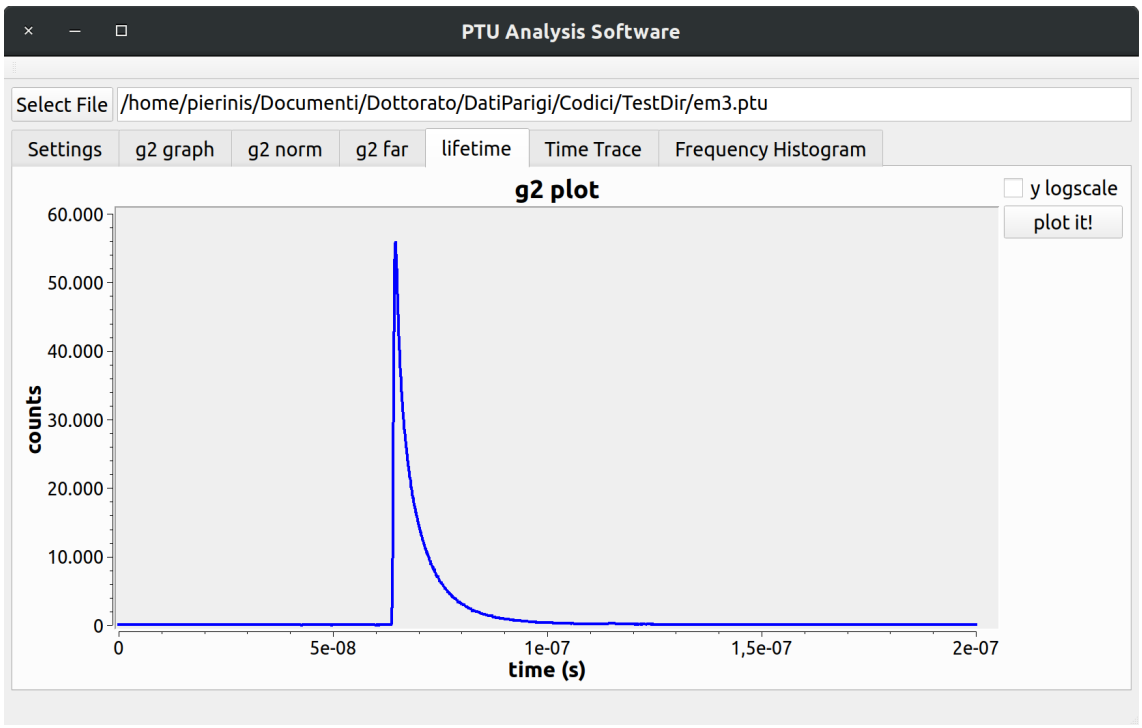

(b)

Figure A.4 – Example screenshot of $g^{(2)}$ *far* A.4a and *lifetime* A.4b panels.

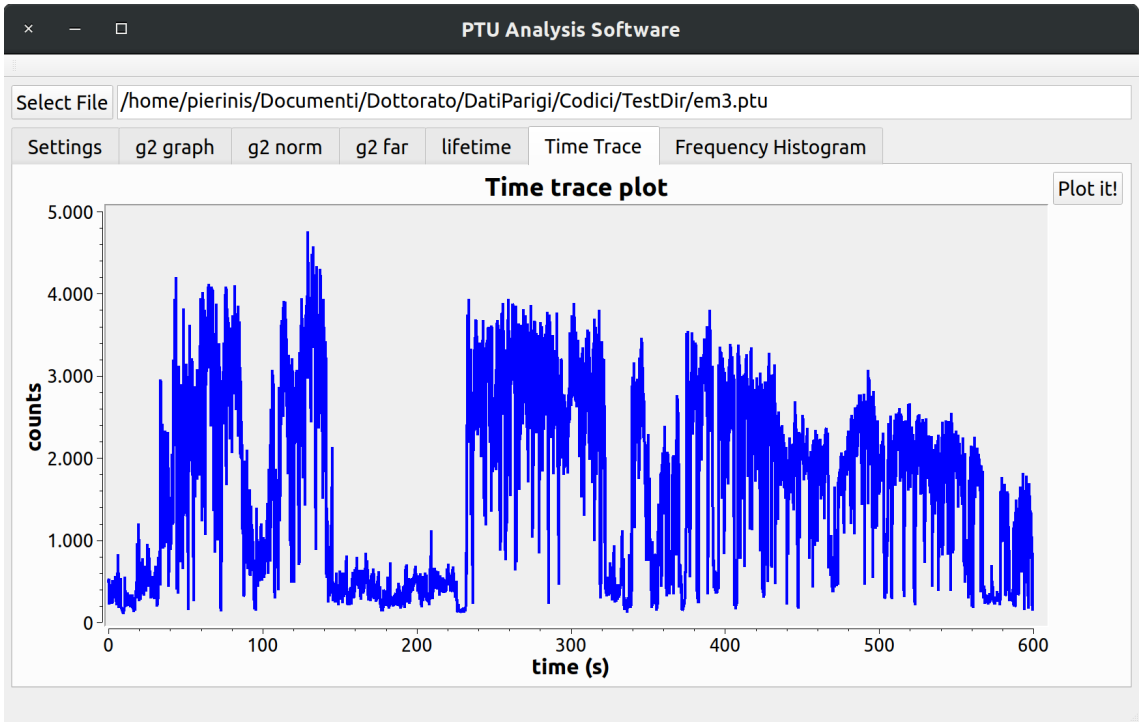

(a)

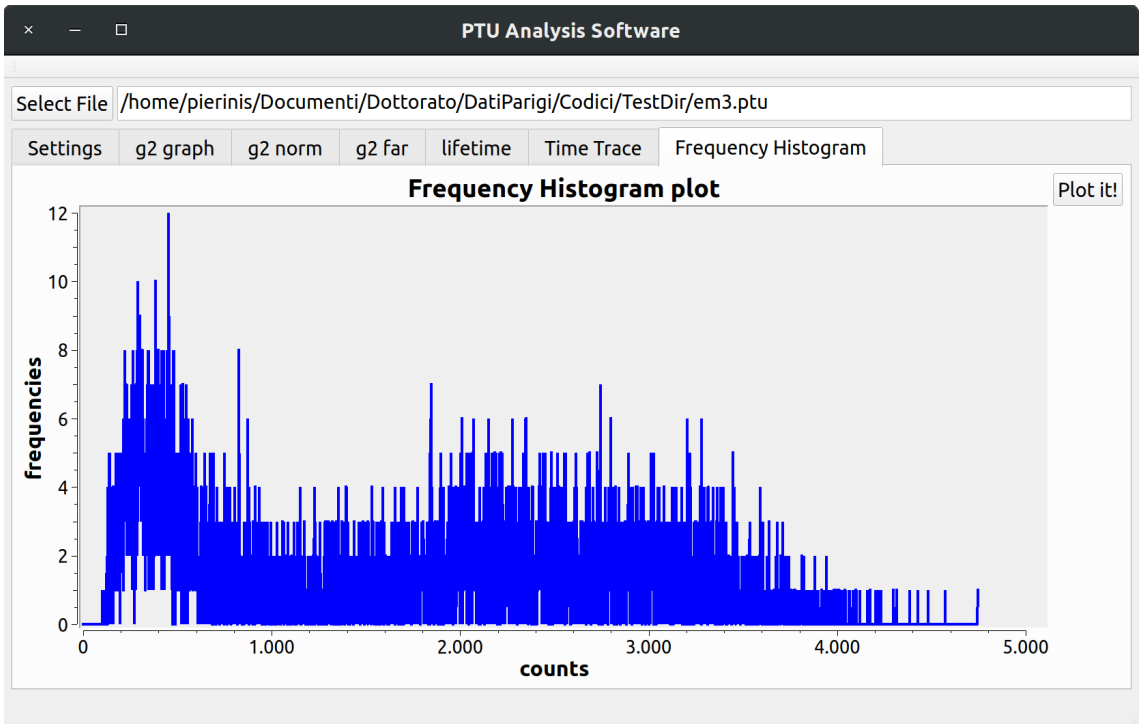

(b)

Figure A.5 – Example screenshot of *Time Trace* A.5a and *Frequency Histogram* A.5b panels.

On the y axis the number of occurrences is reported (labeled as *frequencies*) in the application, while on the x axis the number of counts is reported, corresponding to the y axes of the intensity trace plot. A file containing a matrix of a lifetime histogram for each bins in the frequency histogram plot is also created. This can be used to study the lifetime dependence of the blinking.

Any of this plot is made reading the data previously analyzed with the *Settings* panel: the analysis saves the analyzed data in multiple files that are read by the application when clicking on *plot it* of each panel. The data are saved in text format, allowing an easier opening with different application to perform further analysis as for example the fits.

A.2.3 Possible future improvements

I spent time to make the software stable: now events like "the file does not exists" when clicking on the *plot it!* button does not make the software crash, but raise an error.

I also added various functions, as the experience has shown that they are important. For example, the progress bar showing the progress of the analysis is useful to know that the program is not frozen but it is still running and to estimate the time needed for the operation.

Anyway, several improvements can still be done. Some suggestions are listed below:

- Adding a panel or an option to perform batch analysis could be useful as it could allow to leave the code performing the analysis of multiple files alone. This could be a great point as each analysis can take several minutes. Ideally this batch analysis could use multiple processes, in order to run efficiently on multi-core CPUs.

- An estimation of the ending time could be shown during the analysis.

- The ability to analyze the plotted data with the most common analysis could be added. Here the main problem is the difficulty to perform a fit using C++. Indeed, there is a good and stable library that was written for the C programming language that could be used: the gnu scientific library. Unfortunately its usage is not straightforward (e.g. it requires to manually calculate and declare the Hessian matrix of the function that we want to fit) and requires time to be implemented. The advantage is that it is a low level library and, once implemented, the fitting process will be fast.

- The possibility to save the graphs in pdf format has been added only for the "$g^{(2)}$ far" function, as it is the one that one would more likely want to save. Anyway, this could be added for any plot with minor effort.

- Finally, a cleaner saving of data and metadata could be realized. In the actual option any analysis of the same file overwrite the previous one: it could be useful to save the output files of each analysis in different directories and create a file with the history of the analysis that has been performed.

Of course there are other improvements that can be performed, but in my opinion these are the most important ones.

A.3 Tools used

A.3.1 C++ programming language

The C programming language is one of the most diffused languages. It was created by Dennis Ritchie bewtween 1969 and 1973. In 1972 was born the first Unix operating system entirely written in C: modern operating systems derived from it are MacOS and GNU/Linux, the first one is used in personal computers while the second one is largely diffused on servers and on mobile phones.

The strength of the Unix operating system and its evolutions shows the power of the C programming language, that is now the reference in most of the modern hardware platform. As it is strongly related to Unix, it has an implementation on almost any new operating systems.

The C++ programming language initially was an extension of the C programming language in order to add classes and increase the level of abstraction of the language to make the programming easier. Its development was cured by Bjarne Stroustrup and started in 1979. The advantage of the C++ is that it is object oriented, differently from the C that is procedural: it allows a modern approach while keeping most of the advantages of C. As for the C language, there are open source compilers, that ensure the code to be accessible free-of-charge also in the future. This is the main advantage with respect to other languages, like Matlab, that strongly depends on the license of the producer.

If we compare it with Python, another largely diffused programming language in science, also based on C libraries, C++ is probably more difficult to write but is faster in the execution. Thus, it is convenient for applications that manipulate large data files.

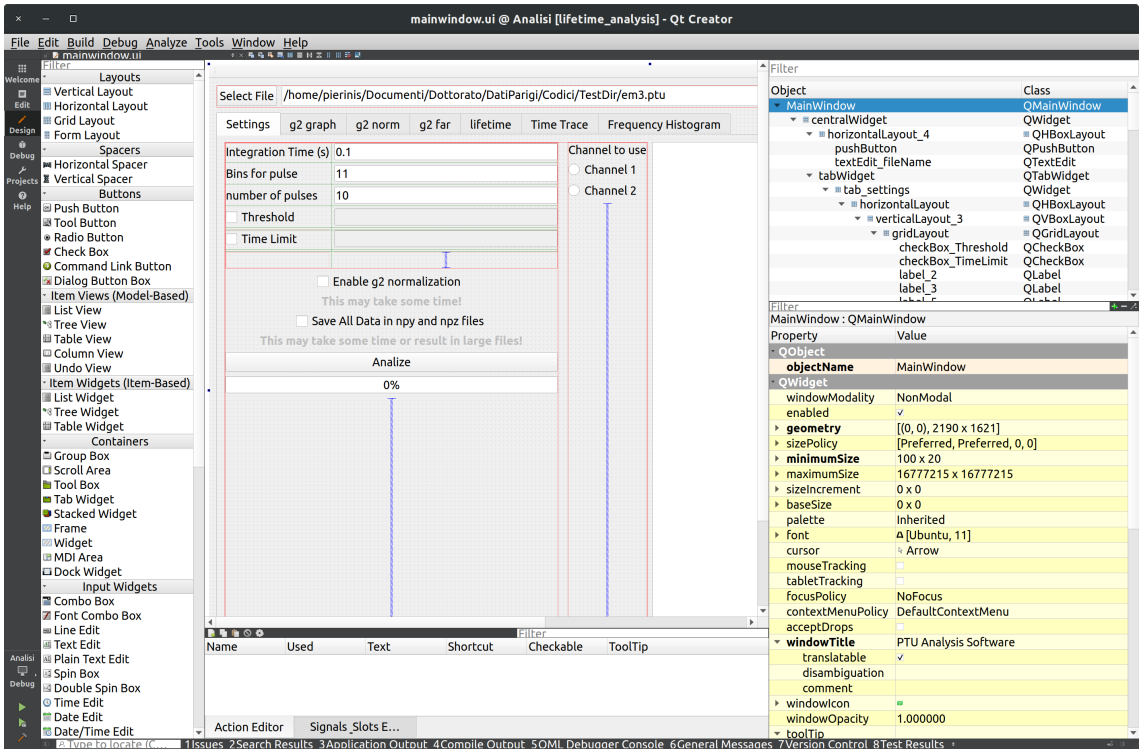

Figure A.6 – Qt Creator window in the part that enable creation and editing of the graphical interface.

Anyway, for applications that do not require a huge effort from the computer side, such as experimental routines, Python is often easier to write and to maintain.

A.3.2 Qt

"Qt is not a programming language on its own. It as a framework written in C++"[121]. Instead, Qt is a cross-platform framework to develop applications in C++. This means that writing a program in Qt it is possible to deploy it on different operating systems (Linux, OS X,Windows) with minor changes.

It is available with two licenses: one that is useful for companies that want to sell their programs but also the GPL license, one of the most important licenses for open source software. The last one is not adapted for producing open source codes. It allows the creation of graphic user interfaces (GUI) in an easy way, simply dragging and dropping the various elements and manually designing it. To show the graph I used the Qwt plugin to the Qt software, that makes this quite easy.[122] In figure A.6 an image of the Qt Creator program that enables to create the graphical interface is shown.

A.4 Algorithm and code details

Complete code listings are not in the scope of this Appendix, and can be requested to me if needed. However a description of the structure of the code could be useful to future users.

The easiest way to start a new qt project is to use *Qt Creator* program, different kinds of blank projects can be selected: in my case I created a desktop application, but mobile applications can also be created. Any Qt project is divided in multiple files, knowing them is the first step to get oriented in the code. I describe in the following the main file types and then proceed with a description of the main points of the analysis algorithm.

A.4.1 Principal files of the code

- One file has a `.pro` extension. It is the **project** file that configures the code and contains the list of the other files of the project, the list of the libraries and where to find them, the version of C++ used (in my case C++11). It is usually created by *Qt Creator* but it needs some time to be manually edited. A screenshot of this file is reported in figure A.7; following it, it is easier to analyze the other file types
- The **sources** files contain the classes used by the application. In objective programming, a Class is the description of the characteristics of a certain object. In the code, the class can be called to create an instance of the object. In my case four classes are present:
  - the *main* class is called on program starting, creates the application and opens the main window
  - *mainwindow* contains the instruction for the creation of the main window of the graphical user interface
  - *measure* here the most of the analysis code is present, the object is created when launching an analysis
  - *lifetime_matrix* is used to create a matrix containing a lifetime histogram for each intensity recorded in the Frequency Histogram plot, as explained in section A.2.2
  - *cnpy* contains the code of an open source library used to write data in a format (`.npy`, `.npz`) easily readable with the *numpy* library of python; *numpy* is largely used in data analysis and the data in this format are useful to be elaborated in further analysis.

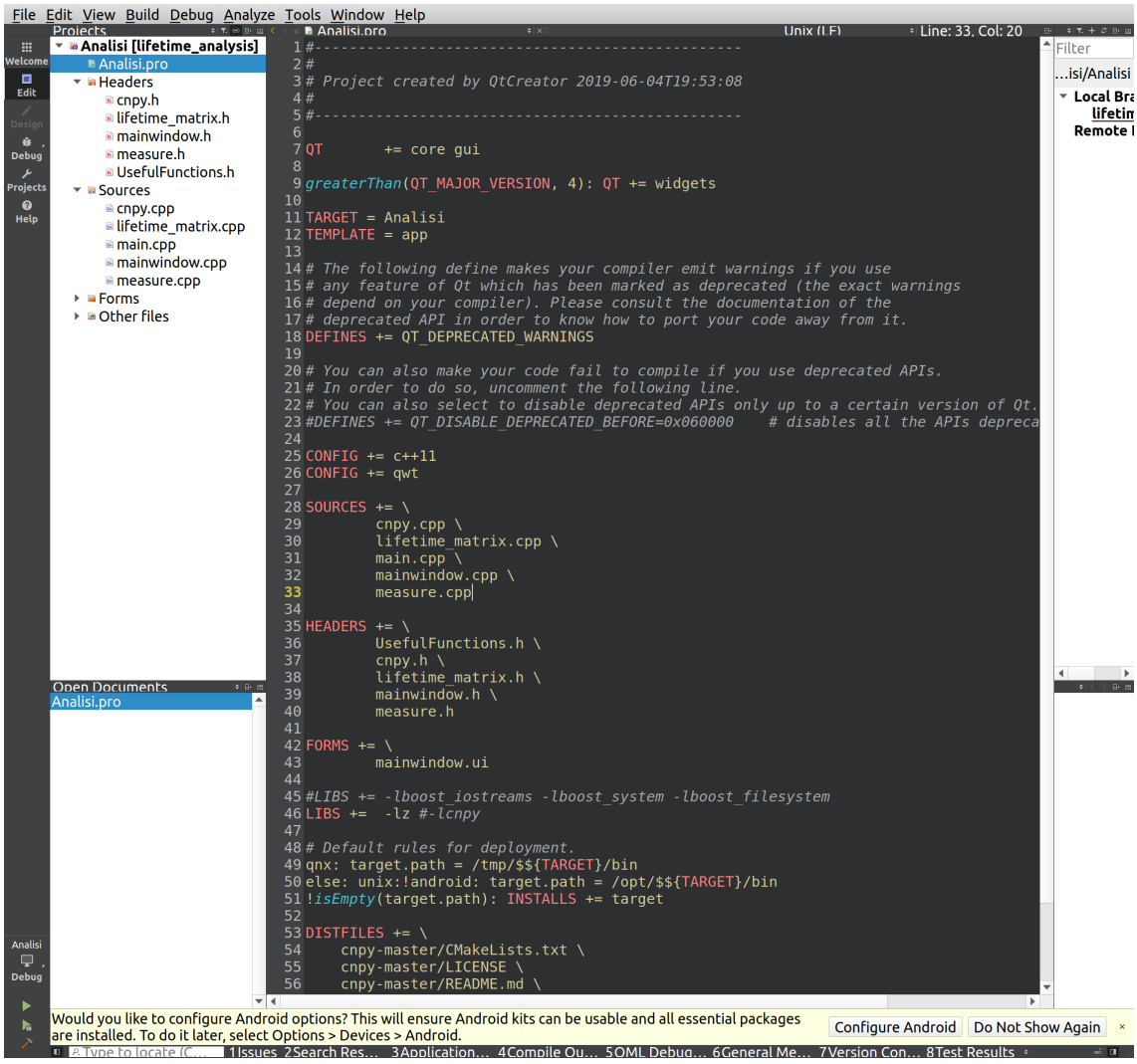

Figure A.7 – Screenshot of *Qt Creator* software showing the `.pro` file of my project. It is visible the list of the project files as described in the text and various included libraries, the most important of which is the Qwt library. This is the version running on linux; slight modification are needed on windows.

- The **headers** corresponds to the class file. They contain the variable definitions and their initial value as well as the paradigms. A paradigm contains the name of a method of the class and the type of method inputs and outputs.

- the **forms** are files that contain the description of the user interface. They are generated by the user interface designer of *Qt Creator* and they have the extension `.ui`.

A.4.2 Algorithm main points

The code contained in the *measure.cpp* file is more than 1000 lines and it is not convenient to report it here entirely. The code has been written starting from the *demo* code provided by Picoquant, that extracts from the file the measurement parameter known to the instrument and the lines where each photon arrival time is recorded. The goal was to analyze it without the occupation of too much memory, in order to avoid *segmentation fault* errors and in the most time efficient way. The strategy I choose was to analyze each lines on the fly during their collection process.

For each photon in the file the function *got photon* is called. The information of the line is recorded in a structure, called *fotone*. The structure *fotone* is sent to a function that has the scope to measure what was the intensity when the photon was collected: for this reason it retains the structure in an array until all the collected photon of a given bin of the intensity trace are read from the `.ptu` file. Once the number of photons collected in the bin is known, this value is stored in each structure *fotone* collected up to now. The mean lifetime in the bin is also calculated; then a line is added to the TimeTrace file, containing the time to which the bin corresponds, the number of photons arrived in that bin and the calculated mean arrival time.

At this point each of the *fotone* structures collected up to now is sent to a function that has the goal to create the $g^{(2)}$ histogram and, if required by the user, to create the *far* $g^{(2)}$. They are created separately. Here two separate arrays with the last arrived photons are created large enough to contain the interval chosen by the user. The photon is assigned to the correct array and the delay between it and the photons already arrived in the other arrays is evaluated, adding eventually bins to the histogram. Here is the most time-consuming function, as it verifies for any arrived photons all the delay with previously arrived photons until the maximal delay desired is reached. This is the reason why the calculation of the *far* $g^{(2)}$histogram require time. In this case, in addition, only the peaks are recorded, to avoid to store too much data points that make the graph

difficult to plot and to visualize.

If the option to record all data in python files is selected, the information on each *fotone* are written there.

Finally, a function writes all the data in appropriate named files. The time required to calculate the $g^{(2)}$ function depends on the number of counts recorded and on the computer processor. In my experience, in order to calculate the $g^{(2)}$ far, with a quite new 8th generation i7 Intel processor under Ubuntu 18.04, it can takes half an hour for largest files. On the other hand, with lower quality processors under Windows we needed half a day of analysis. If the processor is multi-core, multiple instances needs to be launched in order to analyze multiple emitters at the same time and save time: as told before, ideally the application could be improved to natively support multi-processing without the need to launch multiple instances.

Annexe R

Résumé en français

Contents

A.1 Introduction 121
A.2 The software usage 122
A.2.1 *Settings* panel 123
A.2.2 Visualization panels 124
A.2.3 Possible future improvements 129
A.3 Tools used 130
A.3.1 C++ programming language 130
A.3.2 Qt 131
A.4 Algorithm and code details 132
A.4.1 Principal files of the code 132
A.4.2 Algorithm main points 134

R.1 Introduction

Les technologies quantiques utilisent pour l'élaboration et la transmission de l'information les principes fondamentaux de la mécanique quantique. Dans ce type de technologies, l'unité de base de l'information, appelée bit dans un appareil classique, est constituée d'un qu-bit. Idéalement, un qubit est un système quantique à deux niveaux, notés $|1\rangle$ et $|0\rangle$ en analogie à la notation qu'on utilise classiquement. Dans la théorie de l'information quantique, les réalisations physiques d'un qu-bit peuvent être variées, cependant elles possèdent toutes une caractéristique commune : chaque qu-bit peut se trouver non seulement dans un des deux états ($|\psi\rangle = |1\rangle$, $|\psi\rangle = |0\rangle$) mais aussi dans la superposition

de deux :

$$|\psi\rangle = \frac{1}{\sqrt{|\alpha|^2 + |\beta|^2}} (\alpha |0\rangle + \beta |1\rangle), \tag{R.1}$$

où α et β sont deux nombres complexes. L'ensemble des états possibles pour un qubit est représenté avec la sphère de Bloch, reportée en figure R.1. Chaque point de la sphère

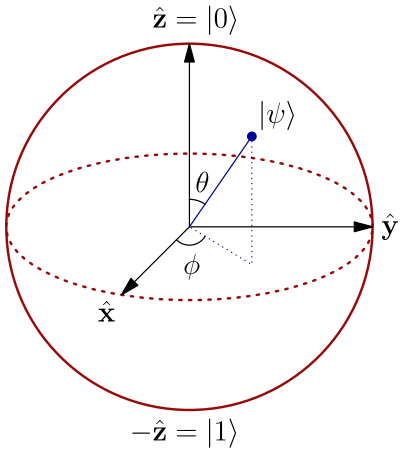

FIGURE R.1 – Représentation sur la sphère de Bloch d'un qubit $|\psi\rangle$. Chaque point sur la sphère correspond à un état $|\psi\rangle$ possible du qubit. $\vartheta = 0$ est en correspondance avec l'état $|0\rangle$, $\vartheta = \pi$ est en correspondance avec l'état $|1\rangle$.

correspond à un vecteur d'état possible ; en particulier les points situés aux pôles de la sphère correspondent respectivement aux états $|0\rangle$ et $|1\rangle$.

L'intérêt pour les technologies quantiques a augmenté de plus en plus dans les dernières années ; pour ce type d'applications et pour leur développement, il est important d'avoir des systèmes reproductibles et de pouvoir disposer d'un nombre suffisant de qubits dans des systèmes les plus compacts possibles. Comme support physique pour un qubit, les photons présentent plusieurs avantages, en particulier du point de vue de la facilité de manipulation et de transport. C'est pour cela que l'optique quantique, qui traite de l'étude de la lumière et des interactions lumière-matière du point de vue de la mécanique quantique, a connu un grand intérêt de la part de la communauté scientifique. En optique quantique, la lumière est considérée comme un ensemble de photons, les excitation fondamentales du champ électromagnétique.

R.1.1 Émetteurs à photon unique

Un émetteur à photon unique est défini comme un objet qui n'émet pas plus d'un seul photon à la fois. En pratique, on peut faire la distinction entre sources de photons uniques

stochastiques, par exemple lorsqu'un laser est atténué de telle sorte que la probabilité d'avoir deux photons en sortie soit faible, et sources de photons uniques déterministes. Dans ce dernier cas, la source n'émet pas plus d'un photon à la fois grâce à la nature des processus physiques qui sont à la base de la génération du photon.

Plusieurs réalisations pratiques sont possibles pour une source de photons uniques déterministe, comme des atomes uniques, des ions piégés, des boîtes quantiques ou des centres colorés dans les nanodiamants. Chacun de ces émetteurs présentent des avantages et des inconvénients. En particulier, dans ma thèse je me suis concentré sur les deux derniers types d'émetteurs, en étudiant les propriétés des boîtes quantiques de pérovskite et de centres colorés dans les nanodiamants.

Je détaille brièvement ci dessous quelques unes des caratéristiques les plus intéressantes de ce genre d'émetteurs.

Mécanisme d'émission

Il s'agit d'émetteurs avec une structure de bandes similaire à celle d'un semi-conducteur. Leur excitation est généralement assurée par une source laser hors résonance, qui va créer un ou plusieurs excitons. Les excitons peuvent se recombiner de façon radiative (avec émission d'un photon) ou non radiative. L'émission de photons uniques dans ce type d'émetteurs est principalment due à l'effet de recombinaison Auger, qui impose qu'un seul exciton, le dernier, peut se recombiner de façon radiative, tandis que tous les autres ont un canal privilégié de recombinaison non radiative où l'énergie est cédée à un autre exciton. Ce mécanisme est illustré en figure R.2.

Saturation

En augmentant la puissance d'excitation, on observe un effet de saturation de l'émission. Dans les boites quantiques, cet effet est observable grâce à la présence de la recombinaison Auger : en effet, quand on augmente la puissance, plusieurs excitons sont créés simultanément mais seulement l'un d'entre eux relaxera de façon non radiative, en émettant un photon. L'équation qui décrit ce comportement est la suivante :

$$P_{PL}(P) = P_{sat} \cdot \left(1 - e^{-\frac{I}{I_{sat}}}\right) + B \cdot I \tag{R.2}$$

où B est un paramètre qui rend compte du fait que l'effet Auger n'est pas complètement efficace. Des exemples de courbes de saturation sont montrés dans la figure R.3.

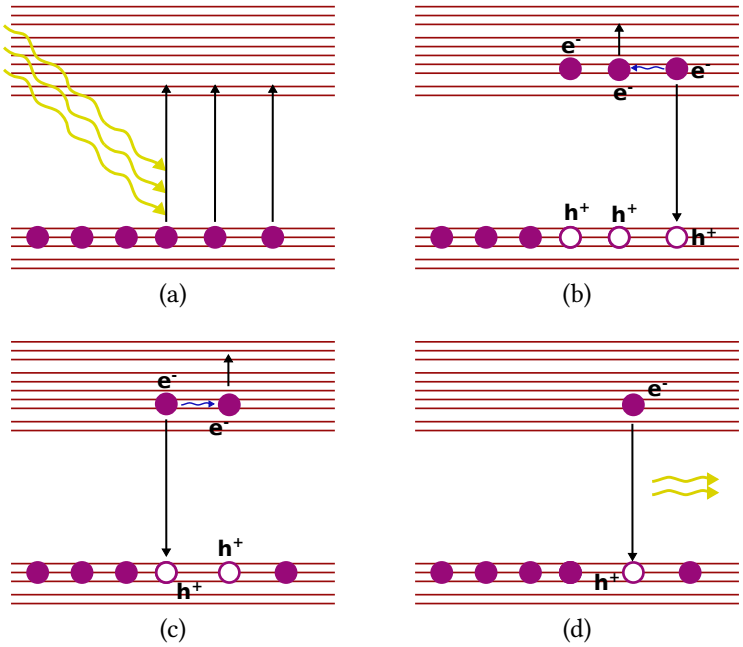

FIGURE R.2 – Mecanisme de recombinaison Auger : (a) Le semi-conducteur est excité par un laser et plusieurs excitons sont créés. (b) et (c) tant que plusieurs excitons sont présents, un exciton peut relaxer en cédant son énergie aux autres ; enfin (d) le dernier exciton ne peut que relaxer radiativement en émettant un seul photon.

Temps de vie de l'émission

Les mesures des temps de vie ont un rôle important dans la caractérisation d'un émetteur à photons uniques : en effet elles constituent une mesure directe du temps de relaxation radiative. On reporte sur un histogramme les délais de collection des photons après l'excitation et on obtient une décroissance exponentielle reportée en figure R.4. Dans le cas général où plusieurs états d'émission sont présents, on peut décrire telle courbe à l'aide de l'équation suivante :

$$I = \sum_i A_i \cdot e^{-t/\tau_i} \tag{R.3}$$

Clignotement

Beaucoup d'émetteurs, à cause des effets de piégeage des charges, ont une émission intermittente. Ce comportement peut constituer un sérieux problème pour les applications et il est donc intéressant de l'étudier. Pour analyser le clignotement il y a plusieurs techniques différentes.

La plus simple prévoit d'utiliser un seuil sur la trace d'intensité ou trace de clignotement : elle est créée en choisissant un intervalle temporel et en comptant le nombre

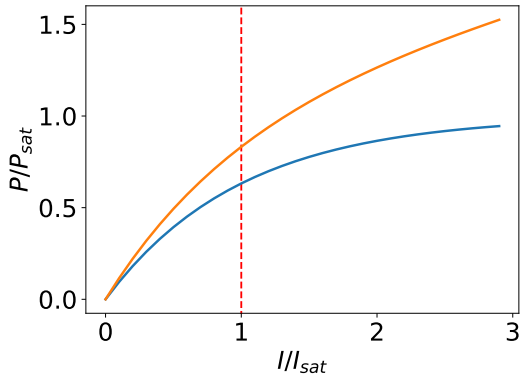

FIGURE R.3 – En bleu, la courbe de saturation décrite par l'équation (R.2) avec $B = 0$, en orange la courbe décrite par la même équation quand $B = 0.2P_{sat}/I$.

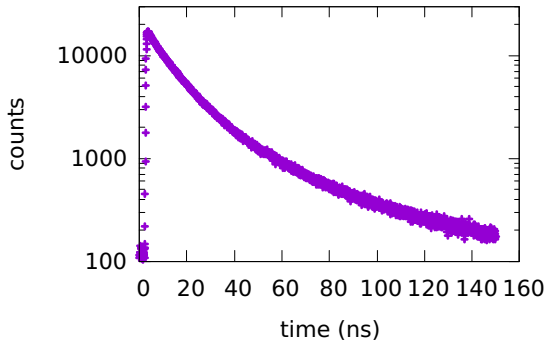

FIGURE R.4 – Histogramme du temps de vie ; mesure effectuée sur l'émission d'un seul CdS/CdSe nanocristal dot-in-rod. Chaque point représente le nombre de photons qui sont arrivés sur le détecteur avec un certain retard. L'histogramme correspond à une fonction exponentielle décroissante (équation (R.3)).

de photons qui arrivent dans cet intervalle. On peut ensuite définir un seuil et considérer que l'émetteur est dans un état *éteint* quand le nombre de photons collectés dans un certain intervalle est inférieur au seuil et *allumé* quand le nombre des photons collectés dans un certain intervalle est supérieur au seuil. À ce stade on peut définir la durée d'un état, *allumé* ou *éteint*, créer une distribution cumulative et étudier ses caractéristiques. Cette approche présente le problème d'être fortement influencée par le choix de la durée de l'intervalle ; en effet si le temps de clignotement est plus court que cette durée, ce type d'analyse n'est pas adéquat. De plus on ne peut pas choisir un intervalle trop court, car on doit avoir suffisamment de comptages pour pouvoir sélectionner un seuil.

Quand on ne peut pas séparer l'état *éteint* de l'état *allumé* on utilise une approche différente. On peut en effet définir la FLID (*fluorescence life intensity distribution*), intro-

duite pour la première fois par Galland *et al.* [51]. Ce type de représentation consiste à calculer le temps moyen d'arrivée des photons pour chaque intervalle de la trace d'intensité ; ensuite la densité de probabilité en fonction de l'intensité du signal et des temps d'arrivée de photons est reconstruite. Un exemple de cette représentation est montré en figure R.5. Dans ce cas, plutôt que de clignotement on parle de *flickering*. En général

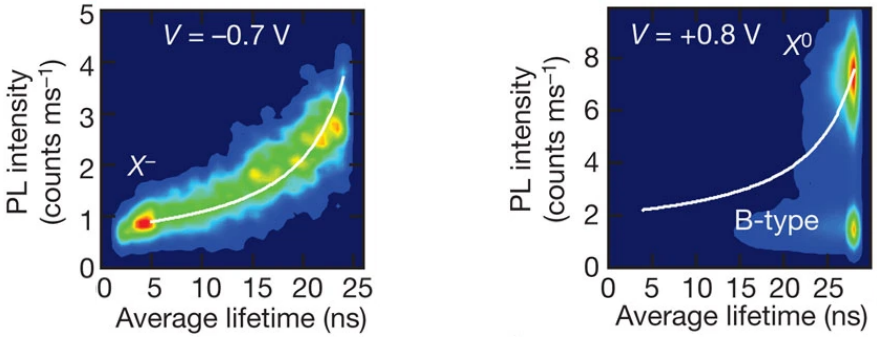

(a) (b)

Figure R.5 – FLID : (a) en présence du clignotement de type A, le temps de vie moyen dépend de l'intensité émise ; au contraire, (b) en présence du clignotement de type B, le temps de vie moyen ne dépend pas de l'intensité émise. *(credits:* Galland et al. *[51]).*

on peut distinguer deux types de clignotement, type A et type B. Dans le cas d'un clignotement de type A, le temps de vie dépend de l'intensité d'émission. Dans le cas d'un clignotement de type B, le temps de vie ne dépend pas de l'intensité de l'émission. D'un point de vue physique, les deux différents types de clignotement correspondent à des mécanismes de relaxation différents.

- Dans le cas du clignotement de type A, la transition de l'état *allumé* vers l'état *éteint* a lieu quand un porteur de charge se déplace dans un état piégé. La transition inverse, de l'état *éteint* vers l'état *allumé*, a lieu quand il est libéré via un processus de relaxation. Ces types de clignotement sont représentés dans la figure R.6.
- Dans le cas du clignotement de type B, les fluctuations d'intensité sont dues à un piégeage rapide des électrons suivi d'une recombinaison non radiative. Ce mécanisme ne comporte pas une variation du temps de vie de l'émission.

Polarisation

La polarisation de la lumière émise par les émetteurs est une caractéristique importante : il est donc utile de la mesurer. Il y a plusieurs façons différentes pour représenter la

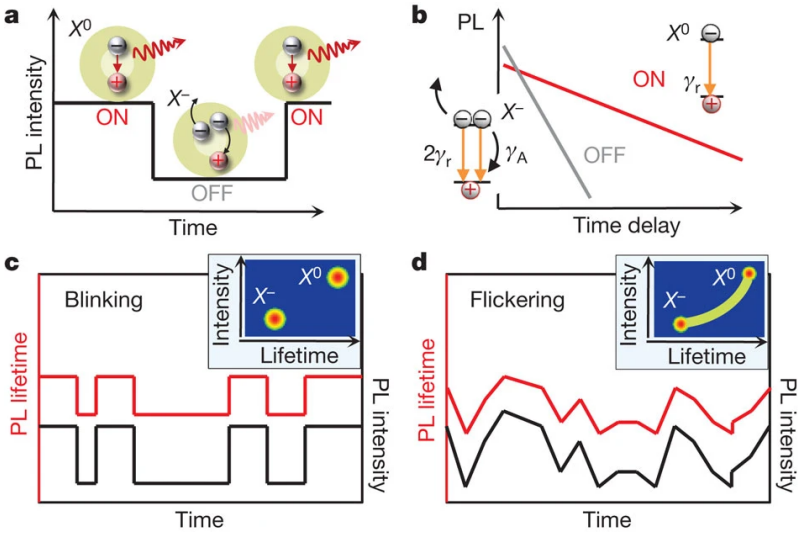

FIGURE R.6 – Mécanisme de clignotement de type A : a) l'état *allumé* correspond à l'état neutre, l'état *éteint* correspond à l'état chargé négativement. b) Des mécanismes différents correspondent à des temps de vie différents. c) Le cas d'un clignotement "propre" correspond à deux points différents sur la FLID ; le cas de *flickering* correspond à une courbe continue sur la FLID. *(credits: GALLAND et al. [51]).*

polarisation de la lumière. Au niveau analytique, on utilise généralement les paramètres de Stokes, qu'on peut indiquer S_0, S_1, S_2, S_3. Ils représentent respectivement

S_0 L'intensité,

S_1 le degrée de polarisation horizontal/vertical,

S_2 le degrée de polarisation à ±45°,

S_3 le degrée de polarisation circulaire.

Dans le cas d'une polarisation entièrement linéaire la relation suivante est valable :

$$S_0^2 = S_1^2 + S_2^2 + S_3^2 \tag{R.4}$$

Alternativement, on peut utiliser la sphère de Poincaré ou l'ellipse de polarisation, qui sont deux méthodes pour représenter graphiquement la polarisation. Elles sont montrées dans la figure R.7.

R.1.2 Optique guidée et integrée

Quand on parle d'optique on peut avoir deux approches différentes. La première, bien connue et utilisée depuis longtemps, est l'optique en espace libre : la lumière est réfléchie

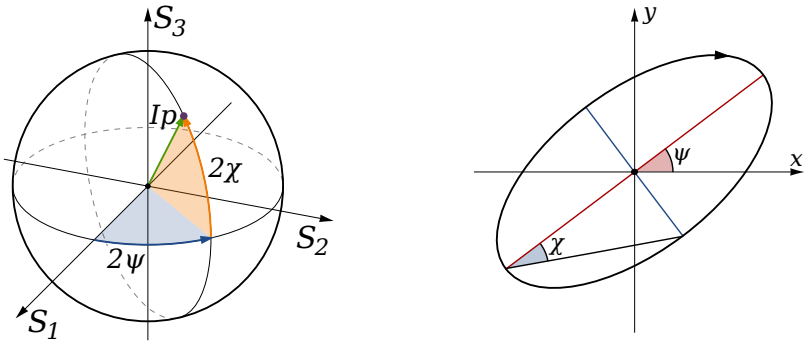

(a) (b)

FIGURE R.7 – Représentations graphiques pour la polarisation. (a) Sphère de Poincaré : La polarisation est représentée comme un point sur la sphère, les cordonnées du point sont en relation avec le vecteur de Bloch selon les équations (1.31). (b) Ellipse de polarisation : c'est une visualisation de la polarisation sur deux dimensions, elle est plus simple à reproduire sur un support plat. Elle contient la même quantité d'information que la sphère de Poincaré. *credits: Wikimedia Common.*

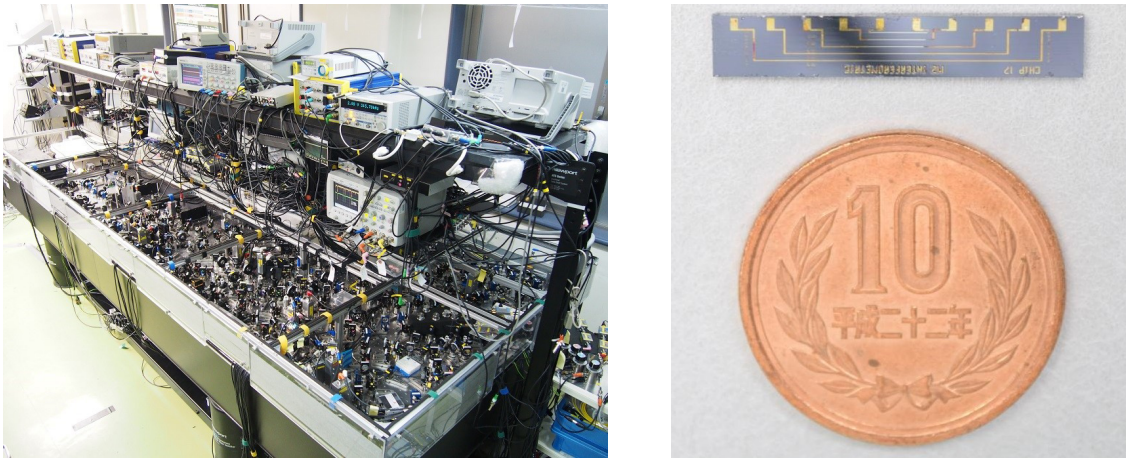

(a) (b)

FIGURE R.8 – Différence entre espace libre (a) et optique intégrée (b). L'optique en espace libre est flexible et bien connue, mais demande un alignement précis et de grandes surfaces ; à l'opposé l'optique intégrée est stable et ne demande pas d'opération d'alignement. *credits: University of Bristol.*

par des miroirs et modifiée par des lentilles, des lames d'onde, etc. L'optique en espace libre présente, par contre, l'inconvénient de nécessiter d'une grande quantité d'espace, des réalignements réguliers et de ne pas pouvoir être produite en série : des contraintes qui deviennent des limites pour des applications.

Une deuxième approche possible est celle de l'optique intégrée qui présente plusieurs avantages :

- Elle est stable
- elle est compacte
- elle peut être reproduite industriellement en plusieurs exemplaires identiques

Ces avantages sont évidents si l'on regarde la figure R.8.

Un exemple connu d'optique guidée est représenté par les fibres optiques, qui, depuis leur découverte, ont trouvé beaucoup d'applications dans différents domaines. Pour les applications, il serait utile de coupler les sources de lumière à des structures optiques guidées sans avoir besoin d'optique en espace libre, comme le microscope. Dans le cadre de ma thèse, j'ai étudié le couplage d'émetteurs de photons uniques avec des nanofibres optiques, couplage dû aux effets du champ proche. J'ai également étudié le couplage des nanoémetteurs avec des guides d'onde à échange ionique.

R.2 Pérovskite

Les cristaux de pérovskite sont des cristaux avec une structure similaire à celle de l'Oxyde de Calcium et Titane, qui est le premier minéral de ce genre à avoir été découvert. Leur structure est représentée dans la figure R.9b. La structure des pérovskites est du type ABX_3, ou A et B sont des cations métalliques, avec les cations B plus petits que les cations A, et X un anion métallique.

Les opticiens se sont intéressés aux pérovskites car leur structure ordonnée leur confère un caractère de semi-conducteurs, et elles sont donc intéressantes pour des applications dans le domaine du photo-voltaïque. Cependant, leur caractère semi-conducteur les rend intéressants aussi pour la synthèse de nanocristaux émetteurs de photons uniques.

R.2.1 Nanocristaux de Pérovskite

Les nanocristaux sont des boites quantiques intéressantes. Ils sont fabriqués par voie chimique et ils émettent des photons uniques à température ambiante. Les boites quantiques

(a) (b)

FIGURE R.9 – (a) Cristaux de pérovskite, originaires de Magnet Cove, Arkansas, USA. *(credits Wikimedia Commons)* (b) Structure 3D d'une perovskite (ABX_3) : en rouge les atomes X, anions, en vert les atomes B et en jaune les atomes A. A et B sont des cations métalliques, avec les cations B plus petits que les cations A.

de pérovskite présentent les mêmes avantages que les nanocristaux semi-conducteurs et y ajoutent la possibilité de contrôler la longueur d'onde d'émission en jouant sur la composition avec une flexibilité plus grande que dans les nanocristaux semi-conducteurs. Leur principale limitation vient de leur stabilité optique très faible et c'est précisément sur l'amélioration de cet aspect que j'ai travaillé.

R.2.2 Caractérisation expérimentale

J'ai utilisé des nanocristaux fabriqués par Emmanuel Lhuillier à l'"Institut de Nanosciences de Paris". Leur synthèse demande seulement quelques heures : cet avantage, que les pérovskites on en commun avec les autres nanocristaux colloïdaux, est un atout considérable en comparaison d'autres émetteurs, tels que les défauts SiV dans les nanodiamants. J'ai travaillé principalement avec deux échantillons différents :

échantillon A fabriqué avec la technique décrite par PROTESESCU *et al.* [69]

échantillon B fabriqué avec une technique différente, utilisée pour la première fois dans le but de produire des émetteurs de photons uniques. Cette technique est décrite dans PIERINI *et al.* [123]

Pour étudier les nanocristaux, j'ai préparé les échantillons en déposant la solution contenant les émetteurs avec un appareil pour faire le revêtement par centrifugation. Une goutte de solution contentant les émetteurs est déposée sur une lamelle de microscope, mise en rotation par la machine afin de distribuer la solution de façon homogène sur la lamelle, qui est ensuite regardée en utilisant un microscope confocal, comme décrit dans la suite.

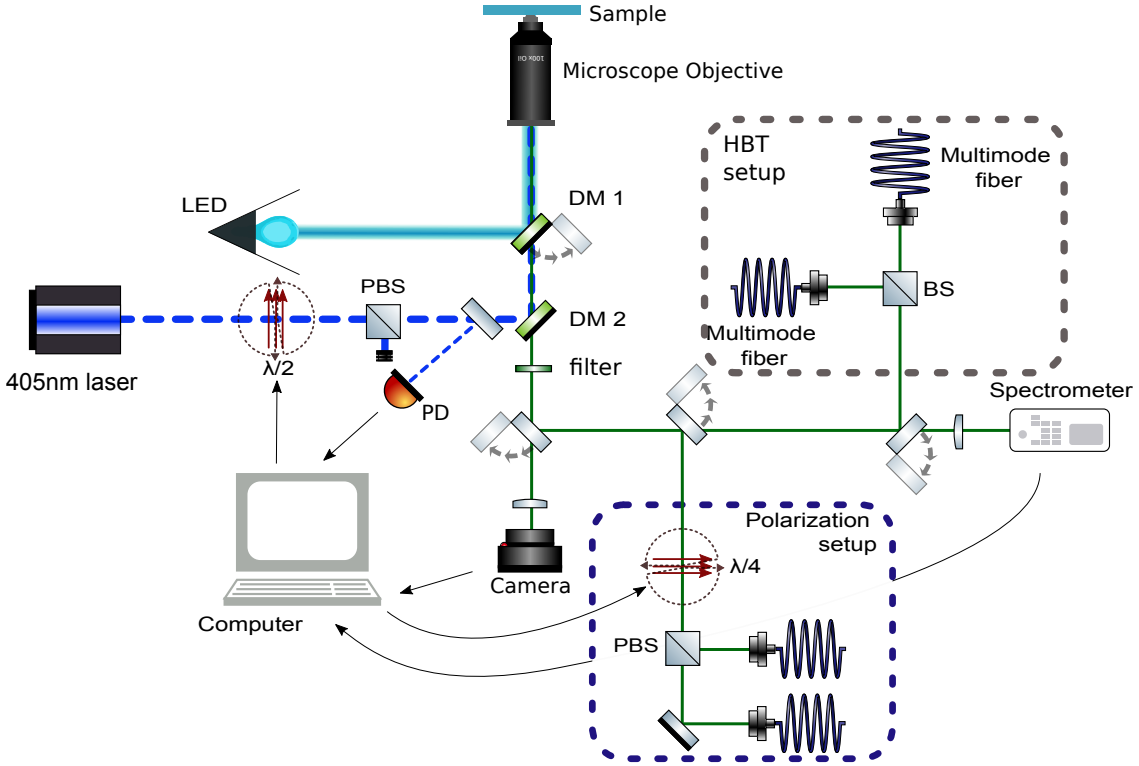

FIGURE R.10 – Montage expérimental pour l'analyse d'un nanocristal unique. Pour une vision en champ-large, la lumière de la LED est réfléchie par un filtre dichroïque et envoyée vers l'échantillon à travers l'objectif. Pour exciter un émetteur unique, le laser pulsé est réfléchi vers l'échantillon. La lumière collectée par la LED est filtrée pour enlever toute trace de la lumière d'excitation et peut ensuite être envoyée vers la camera, le spectromètre ou le montage pour mesurer le $g^{(2)}(\tau)$ (montage HBT). DM : Miroir Dichroïque ; BS : miroir semi-réfléchissant ; PBS : cube polariseur ; Ph : photodiode ; $\lambda/2$: lame demi-onde tournante ; $\lambda/4$: lame quart d'onde tournante.

Montage expérimental

Le montage utilisé pour étudier les émetteurs est montré en figure R.10 L'échantillon est déposé sur le microscope. Afin de sélectionner un émetteur, la LED est utilisée pour regarder un espace suffisamment large. Une image d'un échantillon illuminé avec un spot de grande dimension est montrée en figure R.11

En utilisant des translations motorisées, l'échantillon est déplacé pour placer l'émetteur à l'intérieur du faisceau laser. Ensuite, la LED est éteinte et le laser est utilisé pour exciter l'émetteur et effectuer les mesures : spectre, intensité de saturation, $g^{(2)}(\tau)$, clignotement, polarisation.

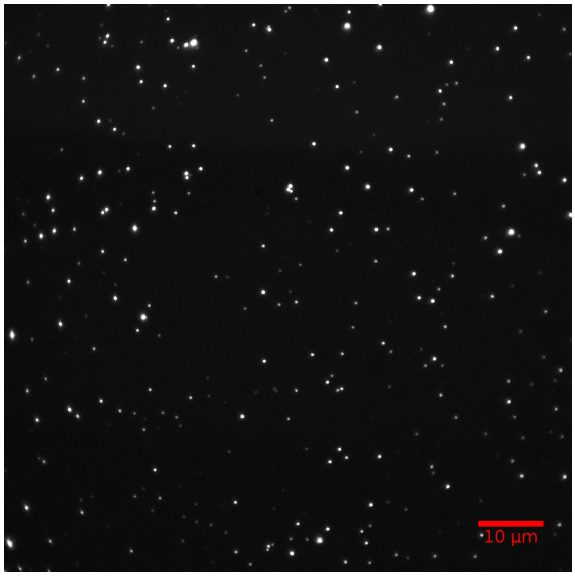

FIGURE R.11 – Exemple d'une image obtenue avec la camera quand l'échantillon est illuminé avec la LED. Les points blancs sont les émetteurs, le fond est noir car la lumière d'excitation est filtrée.

R.2.3 Mesures

Spectres

On peut mesurer les spectres avec le spectromètre. La largeur spectrale et la forme de l'émission sont intéressantes : en effet pour de nombreuses applications telles que le couplage avec des cavités optiques ou encore la conversion de fréquence, on recherche de raies d'émission étroites. En plus, avec une statistique sur les spectres on peut avoir des informations sur les différences entre émetteurs. Par exemple, un spectre est représenté en figure R.12. Dans la figure R.13 est reportée une analyse statistique pour le spectre d'émission et pour la longueur d'onde d'émission centrale. On peut s'attendre à un plus grand confinement dans l'échantillon B car la longueur d'onde d'émission est inférieure.

R.2.4 Saturation

La saturation est importante car elle nous permet de comparer les émetteurs : en effet, on a fait le choix d'exciter tous les émetteurs à l'intensité de saturation. À cause de la présence du clignotement, pour pouvoir faire une mesure de saturation correcte, il est important de prendre en compte d'éventuelles variations de luminosité : pour cela on effectue plusieurs mesures à la même puissance et on considère seulement celle qui détecte l'émission la plus intense. On suppose en effet que ce soit celle où l'émetteur était

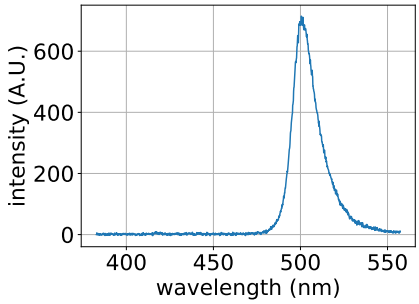

FIGURE R.12 – Spectre d'émission d'un nanocristal unique de pérovskite. Dans cet exemple on observe un pic d'émission à 500 nm.

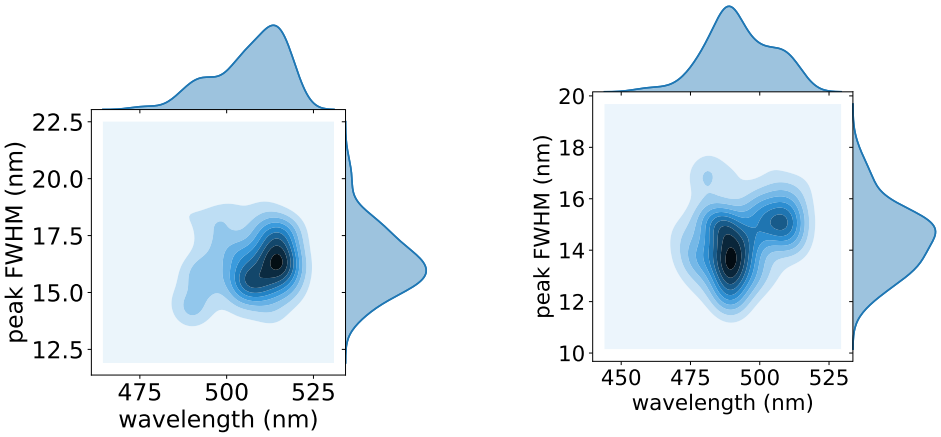

(a) (b)

FIGURE R.13 – Distribution de la longueur d'onde d'émission centrale et de la largeur à mi hauteur pour un échantillon A (a) (calcul fait avec 135 émetteurs) et B (b) (calcul fait avec 135 émetteurs).

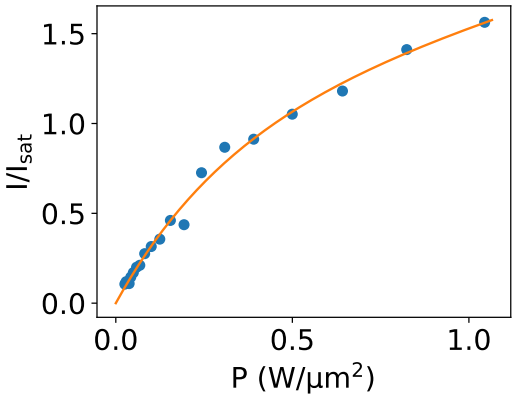

FIGURE R.14 – Exemple de mesure de saturation sur un nanocristal unique de pérovskite

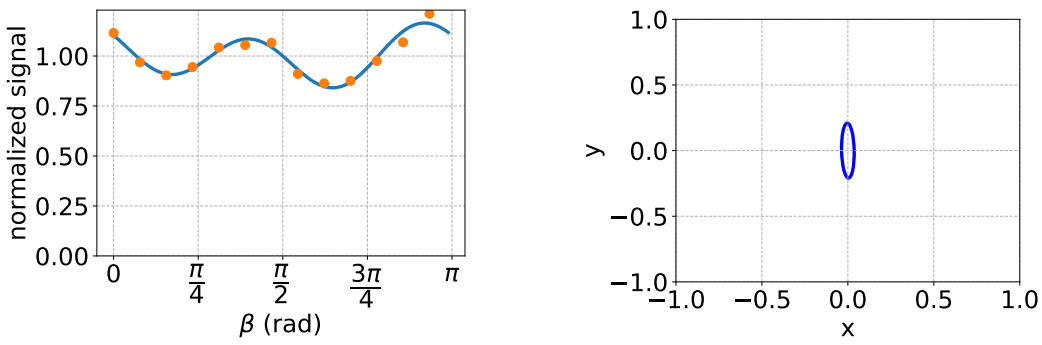

(a) (b)

FIGURE R.15 – (a) Exemple de mesure des paramètres de Stokes pour la lumière émise par un nanocristal de pérovskite. Les points rouges sont les données expérimentales, la courbe bleue est décrite par l'équation (R.6). (b) Ellipse de polarisation. Le degrée de polarisation est 0.18 et le degrée de polarisation linéaire est 0.17, cela montre une émission partiellement polarisée.

toujours dans l'état allumé. Un exemple de mesure de saturation sur des pérovskites est représenté en figure R.14. La courbe orange représente le fit avec la fonction définie précédemment :

$$P = A \cdot \left[1 - e^{-\frac{I}{I_{sat}}}\right] + B \cdot I \tag{R.5}$$

R.2.5 Mesures de polarisation

Pour mesurer la polarisation on tourne une lame quart d'onde et on polarise ensuite la lumière avec un cube polariseur. En mesurant l'intensité transmise par le cube en fonction de la position de la lame quart d'onde, il est possible de remonter aux paramètres de Stokes. La relation qui connecte les paramètres de Stokes S_0, S_1, S_2, S_3, l'intensité transmise I_T, l'angle de rotation du polariseur α (dans notre cas le cube), l'angle de rotation de l'axe rapide de la lame d'onde β et le retard introduit par la lame d'onde δ est la suivante :

$$\begin{aligned} I_T(\alpha,\beta,\delta) = &\frac{1}{2}\left[S_0 + \left(\frac{S_1}{2}\cos 2\alpha + \frac{S_2}{2}\sin 2\alpha\right)(1+\cos\delta)\right] + \\ &+ \frac{1}{2}[S_3 \sin\delta \cdot \sin(2\alpha - 2\beta)] + \\ &+ \frac{1}{4}[(S_1\cos 2\alpha - S_2 \sin 2\alpha)\cos 4\beta + \\ &+ (S_1 \sin 2\alpha + S_2 \cos 2\alpha)\sin 4\beta](1-\cos\delta). \end{aligned} \tag{R.6}$$

Avec cette relation, en mesurant un nombre suffisant de points et en utilisant le développement en série de Fourier, il est possible d'obtenir les valeurs des coefficients S_0, S_1, S_2, S_3 de façon analytique [73]. La figure R.15 présente un exemple de mesure des paramètres de Stokes sur un nanocristal unique de pérovskites.

Mesures de $g^{(2)}$

D'un point de vue expérimental, la mesure de l'émission des photons uniques se fait grâce à une mesure d'autocorrélation. Le signal est divisé en deux parties et chacune d'elles est envoyée vers un module compteur des photons ; on regarde ensuite la corrélation entre le signal sur un détecteur et le signal sur l'autre. D'un point de vue expérimental, ce type de mesures présente plusieurs difficultés :

1. tout d'abord, il s'agit d'une mesure qui demande de travailler dans l'obscurité, car chaque photon parasite qui arrive sur le détecteur peut la perturber. Cependant, on peut essayer de réduire l'effet des *dark counts* en corrigeant le signal après la mesure.

2. une grande quantité de données est collectée pendant la mesure, et donc une grande quantité de données est à élaborer par la suite.

3. Le système de détection présente la limite de ne pas pouvoir détecter deux photons en même temps. L'intérêt de la mesure est exactement de vérifier si, dans les deux parties il y a deux photons au même temps. On peut résoudre le problème en ajoutant une ligne de retard.

Un exemple de mesure de $g^{(2)}$ est reporté en figure R.16. En particulier, en figure R.16a est montré le signal de $g^{(2)}$ sans aucun traitement. On voit au centre le temps mort de l'instrument, qui correspond à un espace sans coïncidences, et le petit pic qui correspond au délai nul, $\tau = 0$, translaté sur la droite grâce à la ligne à retard. Sur la figure R.16b on voit la mesure de $g^{(2)}(\tau)$ après la procédure de correction du signal, qui enlève l'effet de la ligne à retard et le problème dû au temps mort de l'instrument.

R.2.6 Stabilité

Un des problèmes bien connus des pérovskites est leur photo-stabilité : en effet leur structure tend à être endommagée par un effet combiné de la lumière et de l'humidité, ce qui comporte une dégradation de leur émission jusqu'à la disparition. Plusieurs approches ont été testées pour résoudre le problème : j'en ai utilisé deux différentes. La première

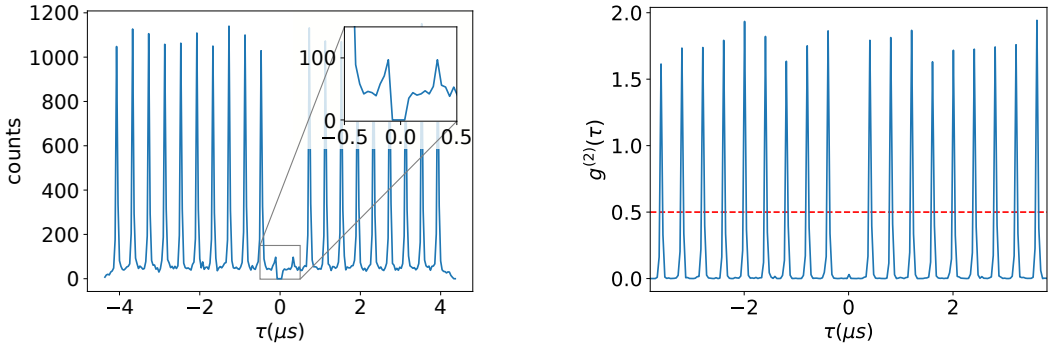

(a) (b)

FIGURE R.16 – Mesures de (a) $g^{(2)}(\tau)$ avant traitement, dans l'encart le temps mort de l'instrument est bien visible. (b) $g^{(2)}(\tau)$ après le traitement. L'émetteur montre un $g^{(2)}(0) \approx 0$, qui signifie une très bonne émission de photons uniques.

consiste à envelopper les pérovskites dans une matrice de polystyrène pour éviter le contact avec l'humidité ambiante, la deuxième à modifier la procédure de fabrication pour obtenir des matériaux plus robustes.

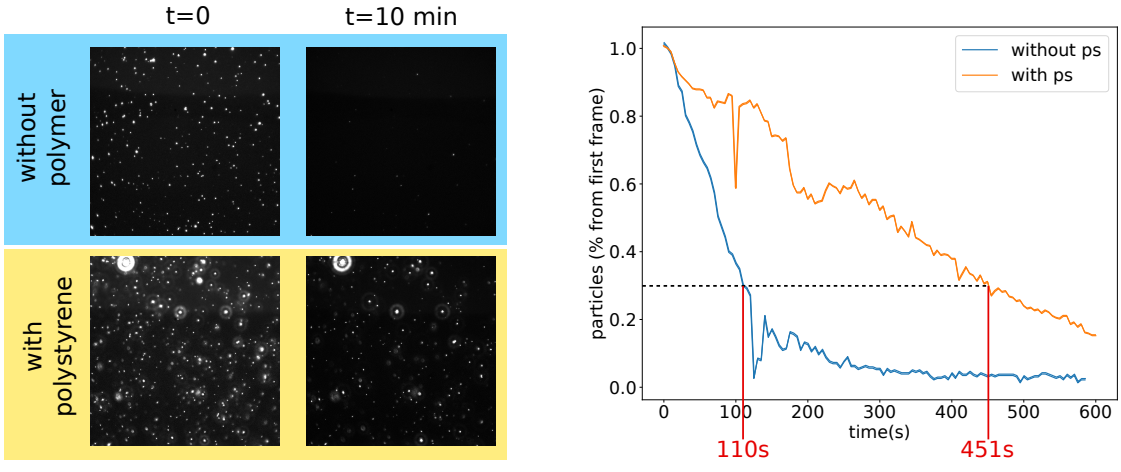

(a) (b)

FIGURE R.17 – (a) Images des échantillons au début de la mesure ($t = 0$) et après dix minutes ($t = 10$ min) sous un fort éclairage LED, sans et avec le polystyrène. (b) Analyse quantitative de la mesure : la stabilité est augmentée d'un facteur quatre.

Les résultats de la première approche sont montrés dans la figure R.17. On peut voir que les nanocristaux enveloppés dans le polystyrène sont capables d'émettre de la lumière pendant un temps quatre fois plus long que les émetteurs nus. On voit donc qu'envelopper les nanocristaux dans un polymère, et en particulier dans le polystyrène,

peut être une méthode efficace pour en améliorer la stabilité. Le test a été effectué avec l'échantillon A. Cette approche a l'inconvénient de nécessiter la présence d'un polymère dans la solution, ce qui pourrait perturber le couplage avec le champ proche et rendre difficile la déposition sur la nanofibre.

On a donc étudié l'effet des ligands présents dans la solution et le rôle de la préparation de l'échantillon. En figure R.18 est montrée la dégradation du spectre d'émission après deux heures de mesure avec l'échantillon B. La dégradation est d'une dizaine de nanomètres, très inférieure aux observations précédentes en littérature Rainò *et al.* [6]. Dans ce travail une dérive équivalente avait été observée en seulement quelques dizaines de secondes. Ce qui est intéressant est aussi l'effet de la dilution, la figure R.19 montre qu'en diluant l'échantillon, on en dégrade rapidement les propriétés de stabilité. La concentration joue donc un rôle crucial dans la stabilité.

R.2.7 Distribution du $g^{(2)}(0)$ en fonction de la longueur d'onde

Avec plusieurs mesures de $g^{(2)}(0)$ on peut vérifier s'il y a un effet de la longueur d'onde sur l'émission. En particulier on peut voir dans la figure R.20 où le $g^{(2)}(0)$ pour trente-trois émetteurs différents est reporté, qu'en général on a une détérioration du $g^{(2)}(0)$ quand la longueur d'onde d'émission augmente. Cela est dû au fait que les grandes longueurs d'onde d'émission correspondent aux émetteurs plus grands, pour lesquels l'effet du confinement quantique est inférieur, d'où la détérioration de l'émission de photons uniques.

R.3 Nanofibres

Les fibres optiques sont un moyen privilégié pour guider la lumière. Depuis leur découverte, elles ont été améliorées et utilisées dans une grande quantité d'applications différentes. Le guidage dans une fibre optique est dû principalement au phénomène de la réflexion totale, ce qui comporte que, si la surface est de bonne qualité (et on peut donc négliger la diffusion), les pertes dans la fibre sont minimales.

Les nanofibres optiques ont un diamètre inférieur à la longueur d'onde de la lumière guidée, ce qui facilite le couplage de la lumière émise par un émetteur directement dans la nanofibre. Généralement elles sont obtenues en étirant une fibre optique standard de façon contrôlée : en particulier dans notre expérience on utilise une flamme pure d'oxygène et hydrogène pour réchauffer la fibre avant de l'étirer, mais l'utilisation d'un laser est aussi possible. Le profil de zone de transition entre la fibre et la nanofibre est

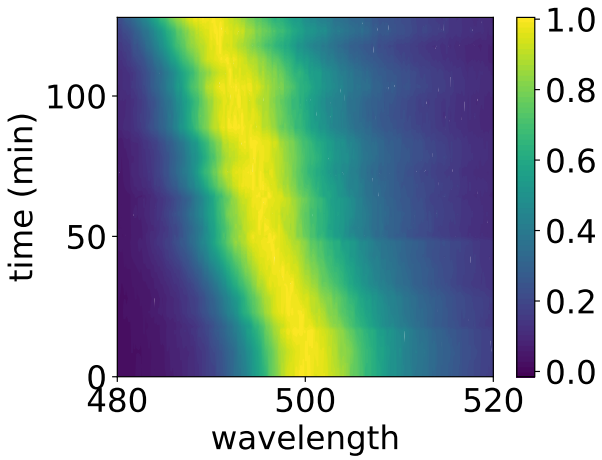

FIGURE R.18 – Évolution du spectre d'émission d'un émetteur de photons uniques de l'échantillon B sur le temps d'illumination. L'émetteur était excité à l'intensité de saturation. Chaque spectre est normalisé. Une dérive d'approximativement 10 nm est visible après deux heures de mesure.

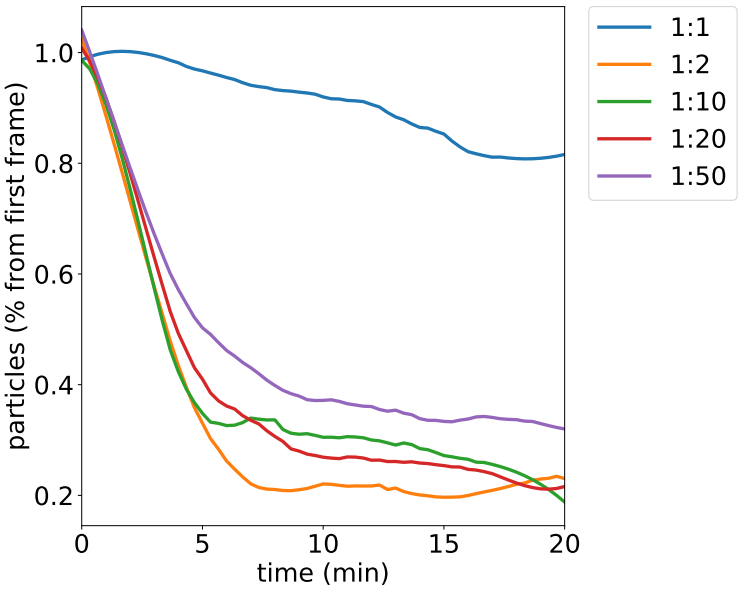

FIGURE R.19 – Mesure de la robustesse de l'échantillon de pérovskites avec des concentrations différentes. Les échantillons ont été obtenus en diluant la solution originale avec du toluène.

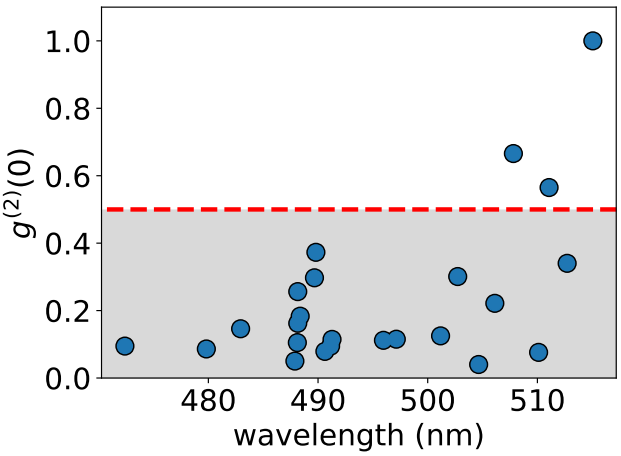

FIGURE R.20 – Distribution de $g^{(2)}(0)$ en fonction de la longueur d'onde d'émission centrale pour 33 émetteurs différents excités à l'intensité de saturation

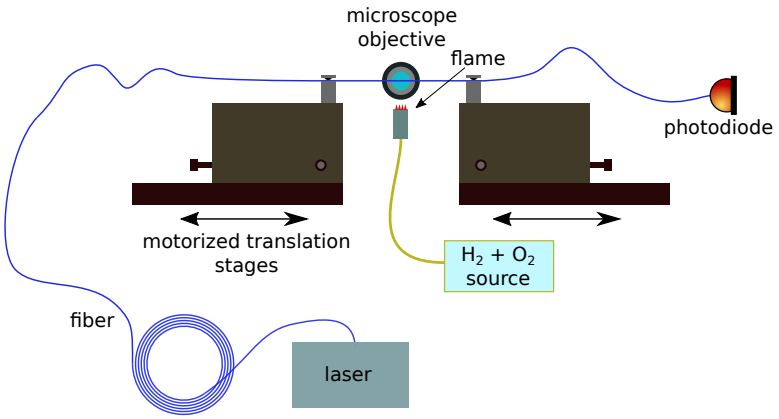

FIGURE R.21 – Montage expérimental pour étirer les nanofibres. Le laser est utilisé pour un surveillance constant de la transmission.

important, pour réduire au minimum les pertes de lumière dans la propagation.

Le montage utilisé pour étirer les nanofibres est montré en figure R.21. Une flamme d'oxygène et hydrogène est utilisé pour réchauffer la nanofibre. Les étages de translation, contrôlés par ordinateur, étirent et déplacent la nanofibre pour obtenir le profil désiré. Les mouvements nécessaires pour obtenir ce profil sont calculés par ordinateur en utilisant la technique développé par BIRKS et LI [86]. Dans ce calcul on tient compte de la transmission souhaitée ainsi que des contraintes expérimentales dont la plus importante est la longueur maximale de la région de transition, limitée à quelques centimètres.

Une fois la fibre étirée, on la déplace sur le montage de l'expérience, pour la coupler avec les émetteurs. Le montage expérimental utilisé est montré en figure R.22. Ce type de

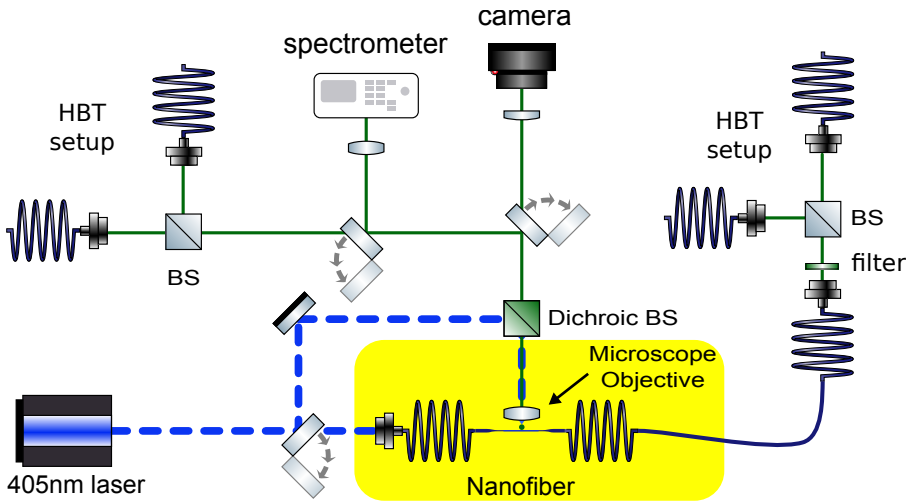

FIGURE R.22 – Montage pour l'étude d'un émetteur sur une nanofibre : le laser pulsé bleu peut exciter le nanoémetteur par la nanofibre ou par l'espace libre. L'image peut être prise par la caméra, le spectre et le $g^{(2)}$ peuvent entre mesurés soit en espace libre soit en utilisant la lumière émise directement dans la fibre. BS : diviseur de faisceaux non polariseur, HBT : Hanbury Brown and Twiss.

montage permet, entre autre, de mesurer le $g^{(2)}$ en utilisant des photons émis directement dans la fibre via le couplage de champ proche.

La déposition d'un émetteur sur la nanofibre s'effectue en la touchant délicatement avec une goutte de solution contenant les émetteurs. Un émetteur peut alors rester collé à la fibre. On peut alors exciter directement le nanoémetteur via la nanofibre pour mesurer le $g^{(2)}$ et vérifier si l'on a effectivement un émetteur unique couplé avec la nanofibre. Un exemple de $g^{(2)}$ obtenu sur des photons émis par un nanocristal de pérovskite directement couplé à la nanofibre est montré dans la figure R.23.

R.4 Perspectives

Dans ma thèse je me suis concentré sur l'étude des nanocristaux de pérovskites couplés à des nanofibres optiques. Ce système présente cependant des limites, surtout dus, d'une part, à l'instabilité des pérovskites et, d'autre part, à la fragilité des fibres optiques.

Concernant ce dernier aspect, j'ai eu l'occasion d'étudier des systèmes différents basés sur de guides d'onde à échange ionique qui pourraient résoudre le problème.

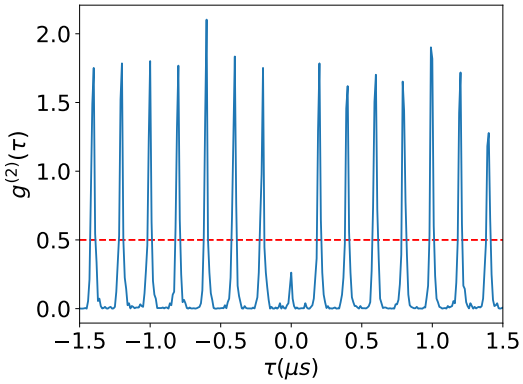

FIGURE R.23 – Fonction d'autocorrélation $g^{(2)}$ d'un nanocristal unique de pérovskite déposé sur une nanofibre : les photons sont émis directement dans la nanofibre et mesurés à sa sortie. On obtient $g^{(2)}(0) = 0.24$.

R.4.1 Emetteurs

Pour ce qui concerne les émetteurs, les défauts réticulaires dans les nanodiamants sont une option qui pourrait résoudre le problème de stabilité des pérovskites. La présence d'un défaut va créer dans le diamant un système de bandes similaire à celui des semiconducteurs, et il a été montré que ces défauts peuvent émettre des photons uniques. En particulier, les centres SiV ont un spectre d'émission fin et la plupart de leur émission (70 %) est dans la *zero phonon line*, même à température ambiante. S'ils présentent l'avantage d'être robustes, leur fabrication est beaucoup plus complexe de celle des nanocristaux de pérovskites. Dans l'échantillon que j'ai pu analyser, je n'ai pas trouvé d'émetteurs uniques.

R.4.2 Guides d'onde à échange ionique

Une solution pour résoudre le problème de la fragilité des nanofibres peut être d'utiliser des structures de guidage de la lumière inscrites dans le verre. J'ai eu l'occasion d'étudier les guides d'onde à échange ionique. En particulier, en travaillant avec Giuseppe Lio, nous avons étudié un système pour déposer des émetteurs sur le guide [115].

En ajoutant une photorésine à la solution qui contient les émetteurs et en déposant une couche de cette solution sur le verre qui contient les guides, il est possible d'utiliser la polymérisation induite par le champ proche et il est ainsi possible de durcir la couche proche du guide. En lavant ensuite l'échantillon avec un solvant adapté, seuls les émetteurs présents sur le guide d'onde vont rester. En effet, on a vérifié que l'émission

des émetteurs était présente à la fin du processus et nous avons caractérisé l'intensité de lumière et le temps nécessaire pour faire la couche la plus fine possible.

Bibliography

[1] Nam-Gyu Park. "Perovskite solar cells: an emerging photovoltaic technology". In: *Materials today* 18.2 (2015), pp. 65–72.

[2] Gabriele Rainò *et al.* "Single Cesium Lead Halide Perovskite Nanocrystals at Low Temperature: Fast Single-Photon Emission, Reduced Blinking, and Exciton Fine Structure". en. In: *ACS Nano* 10.2 (Feb. 2016), pp. 2485–2490. ISSN: 1936-0851, 1936-086X. DOI: 10.1021/acsnano.5b07328.

[3] Caixia Huo *et al.* "Optical Spectroscopy of Single Colloidal $CsPbBr_3$ Perovskite Nanoplatelets". In: *Nano Letters* (Mar. 2020). ISSN: 1530-6984. DOI: 10.1021/acs.nanolett.0c00611.

[4] Young-Shin Park *et al.* "Room Temperature Single-Photon Emission from Individual Perovskite Quantum Dots". en. In: *ACS Nano* 9.10 (Oct. 2015), pp. 10386–10393. ISSN: 1936-0851, 1936-086X. DOI: 10.1021/acsnano.5b04584.

[5] Lung-Chien Chen *et al.* "Influence of PMMA on All-Inorganic Halide Perovskite $CsPbBr_3$ Quantum Dots Combined with Polymer Matrix". en. In: *Materials* 12.6 (Jan. 2019), p. 985. DOI: 10.3390/ma12060985.

[6] Gabriele Rainò *et al.* "Underestimated Effect of a Polymer Matrix on the Light Emission of Single $CsPbBr_3$ Nanocrystals". en. In: *Nano Letters* 19.6 (June 2019), pp. 3648–3653. ISSN: 1530-6984, 1530-6992. DOI: 10.1021/acs.nanolett.9b00689.

[7] Jun Pan *et al.* "Air-Stable Surface-Passivated Perovskite Quantum Dots for Ultra-Robust, Single- and Two-Photon-Induced Amplified Spontaneous Emission". en. In: *The Journal of Physical Chemistry Letters* 6.24 (Dec. 2015), pp. 5027–5033. ISSN: 1948-7185. DOI: 10.1021/acs.jpclett.5b02460.

[8] Fam Le Kien *et al.* "Spontaneous emission of a cesium atom near a nanofiber: Efficient coupling of light to guided modes". In: *Physical Review A* 72.3 (2005), p. 032509.

[9] VV Klimov and Martial Ducloy. "Spontaneous emission rate of an excited atom placed near a nanofiber". In: *Physical Review A* 69.1 (2004), p. 013812.

[10] Masazumi Fujiwara *et al.* "Highly efficient coupling of photons from nanoemitters into single-mode optical fibers". In: *Nano letters* 11.10 (2011), pp. 4362–4365.

[11] Ramachandrarao Yalla, K. P. Nayak, and K. Hakuta. "Fluorescence Photon Measurements from Single Quantum Dots on an Optical Nanofiber". EN. In: *Optics Express* 20.3 (Jan. 2012), pp. 2932–2941. ISSN: 1094-4087. DOI: 10.1364/OE.20.002932.

[12] Maxime Joos *et al.* "Polarization control of linear dipole radiation using an optical nanofiber". In: *Physical Review Applied* 9.6 (2018), p. 064035.

[13] Vadim V. Vorobyov *et al.* "Coupling of Single NV Center to Adiabatically Tapered Opticalsingle Mode Fiber". en. In: *The European Physical Journal D* 70.12 (Dec. 2016), p. 269. ISSN: 1434-6079. DOI: 10.1140/epjd/e2016-70099-3.

[14] David J Griffiths and Darrell F Schroeter. *Introduction to quantum mechanics*. Cambridge University Press, 2018.

[15] J. J. Sakurai and Jim Napolitano. *Modern Quantum Mechanics*. 2nd ed. Boston: Addison-Wesley, 2011. ISBN: 978-0-8053-8291-4.

[16] W. K. Wootters and W. H. Zurek. "A Single Quantum Cannot Be Cloned". en. In: *Nature* 299.5886 (Oct. 1982), pp. 802–803. ISSN: 1476-4687. DOI: 10.1038/299802a0.

[17] Frank Arute *et al.* "Quantum Supremacy Using a Programmable Superconducting Processor". en. In: *Nature* 574.7779 (Oct. 2019), pp. 505–510. ISSN: 1476-4687. DOI: 10.1038/s41586-019-1666-5.

[18] Malvin C. Teich and Bahaa E.A. Saleh. "I Photon Bunching and Antibunching". en. In: *Progress in Optics*. Vol. 26. Elsevier, 1988, pp. 1–104. ISBN: 978-0-444-87096-4. DOI: 10.1016/S0079-6638(08)70174-4.

[19] Roy J. Glauber. "The Quantum Theory of Optical Coherence". en. In: *Physical Review* 130.6 (June 1963), pp. 2529–2539. ISSN: 0031-899X. DOI: 10.1103/PhysRev.130.2529.

[20] Rodney Loudon. *The quantum theory of light*. OUP Oxford, 2000.

[21] M. D. Eisaman *et al.* "Invited Review Article: Single-Photon Sources and Detectors". en. In: *Review of Scientific Instruments* 82.7 (July 2011), p. 071101. ISSN: 0034-6748, 1089-7623. DOI: 10.1063/1.3610677.

[22] A. L. Migdall, D. Branning, and S. Castelletto. "Tailoring Single-Photon and Multiphoton Probabilities of a Single-Photon on-Demand Source". In: *Physical Review A* 66.5 (Nov. 2002), p. 053805. DOI: 10.1103/PhysRevA.66.053805.

[23] M. J. Fitch *et al.* "Photon-Number Resolution Using Time-Multiplexed Single-Photon Detectors". In: *Physical Review A* 68.4 (Oct. 2003), p. 043814. DOI: 10.1103/PhysRevA.68.043814.

[24] Evan Jeffrey, Nicholas A. Peters, and Paul G. Kwiat. "Towards a Periodic Deterministic Source of Arbitrary Single-Photon States". en. In: *New Journal of Physics* 6 (July 2004), pp. 100–100. ISSN: 1367-2630. DOI: 10.1088/1367-2630/6/1/100.

[25] Jeffrey H. Shapiro and Franco N. Wong. "On-Demand Single-Photon Generation Using a Modular Array of Parametric Downconverters with Electro-Optic Polarization Controls". EN. In: *Optics Letters* 32.18 (Sept. 2007), pp. 2698–2700. ISSN: 1539-4794. DOI: 10.1364/OL.32.002698.

[26] Axel Kuhn, Markus Hennrich, and Gerhard Rempe. "Deterministic Single-Photon Source for Distributed Quantum Networking". In: *Physical Review Letters* 89.6 (July 2002), p. 067901. DOI: 10.1103/PhysRevLett.89.067901.

[27] J. McKeever *et al.* "Deterministic Generation of Single Photons from One Atom Trapped in a Cavity". en. In: *Science* 303.5666 (Mar. 2004), pp. 1992–1994. ISSN: 0036-8075, 1095-9203. DOI: 10.1126/science.1095232.

[28] M. Hennrich *et al.* "Photon Statistics of a Non-Stationary Periodically Driven Single-Photon Source". en. In: *New Journal of Physics* 6 (July 2004), pp. 86–86. ISSN: 1367-2630. DOI: 10.1088/1367-2630/6/1/086.

[29] T. Wilk *et al.* "Polarization-Controlled Single Photons". In: *Physical Review Letters* 98.6 (Feb. 2007), p. 063601. DOI: 10.1103/PhysRevLett.98.063601.

[30] Markus Hijlkema *et al.* "A Single-Photon Server with Just One Atom". en. In: *Nature Physics* 3.4 (Apr. 2007), pp. 253–255. ISSN: 1745-2481. DOI: 10.1038/nphys569.

[31] Barak Dayan *et al.* "A Photon Turnstile Dynamically Regulated by One Atom". en. In: *Science* 319.5866 (Feb. 2008), pp. 1062–1065. ISSN: 0036-8075, 1095-9203. DOI: 10.1126/science.1152261.

[32] Takao Aoki *et al.* "Efficient Routing of Single Photons by One Atom and a Microtoroidal Cavity". In: *Physical Review Letters* 102.8 (Feb. 2009), p. 083601. DOI: 10.1103/PhysRevLett.102.083601.

[33] Edward Mills Purcell. "Spontaneous emission probabilities at radio frequencies". In: *Confined Electrons and Photons*. Springer, 1995, pp. 839–839.

[34] Nikolay V. Vitanov *et al.* "Stimulated Raman Adiabatic Passage in Physics, Chemistry, and Beyond". In: *Reviews of Modern Physics* 89.1 (Mar. 2017), p. 015006. DOI: 10.1103/RevModPhys.89.015006.

[35] D. Kielpinski, C. Monroe, and D. J. Wineland. "Architecture for a Large-Scale Ion-Trap Quantum Computer". en. In: *Nature* 417.6890 (June 2002), pp. 709–711. ISSN: 1476-4687. DOI: 10.1038/nature00784.

[36] M. Riebe *et al.* "Deterministic Entanglement Swapping with an Ion-Trap Quantum Computer". en. In: *Nature Physics* 4.11 (Nov. 2008), pp. 839–842. ISSN: 1745-2481. DOI: 10.1038/nphys1107.

[37] Jonathan P. Home *et al.* "Complete Methods Set for Scalable Ion Trap Quantum Information Processing". en. In: *Science* 325.5945 (Sept. 2009), pp. 1227–1230. ISSN: 0036-8075, 1095-9203. DOI: 10.1126/science.1177077.

[38] F. Jelezko and J. Wrachtrup. "Single Defect Centres in Diamond: A Review". en. In: *physica status solidi (a)* 203.13 (Oct. 2006), pp. 3207–3225. ISSN: 1862-6319. DOI: 10.1002/pssa.200671403.

[39] J. P. Hadden *et al.* "Integrated Waveguides and Deterministically Positioned Nitrogen Vacancy Centers in Diamond Created by Femtosecond Laser Writing". EN. In: *Optics Letters* 43.15 (Aug. 2018), pp. 3586–3589. ISSN: 1539-4794. DOI: 10.1364/OL.43.003586.

[40] Chunlang Wang *et al.* "Single Photon Emission from SiV Centres in Diamond Produced by Ion Implantation". en. In: *Journal of Physics B: Atomic, Molecular and Optical Physics* 39.1 (2006), p. 37. ISSN: 0953-4075. DOI: 10.1088/0953-4075/39/1/005.

[41] Elke Neu *et al.* "Single Photon Emission from Silicon-Vacancy Colour Centres in Chemical Vapour Deposition Nano-Diamonds on Iridium". en. In: *New Journal of Physics* 13.2 (2011), p. 025012. ISSN: 1367-2630. DOI: 10.1088/1367-2630/13/2/025012.

[42] Sarah Lindner *et al.* "Strongly Inhomogeneous Distribution of Spectral Properties of Silicon-Vacancy Color Centers in Nanodiamonds". en. In: (), p. 24.

[43] Lise Meitner. "Über die Entstehung der β-Strahl-Spektren radioaktiver Substanzen". de. In: *Zeitschrift für Physik* 9.1 (Dec. 1922), pp. 131–144. ISSN: 0044-3328. DOI: 10.1007/BF01326962.

[44] V. I. Klimov *et al.* "Quantization of Multiparticle Auger Rates in Semiconductor Quantum Dots". en. In: *Science* 287.5455 (Feb. 2000), pp. 1011–1013. ISSN: 0036-8075, 1095-9203. DOI: 10.1126/science.287.5455.1011.

[45] István Robel *et al.* "Universal Size-Dependent Trend in Auger Recombination in Direct-Gap and Indirect-Gap Semiconductor Nanocrystals". In: *Physical Review Letters* 102.17 (May 2009), p. 177404. DOI: 10.1103/PhysRevLett.102.177404.

[46] Stefano Vezzoli. "Experimental Study of Nanocrystals as Single Photon Sources". These de Doctorat. Paris 6, Jan. 2013.

[47] M. Manceau *et al.* "CdSe/CdS Dot-in-Rods Nanocrystals Fast Blinking Dynamics." en. In: *ChemPhysChem* 19.23 (2018), pp. 3288–3295. ISSN: 1439-7641. DOI: 10.1002/cphc.201800694.

[48] Rogier Verberk, Antoine M. van Oijen, and Michel Orrit. "Simple Model for the Power-Law Blinking of Single Semiconductor Nanocrystals". In: *Physical Review B* 66.23 (Dec. 2002), p. 233202. DOI: 10.1103/PhysRevB.66.233202.

[49] Rogier Verberk and Michel Orrit. "Photon Statistics in the Fluorescence of Single Molecules and Nanocrystals: Correlation Functions versus Distributions of on- and off-Times". In: *The Journal of Chemical Physics* 119.4 (July 2003), pp. 2214–2222. ISSN: 0021-9606. DOI: 10.1063/1.1582848.

[50] Leonhard Euler. "De progressionibus transcendentibus seu quarum termini generales algebraice dari nequeunt". In: *Commentarii academiae scientiarum Petropolitanae* (1738), pp. 36–57.

[51] Christophe Galland *et al.* "Two Types of Luminescence Blinking Revealed by Spectroelectrochemistry of Single Quantum Dots". en. In: *Nature* 479.7372 (Nov. 2011), pp. 203–207. ISSN: 1476-4687. DOI: 10.1038/nature10569.

[52] F. Pisanello *et al.* "Dots in Rods as Polarized Single Photon Sources". en. In: *Superlattices and Microstructures*. Proceedings of the 9th International Conference on Physics of Light-Matter Coupling in Nanostructures, PLMCN 2009 (Lecce - Italy) 47.1 (Jan. 2010), pp. 165–169. ISSN: 0749-6036. DOI: 10.1016/j.spmi.2009.06.009.

[53] Ferruccio Pisanello *et al.* "Room Temperature-Dipolelike Single Photon Source with a Colloidal Dot-in-Rod". In: *Applied Physics Letters* 96.3 (Jan. 2010), p. 033101. ISSN: 0003-6951. DOI: 10.1063/1.3291849.

[54] F. Kaiser *et al.* "Polarization Properties of Single Photons Emitted by Nitrogen-Vacancy Defect in Diamond at Low Temperature". In: *arXiv:0906.3426 [quant-ph]* (June 2009). arXiv: 0906.3426 [quant-ph].

[55] Lars Thylén and Lech Wosinski. "Integrated Photonics in the 21st Century". EN. In: *Photonics Research* 2.2 (Apr. 2014), pp. 75–81. ISSN: 2327-9125. DOI: 10.1364/PRJ.2.000075.

[56] R. J. P. Engelen *et al.* "The Effect of Higher-Order Dispersion on Slow Light Propagation in Photonic Crystal Waveguides". EN. In: *Optics Express* 14.4 (Feb. 2006), pp. 1658–1672. ISSN: 1094-4087. DOI: 10.1364/OE.14.001658.

[57] Hemant Sankar Dutta *et al.* "Coupling Light in Photonic Crystal Waveguides: A Review". en. In: *Photonics and Nanostructures - Fundamentals and Applications* 20 (July 2016), pp. 41–58. ISSN: 1569-4410. DOI: 10.1016/j.photonics.2016.04.001.

[58] Yurui Fang and Mengtao Sun. "Nanoplasmonic Waveguides: Towards Applications in Integrated Nanophotonic Circuits". en. In: *Light: Science & Applications* 4.6 (June 2015), e294–e294. ISSN: 2047-7538. DOI: 10.1038/lsa.2015.67.

[59] Jaime García-Rupérez *et al.* "Label-Free Antibody Detection Using Band Edge Fringes in SOI Planar Photonic Crystal Waveguides in the Slow-Light Regime". EN. In: *Optics Express* 18.23 (Nov. 2010), pp. 24276–24286. ISSN: 1094-4087. DOI: 10.1364/OE.18.024276.

[60] A. Block *et al.* "Bloch Oscillations in Plasmonic Waveguide Arrays". en. In: *Nature Communications* 5.1 (May 2014), p. 3843. ISSN: 2041-1723. DOI: 10.1038/ncomms4843.

[61] Eugene A. Katz. "Perovskite: Name Puzzle and German-Russian Odyssey of Discovery". In: *Helvetica Chimica Acta* (). DOI: 10.1002/hlca.202000061.

[62] G. H. Jonker and J. H. Van Santen. "Ferromagnetic Compounds of Manganese with Perovskite Structure". en. In: *Physica* 16.3 (Mar. 1950), pp. 337–349. ISSN: 0031-8914. DOI: 10.1016/0031-8914(50)90033-4.

[63] In Chung *et al.* "All-Solid-State Dye-Sensitized Solar Cells with High Efficiency". en. In: *Nature* 485.7399 (May 2012), pp. 486–489. ISSN: 1476-4687. DOI: 10.1038/nature11067.

[64] Felix Deschler, Dieter Neher, and Lukas Schmidt-Mende. "Perovskite Semiconductors for next Generation Optoelectronic Applications". In: *APL Materials* 7.8 (Aug. 2019), p. 080401. DOI: 10.1063/1.5119744.

[65] Wei Geng *et al.* "Localised Excitation of a Single Photon Source by a Nanowaveguide". en. In: *Scientific Reports* 6.1 (Jan. 2016), pp. 1–9. ISSN: 2045-2322. DOI: 10.1038/srep19721.

[66] K. Muhammed Shafi *et al.* "Occurrence Control of Charged Exciton for a Single CdSe Quantum Dot at Cryogenic Temperatures on an Optical Nanofiber". en. In: *arXiv:2003.10619 [cond-mat, physics:quant-ph]* (Mar. 2020). arXiv: 2003.10619 [cond-mat, physics:quant-ph].

[67] Michael A. Becker *et al.* "Bright Triplet Excitons in Caesium Lead Halide Perovskites". en. In: *Nature* 553.7687 (Jan. 2018), pp. 189–193. ISSN: 1476-4687. DOI: 10.1038/nature25147.

[68] Peter C. Sercel *et al.* "Exciton Fine Structure in Perovskite Nanocrystals". In: *Nano Letters* 19.6 (June 2019), pp. 4068–4077. ISSN: 1530-6984. DOI: 10.1021/acs.nanolett.9b01467.

[69] Loredana Protesescu *et al.* "Nanocrystals of cesium lead halide perovskites ($CsPbX_3$, X= Cl, Br, and I): novel optoelectronic materials showing bright emission with wide color gamut". In: *Nano letters* 15.6 (2015), pp. 3692–3696.

[70] Mark C. Weidman *et al.* "Highly Tunable Colloidal Perovskite Nanoplatelets through Variable Cation, Metal, and Halide Composition". In: *ACS Nano* 10.8 (Aug. 2016), pp. 7830–7839. ISSN: 1936-0851. DOI: 10.1021/acsnano.6b03496.

[71] Sujata Tarafdar *et al. Droplet Drying Patterns on Solid Substrates: From Hydrophilic to Superhydrophobic Contact to Levitating Drops.* en. Review Article. 2018. DOI: 10.1155/2018/5214924.

[72] Clotilde Lethiec *et al.* "Measurement of Three-Dimensional Dipole Orientation of a Single Fluorescent Nanoemitter by Emission Polarization Analysis". In: *Physical Review X* 4.2 (May 2014), p. 021037. DOI: 10.1103/PhysRevX.4.021037.

[73] H. G. Berry, G. Gabrielse, and A. E. Livingston. "Measurement of the Stokes Parameters of Light". EN. In: *Applied Optics* 16.12 (Dec. 1977), pp. 3200–3205. ISSN: 2155-3165. DOI: 10.1364/AO.16.003200.

[74] C.E. Shannon. "Communication in the Presence of Noise". In: *Proceedings of the IRE* 37.1 (Jan. 1949), pp. 10–21. ISSN: 2162-6634. DOI: 10.1109/JRPROC.1949.232969.

[75] V. Andreev *et al.* "A Self-Calibrating Polarimeter to Measure Stokes Parameters". In: *arXiv:1703.00963 [physics]* (Feb. 2017). arXiv: 1703.00963 [physics].

[76] Ernst Mach. *The principles of physical optics: an historical and philosophical treatment*. Courier Corporation, 2013.

[77] Daniel Colladon. "On the reflections of a ray of light inside a parabolic liquid stream". In: *Comptes Rendus* 15 (1842), pp. 800–802.

[78] Bahaa E. A. Saleh and Malvin Carl Teich. *Fundamentals of Photonics*. 2nd ed. Wiley Series in Pure and Applied Optics. Hoboken, N.J: Wiley Interscience, 2007. ISBN: 978-0-471-35832-9.

[79] Limin Tong, Jingyi Lou, and Eric Mazur. "Single-Mode Guiding Properties of Subwavelength-Diameter Silica and Silicon Wire Waveguides". EN. In: *Optics Express* 12.6 (Mar. 2004), pp. 1025–1035. ISSN: 1094-4087. DOI: 10.1364/OPEX.12.001025.

[80] Katsunari Okamoto. *Fundamentals of Optical Waveguides*. en. 2nd ed. Amsterdam ; Boston: Elsevier, 2006. ISBN: 978-0-12-525096-2.

[81] D. Gloge. "Weakly Guiding Fibers". EN. In: *Applied Optics* 10.10 (Oct. 1971), pp. 2252–2258. ISSN: 2155-3165. DOI: 10.1364/AO.10.002252.

[82] Jan Petersen, Jürgen Volz, and Arno Rauschenbeutel. "Chiral Nanophotonic Waveguide Interface Based on Spin-Orbit Interaction of Light". en. In: *Science* 346.6205 (Oct. 2014), pp. 67–71. ISSN: 0036-8075, 1095-9203. DOI: 10.1126/science.1257671.

[83] R. Mitsch *et al.* "Quantum State-Controlled Directional Spontaneous Emission of Photons into a Nanophotonic Waveguide". en. In: *Nature Communications* 5.1 (Dec. 2014), p. 5713. ISSN: 2041-1723. DOI: 10.1038/ncomms6713.

[84] Ryutaro Nagai and Takao Aoki. "Ultra-Low-Loss Tapered Optical Fibers with Minimal Lengths". en. In: *Optics Express* 22.23 (Nov. 2014), p. 28427. ISSN: 1094-4087. DOI: 10.1364/OE.22.028427.

[85] J.D. Love *et al.* "Tapered Single-Mode Fibres and Devices. Part 1: Adiabaticity Criteria". en. In: *IEE Proceedings J Optoelectronics* 138.5 (1991), p. 343. ISSN: 02673932. DOI: 10.1049/ip-j.1991.0060.

[86] T.A. Birks and Y.W. Li. "The Shape of Fiber Tapers". In: *Journal of Lightwave Technology* 10.4 (Apr. 1992), pp. 432–438. ISSN: 07338724. DOI: 10.1109/50.134196.

[87] J Dewynne, JR Ockendon, and P Wilmott. "On a mathematical model for fiber tapering". In: *SIAM Journal on Applied Mathematics* 49.4 (1989), pp. 983–990.

[88] K. P. Nayak and K. Hakuta. "Single Atoms on an Optical Nanofibre". en. In: *New Journal of Physics* 10.5 (May 2008), p. 053003. ISSN: 1367-2630. DOI: 10.1088/1367-2630/10/5/053003.

[89] K. P. Nayak *et al.* "Antibunching and Bunching of Photons in Resonance Fluorescence from a Few Atoms into Guided Modes of an Optical Nanofiber". en. In: *Physical Review A* 79.2 (Feb. 2009), p. 021801. ISSN: 1050-2947, 1094-1622. DOI: 10.1103/PhysRevA.79.021801.

[90] Tim Schröder *et al.* "A Nanodiamond-Tapered Fiber System with High Single-Mode Coupling Efficiency". EN. In: *Optics Express* 20.10 (May 2012), pp. 10490–10497. ISSN: 1094-4087. DOI: 10.1364/OE.20.010490.

[91] Lars Liebermeister *et al.* "Tapered Fiber Coupling of Single Photons Emitted by a Deterministically Positioned Single Nitrogen Vacancy Center". en. In: *Applied Physics Letters* 104.3 (Jan. 2014), p. 031101. ISSN: 0003-6951, 1077-3118. DOI: 10.1063/1.4862207.

[92] Masazumi Fujiwara *et al.* "Ultrathin Fiber-Taper Coupling with Nitrogen Vacancy Centers in Nanodiamonds at Cryogenic Temperatures". EN. In: *Optics Letters* 40.24 (Dec. 2015), pp. 5702–5705. ISSN: 1539-4794. DOI: 10.1364/OL.40.005702.

[93] Yehonadav Bekenstein *et al.* "Highly Luminescent Colloidal Nanoplates of Perovskite Cesium Lead Halide and Their Oriented Assemblies". In: *Journal of the American Chemical Society* 137.51 (Dec. 2015), pp. 16008–16011. ISSN: 0002-7863. DOI: 10.1021/jacs.5b11199.

[94] Quinten A. Akkerman *et al.* "Solution Synthesis Approach to Colloidal Cesium Lead Halide Perovskite Nanoplatelets with Monolayer-Level Thickness Control". In: *Journal of the American Chemical Society* 138.3 (Jan. 2016), pp. 1010–1016. ISSN: 0002-7863. DOI: 10.1021/jacs.5b12124.

[95] S. Pierini *et al.* "Hybrid Devices for Quantum Nanophotonics". en. In: *Journal of Physics: Conference Series* 1537 (May 2020), p. 012005. ISSN: 1742-6596. DOI: 10.1088/1742-6596/1537/1/012005.

[96] Dongdong Yan *et al.* "Ultrastable $CsPbBr_3$ Perovskite Quantum Dot and Their Enhanced Amplified Spontaneous Emission by Surface Ligand Modification". en. In: *Small* (Apr. 2019), p. 1901173. ISSN: 1613-6810, 1613-6829. DOI: 10.1002/smll.201901173.

[97] Gordon Davies and Institution of Electrical Engineers, eds. *Properties and Growth of Diamond*. eng. EMIS Datareviews Series 9. London: INSPEC, the Institution of Electrical Engineers, 1994. ISBN: 978-0-85296-875-8.

[98] Mackrine Nahra *et al.* "Single Germanium Vacancy Centres in Nanodiamonds with Bulk-like Spectral Stability". en. In: *arXiv:2010.15475 [quant-ph]* (Oct. 2020). arXiv: 2010.15475 [quant-ph].

[99] Michael Trupke *et al.* "Enhancing Photon Collection from Quantum Emitters in Diamond". en. In: *Progress in Informatics* 8 (Mar. 2011), p. 33. ISSN: 1349-8614, 1349-8606. DOI: 10.2201/NiiPi.2011.8.4.

[100] Lucio Robledo *et al.* "Spin dynamics in the optical cycle of single nitrogen-vacancy centres in diamond". In: *New Journal of Physics* 13.2 (2011), p. 025013.

[101] Jeffrey Holzgrafe *et al.* "Error Corrected Spin-State Readout in a Nanodiamond". en. In: *npj Quantum Information* 5.1 (Feb. 2019), pp. 1–6. ISSN: 2056-6387. DOI: 10.1038/s41534-019-0126-2.

[102] Helena S. Knowles, Dhiren M. Kara, and Mete Atatüre. "Observing Bulk Diamond Spin Coherence in High-Purity Nanodiamonds". en. In: *Nature Materials* 13.1 (Jan. 2014), pp. 21–25. ISSN: 1476-4660. DOI: 10.1038/nmat3805.

[103] A. I. Zeleneev *et al.* "Nanodiamonds with SiV Colour Centres for Quantum Technologies". en. In: *Quantum Electronics* 50.3 (Mar. 2020), p. 299. ISSN: 1063-7818. DOI: 10.1070/QEL17189.

[104] Jonas Nils Becker *et al.* "Ultrafast All-Optical Coherent Control of Single Silicon Vacancy Colour Centres in Diamond". en. In: *Nature Communications* 7.1 (Dec. 2016), p. 13512. ISSN: 2041-1723. DOI: 10.1038/ncomms13512.

[105] L. Marseglia *et al.* "Bright Nanowire Single Photon Source Based on SiV Centers in Diamond". EN. In: *Optics Express* 26.1 (Jan. 2018), pp. 80–89. ISSN: 1094-4087. DOI: 10.1364/OE.26.000080.

[106] Elke Neu, Mario Agio, and Christoph Becher. "Photophysics of Single Silicon Vacancy Centers in Diamond: Implications for Single Photon Emission". EN. In: *Optics Express* 20.18 (Aug. 2012), pp. 19956–19971. ISSN: 1094-4087. DOI: 10.1364/OE.20.019956.

[107] Stefan Häußler *et al.* "Photoluminescence Excitation Spectroscopy of SiV $^-$ and GeV $^-$ Color Center in Diamond". en. In: *New Journal of Physics* 19.6 (June 2017), p. 063036. ISSN: 1367-2630. DOI: 10.1088/1367-2630/aa73e5.

[108] Jean-Paul Boudou *et al.* "Fluorescent Nanodiamonds Derived from HPHT with a Size of Less than 10nm". en. In: *Diamond and Related Materials* 37 (Aug. 2013), pp. 80–86. ISSN: 0925-9635. DOI: 10.1016/j.diamond.2013.05.006.

[109] Romana Schirhagl *et al.* "Nitrogen-Vacancy Centers in Diamond: Nanoscale Sensors for Physics and Biology". In: *Annual Review of Physical Chemistry* 65.1 (2014), pp. 83–105. DOI: 10.1146/annurev-physchem-040513-103659.

[110] Ari Tervonen, Seppo K. Honkanen, and Brian R. West. "Ion-Exchanged Glass Waveguide Technology: A Review". In: *Optical Engineering* 50.7 (July 2011), p. 071107. ISSN: 0091-3286, 1560-2303. DOI: 10.1117/1.3559213.

[111] R. G. Walker, C. D. W. Wilkinson, and J. a. H. Wilkinson. "Integrated Optical Waveguiding Structures Made by Silver Ion-Exchange in Glass. 1: The Propagation Characteristics of Stripe Ion-Exchanged Waveguides; a Theoretical and Experimental Investigation". EN. In: *Applied Optics* 22.12 (June 1983), pp. 1923–1928. ISSN: 2155-3165. DOI: 10.1364/AO.22.001923.

[112] Martin N. Weiss and Ramakant Srivastava. "Determination of Ion-Exchanged Channel Waveguide Profile Parameters by Mode-Index Measurements". EN. In: *Applied Optics* 34.3 (Jan. 1995), pp. 455–458. ISSN: 2155-3165. DOI: 10.1364/AO.34.000455.

[113] Josslyn Beltran Madrigal *et al.* "Hybrid Integrated Optical Waveguides in Glass for Enhanced Visible Photoluminescence of Nanoemitters". en. In: *Applied Optics* 55.36 (Dec. 2016), p. 10263. ISSN: 0003-6935, 1539-4522. DOI: 10.1364/AO.55.010263.

[114] Andreas W. Schell *et al.* "A Scanning Probe-Based Pick-and-Place Procedure for Assembly of Integrated Quantum Optical Hybrid Devices". In: *Review of Scientific Instruments* 82.7 (July 2011), p. 073709. ISSN: 0034-6748. DOI: 10.1063/1.3615629.

[115] Giuseppe Emanuele Lio *et al.* "Integration of Nanoemitters onto Photonic Structures by Guided Evanescent-Wave Nano-Photopolymerization". In: *The Journal of Physical Chemistry C* 123.23 (June 2019), pp. 14669–14676. ISSN: 1932-7447. DOI: 10.1021/acs.jpcc.9b03716.

[116] Shoji Maruo, Osamu Nakamura, and Satoshi Kawata. "Three-Dimensional Microfabrication with Two-Photon-Absorbed Photopolymerization". EN. In: *Optics Letters* 22.2 (Jan. 1997), pp. 132–134. ISSN: 1539-4794. DOI: 10.1364/OL.22.000132.

[117] Brian H. Cumpston *et al.* "Two-Photon Polymerization Initiators for Three-Dimensional Optical Data Storage and Microfabrication". en. In: *Nature* 398.6722 (Mar. 1999), pp. 51–54. ISSN: 1476-4687. DOI: 10.1038/17989.

[118] Carole Ecoffet, Anne Espanet, and Daniel J. Lougnot. "Photopolymerization by Evanescent Waves: A New Method to Obtain Nanoparts". In: *Advanced Materials* 10.5 (1998), pp. 411–414. ISSN: 1521-4095. DOI: 10.1002/(SICI)1521-4095(199803)10:5<411::AID-ADMA411>3.0.CO;2-P.

[119] Martí Duocastella *et al.* "Improving the Spatial Resolution in Direct Laser Writing Lithography by Using a Reversible Cationic Photoinitiator". In: *The Journal of Physical Chemistry C* 121.31 (Aug. 2017), pp. 16970–16977. ISSN: 1932-7447. DOI: 10.1021/acs.jpcc.7b03591.

[120] Dandan Ge *et al.* "Hybrid Plasmonic Nano-Emitters with Controlled Single Quantum Emitter Positioning on the Local Excitation Field". en. In: *Nature Communications* 11.1 (July 2020), p. 3414. ISSN: 2041-1723. DOI: 10.1038/s41467-020-17248-8.

[121] *About Qt - Qt Wiki*. https://wiki.qt.io/About_Qt#What_is_Qt.3F. [Online; accessed 13-Ott-2020].

[122] *Qwt User's Guide: Qwt - Qt Widgets for Technical Applications*. https://qwt.sourceforge.io/index.html. [Online; accessed 13-Ott-2020].

[123] Stefano Pierini *et al.* "Highly Photostable Perovskite Nanocubes: Toward Integrated Single Photon Sources Based on Tapered Nanofibers". In: *ACS Photonics* 7.8 (Aug. 2020), pp. 2265–2272. DOI: 10.1021/acsphotonics.0c00820.

Stefano PIERINI

Doctorat : Matériaux, Mécanique, Optique, Nanotechnologie

Année 2021

Étude des nanocristaux de pérovskite comme sources de photons uniques pour la photonique quantique intégrée

Cette thèse est consacrée à l'étude du couplage d'émetteurs de photons uniques avec des nanostructures photoniques en utilisant les propriétés du champ proche d'une structure photonique en vue de la réalisation d'une source à photons uniques intégrée et compacte pour des applications quantiques. La première partie de mon travail de thèse a été consacrée à l'optimisation des nanocristaux de pérovskites. Bien que les nanocristaux de pérovskites soient des sources de photons uniques très prometteuses, ils nécessitent encore des améliorations : dans ce travail, je passe en revue les principales propriétés de ces émetteurs et je présente une caractérisation complète des nanocristaux de pérovskites avec une photo-stabilité améliorée, un clignotement réduit et un fort dégroupement de photons. Dans la deuxième partie de la thèse, je me concentre sur le couplage des émetteurs quantiques avec diverses structures photoniques : à savoir les nanofibres optiques effilées et les guides d'ondes à échange d'ions. La méthode de fabrication et les propriétés optiques des nanofibres sont décrites en détail et le couplage d'un nanocristal de pérovskite unique avec une nanofibre est réalisé, ce qui constitue une preuve de principe d'une source hybride et intégrée de photons uniques. Enfin, je montre comment le champ proche autour des guides d'ondes d'échange d'ions peut être utilisé avec la polymérisation en champ proche pour piéger des émetteurs quantiques sur les guides d'ondes.

Mots clés : optique quantique – nanophotonique – pérovskites – nanocristaux – nanofibres.

Experimental Study of Perovskite Nanocrystals as Single Photon Sources for Integrated Quantum Photonics

This thesis is devoted to the study of the coupling of single-photon emitters with photonic nanostructures by using the properties of the near field of a photonic structure in view of the realization of a compact integrated single-photon source for quantum applications. The first part of my thesis work was consecrated to the optimization of perovskites nanocrystals. Although perovskites nanocrystals are very promising single-photon sources, they still need improvements: in this work, I review the main properties of these emitters and present a full characterization of perovskite nanocrystals with improved photo-stability, reduced blinking ad strong antibunching. In the second part of the thesis, I focus on the coupling of quantum emitters with various photonic structures: namely the tapered optical nanofibers and the ion-exchange waveguides. The fabrication method and the optical properties of the nanofibers are described in detail and the coupling of a single perovskite nanocrystal with a nanofiber is achieved, which constitutes a proof of principle of a hybrid integrated single-photon source. Finally, I show how the near field around ion Exchange waveguides can be employed together with near-field polymerizations to trap single-photon emitters onto the waveguides.

Keywords: quantum optics – nanophotonics – perovskite – nanocrystals – nanofibers.